Novel Effects in Optical Coherence: Fundamentals and Applications

by

Omar S. Magaña-Loaiza

Submitted in Partial Fulfillment of
the Requirements for the Degree
Doctor of Philosophy

Supervised by
Professor Robert W. Boyd

Materials Science Program
Arts, Sciences and Engineering
Edmund A. Hajim School of Engineering and Applied Sciences

University of Rochester
Rochester, New York

2016

For my family and friends, with thanks for the great times

Biographical Sketch

Omar S. Magaña-Loaiza was born in Tijuana, México in September of 1986. He joined Centro de Enseñanza Técnica y Superior (CETYS) Universidad in 2004. At CETYS Universidad, he majored in Electrical Engineering. After graduating from CETYS Universidad in 2008, he joined the Instituto Nacional de Astrofísica, Óptica y Electrónica (INAOE) in Puebla and conducted research on quantum photonics under the supervision of Professor Jose J. Sanchez-Mondragon. In 2010, he obtained a Master of Science degree in Optics from INAOE. This same year he began doctoral studies in materials science at the University of Rochester. In 2011, he pursue research in quantum optics under the supervision of Professor Robert W. Boyd. Omar received a Master of Science degree from the University of Rochester in 2012.

The following publications were a result of work conducted during doctoral study

[1] "Exotic Looped Trajectories of Photons in Three-Slit Interference", O. S. Magaña-Loaiza, I De Leon, M. Mirhosseini, R. Fickler, A. Safari, M. Uwe, B. Mcintyre, P. Banzer, B Rodenburg, G. Leuchs and R. W. Boyd, **Under Review**, (2016).

[2] "Hanbury Brown and Twiss Interferometry with Twisted Light", O. S. Magaña-Loaiza, M. Mirhosseini, R. M. Cross, S. M. Hashemi Rafsanjani and R. W. Boyd, **Science Advances**, 2, e1501143 (2016). Cover page (Exploring twisted light - The physics behind random optical fields).

[3] "Enhanced spectral sensitivity of a chip-scale photonic-crystal slow-light interferometer", O. S. Magaña-Loaiza, B. Gao, S. A. Schulz, J. Upham, K. Dolgaleva, and R. W. Boyd, **Optics Letters**, 41, 1431 (2016).

[4] "Amplification of Angular Rotations Using Weak Measurements", O. S. Magaña-Loaiza, M. Mirhosseini, B. Rodenburg, and R. W. Boyd, **Physical Review Letters**, 112, 200401 (2014).

[5] "Compressive Object Tracking using Entangled Photons", O. S. Magaña-Loaiza, G. A. Howland, M. Malik, J. C. Howell, and R. W. Boyd, **Applied Physics Letters**, 102, 231104 (2013). Editors' Choice article in **Science** Volume 341, Number 6141, Issue 5 July 2013.

[6] "Recent progress in weak value amplification and direct measurement", O. S. Magaña-Loaiza, M. Mirhosseini and R. W. Boyd, Book Chapter, **"Frontiers in Modern Optics"** , edited by D. Faccio, J. Dudley and M. Clerici (IOS Press, Amsterdam; DIF Bologna) pp. 77-122, (2016).

[7] "Weak-value measurements can outperform conventional measurements", O. S. Magaña-Loaiza, J. Harris, J. Lundeen, and R. W. Boyd, Invited Paper **Under Review**, (2016).

[8] "Multiplexing Free-Space Channels using Twisted Light", B. Rodenburg, O. S. Magaña-Loaiza, Mohammad Mirhosseini, Payam Taherirostami, Changchen Chen and R. W. Boyd, **Journal of Optics**, 18, 054015 (2016).

[9] "Wigner distribution of twisted photons", M. Mirhosseini, O. S. Magaña-Loaiza, Changchen Chen, Mohammad Hashemi Rafsanjani Rafsanjani and R. W. Boyd, **Physical Review Letters**, 116, 130402 (2016).

[10] "Light-drag enhancement by a highly dispersive rubidium vapor", A. Safari, I. De Leon, M. Mirhosseini, O. S. Magaña-Loaiza and R. W. Boyd, **Physical Review Letters**, 116, 013601 (2016).

[11] "The Quantum Hilbert Hotel", V. Potocek, F. M. Miatto, M. Mirhosseini, O. S. Magaña-Loaiza, A. C. Liapis, D. K. L Oi, R. W. Boyd and J. Jeffers, **Physical Review Letters**, 115, 160505 (2015), Synopsis.

[12] "State transfer based on classical nonseparability', S. M. Hashemi Rafsanjani, M. Mirhosseini, O. S. Magaña-Loaiza and R. W. Boyd, **Physical Review A**, 92, 023827 (2015).

[13] "High-dimensional quantum cryptography with twisted light", M. Mirhosseini, O. S. Magaña-Loaiza, M. N. O'Sullivan, B. Rodenburg, M. Malik, M. J. Padgett, D. J. Gauthier and R. W. Boyd, **New Journal of Physics**, 17, 033033 (2015), Highlights of 2015

[14] “Compressive Direct Measurement of the Quantum Wavefunction", M. Mirhosseini, O. S. Magaña-Loaiza, S.M. Hashemi Rafsanjani and R. W. Boyd, **Physical Review Letters**, 113, 090402 (2014).

[15] “Experimental generation of an optical field with arbitrary spatial coherence properties", B. Rodenburg, M. Mirhosseini, O. S. Magaña-Loaiza, and R. W. Boyd, **Journal of the Optical Society of America B**, Vol. 31, Issue 6, pp. A51-A55 (2014).

[16] “Simulating thick atmospheric turbulence in the lab with application to orbital angular momentum communication", B. Rodenburg, M. Malik, O. S. Magaña-Loaiza, M. Yanakas, L. Maher, N. K. Steinhoff, G. A. Tyler, R. W. Boyd, **New Journal of Physics**, 16, 033020 (2014).

[17] “Rapid Generation of Light Beams Carrying Orbital Angular Momentum”, M. Mirhosseini, O. S. Magaña-Loaiza, C. Chen, B. Rodenburg, M. Malik, and R. W. Boyd, **Optics Express**, Vol. 21, Issue 25, 30196-30203 (2013).

[18] “Enhancing entangled-state phase estimation by combining classical and quantum protocols ", H. Shin, O. S. Magaña-Loaiza, M. Malik, Malcolm N. O‘Sullivan and R. W Boyd, **Optics Express**, Vol. 21, Issue 3, 2816-2822 (2013).

[19] “Quantum-secured Imaging", M. Malik, O. S. Magaña-Loaiza and R. W. Boyd, **Applied Physics Letters**, 101, 241103 (2012).

[20] “Weak-value amplification of the fast-light effect in rubidium vapor”, M. Mirhosseini, G. Viza, O. S. Magaña-Loaiza, M. Malik, J.C. Howell and R. W. Boyd, **Physical Review A**, 93, 053836 (2016).

[21] “Interferometry with Photon-Subtracted Thermal Light”, S. M. Hashemi Rafsanjani, M. Mirhosseini, O. S. Magaña-Loaiza, B Gard, B. E. Koltenbah, C.G. Parazzoli, B. C. Capron, C.G. Gerry, J. P Dowling and R. W. Boyd, **Under review**, (2016).

[22] “Photon Added Coherent States: Nondeterministic, Noiseless Amplification in Quantum Metrology”, B Gard, D. Li, C. You, K. P. Seshadreesan, R. Birrittella, S. M. Hashemi Rafsanjani, O. S. Magaña-Loaiza, B. E. Koltenbah, C.G. Parazzoli, B. C. Capron, R. W. Boyd, C.G. Gerry, H. Lee, and, J. P Dowling, **Under review**, (2016).

Acknowledgments

I am deeply grateful for the guidance, patience, support and mentorship that Professor Robert W. Boyd provided me along my graduate studies. It has been a great opportunity and privilege to explore novel physics under his tutelage, he is the best Advisor. Prof. Boyd always gave me the freedom to work on different projects, including those that resulted from my curiosity. Also, I would like to express my gratitude to my committee members, Profs. Peter W. Milonni, Nicholas P. Bigelow, Qiang Lin and Anthony N. Vamivakas for helpful discussions and encouragement. I want to thank the chair of the committee, Prof. Michael C. Huang, my colleagues and group members: Prof. John Howell, Prof. Jonathan Dowling, Prof. John Jeffers, Prof. Christopher Gerry, Prof. Gerd Leuchs, Prof. Miles Padgett, Prof. Daniel Gauthier, Prof. Heedeuk Shin, Prof. Zhimin Shi, Prof. Martin Lavery, Prof. Anand Jha, Prof. Israel De Leon, Dr. Brandon Rodenburg, Dr. Mohammad Mirhosseini, Dr. Seyed Mohammad Hashemi Rafsanjani, Dr. Andreas Liapis, Dr. Robert Fickler, Dr. Jerry Kuper, Dr. Mehul Malik, Dr. Gerardo Viza, Dr. Joseph Vornehm, Dr. Sebastian Schulz, Dr. Jeremy Upham, Brian McIntyre, Per Adamson, Malcolm O´Sullivan, Robert Cross, Akbar Safari, Zahir Alam, Saumya Choudhary, Changchen Chen, Payam

Taherirostami, Boshen Gao, Zhe Yang, Jiapeng Zhao and Kashif Awan. I would like to specifically thank Dr. Svetlana Lukishova and Dr. Francisco Arteaga-Sierra for their friendship and wonderful discussions.

I appreciate all the help that the Materials Science and Optics staff gave me these years. More specifically, I would like to thank Carla Gottschalk, Lynda McGarry, Gina Eagan, Maria Schnitzler and Noelene Votens for helping me with paperwork and other complicated processes. I also want to thank Hugo Begin for all the help he provides me every time I visit the University of Ottawa.

I would also like to thank my former advisors Javier Sánchez-Mondragón and Roberto Salas-Corrales for their friendship and encouragement over the years.

I want to thank my family and friends for their support and the great times we have spent together. Thanks for the great parties, food and the adventures here and there. It is hard to list all the names of my friends and family members but at least I would like to mention and thank the best parents, Carmen Loaiza Reynaldo and Santiago Magaña Vazquez, for their unconditional support and for teaching me how to enjoy and live life to the fullest. I thank Carlos Magaña Loaiza for being the best brother and friend. I thank my grandmother Kika Reynaldo for all her love. I also want to thank my parents-in-law, Rosa Elvia Reyes Gutierrez and Armando Ybarra Varela, for their enthusiastic support and encouragement. Finally, I thank my beautiful wife Paloma Ybarra Reyes for being a great woman, friend and excellent wife and for the wonderful times we have had together. If my life was great, now it is

much better with our lovely son Mateo Santiago Magaña Ybarra. Mateo and Paloma have brought me happiness, joy and love. I thank God and la Virgen de Guadalupe for making everything possible.

Abstract

We describe our recent contributions to the field of optical coherence. We discuss a series of experiments that exploit a variety of novel mechanisms of optical interference to unveil new behaviors of light. More specifically, we discuss how we explored the conditions under which light is forced to exhibit new properties. These effects are not only fundamentally important but they open the door for a wide variety of applications.

In Chapter 1 we review the fundamental concepts that are utilized along the thesis. In Chapter 2 we discuss how extreme conditions in a quantum measurement process allowed us to exploit a form of spin-orbit interaction in an optical beam that produces weak values (WVs) in the azimuthal variables. These interferometric WVs lead to a shift in the angular position and orbital angular momentum (OAM) of an optical beam. The OAM spectrum is shifted as a consequence of the breakup in the polarization symmetry, realized by a differential geometric phase. We show how these effects can be used to amplify angular rotations. In the same chapter, we discuss another technique that uses interferometric WVs for direct measurement of the quantum wavefunction. We improve the state-of-the-art of this technique by incorporating compressive sensing

(CS) through the implementation of random projection operators. Our technique allowed us to demonstrate the measurement of a 19 200 dimensional state.

In Chapter 3, we introduce the Wigner distribution in the azimuthal space. The Wigner distribution in the angular domain provides valuable insight into understanding the wave behavior of the light field in the conjugate bases of OAM and azimuthal angle. In addition, we discuss how our technique allows one to determine the azimuthal first-order degree of coherence of a partially coherent beam.

In Chapter 4 we describe how the random fluctuations of light give rise to the formation of correlations in the OAM components and angular positions of pseudothermal light. The presence of these correlations is manifested through a new family of exotic interference structures in the OAM distribution of random light. We describe these effects in the context of the azimuthal Hanbury Brown and Twiss effect.

In Chapter 5, we exploit quantum correlations to perform quantum imaging. We present a CS protocol that tracks a moving object by removing static components from a scene. The implementation is carried out on a quantum imaging scheme to minimize both the number of photons and the number of measurements required to form a quantum image of the tracked object. This procedure tracks an object at low light level, permitting us to more effectively use the information content in each photon.

Another effect that has been recently predicted is the finite probability of a photon to follow looped paths in a three-slit interferometer. This produces an apparent

deviation from the most conventional form of the superposition principle. However, the probability of observing these exotic paths is very small and thus extremely hard to be measured. In Chapter 6, we discuss how we have increased the probability of photons to follow such looped trajectories and measured its contributions to the formation of interference fringes.

Contributors and Funding Sources

The thesis committee examining this dissertation is comprised of Prof. Robert W. Boyd, Prof. Peter W. Milonni, Prof. Nicholas P. Bigelow, Prof. Nick Vamivakas and Prof. Qiang Lin. The committee is chaired by Prof. Michael C. Huang from the department of Electrical and Computer Engieering at the University of Rochester. The research performed during my time as doctoral student is a result of many collaborations within the quantum photonics research group, as well as outside of it.

My PhD program has been funded by many sources and agencies. I would like to thank The University of Rochester, Defense Advances Research Projects Agency (DARPA), National Aeronautics and Space Administration (NASA), Defense Threat Reduction Agency (DTRA), the US Office of Naval Research (ONR), KBN Optics, Secretaría de Educación Pública (SEP) and Consejo Nacional de Ciencia y Tecnología (CONACYT) for all the support. However, I would like to acknowledge CONACYT for supporting the majority of my graduate studies.

The information discussed in Chapter 2 has been adapted from two peer-reviewed publications. The work in [1] was conceived and led by Omar S. Magaña-Loaiza,

this work was published in Physical Review Letters. The work in [2] was conceived and led by Mohammad Mirhosseini and published in Physical Review Letters. Both experiments were performed in the laboratory of Professor Robert Boyd with contributions from Brandon Rodenburg, Seyed Mohammad Hashemi Rafsanjani and Professor Boyd. This research was supported by DARPA/DSO InPho program, the U.S. Defense Threat Reduction Agency (Grant No. HDTRA1-10-1-0025), the Canadian Excellence Research Chair (CERC) program and CONACYT.

The work presented in Chapter 3 is adapted from a paper published in Physical Review Letters [3]. This work was led by Mohammad Mirhosseini and involved efforts of Changchen Chen, Seyed Mohammad Hashemi Rafsanjani, Prof. Boyd and Omar S. Magaña-Loaiza. This work was supported by the US ONR, CERC, CONACYT and SEP.

The content of Chapter 4 is primarily adapted from a paper published in Science Advances [4]. This work was conceived and led by Omar S. Magaña-Loaiza and involved efforts of Mohammad Mirhosseini, Robert M. Cross, Seyed Mohammad Hashemi Rafsanjani and Prof. Boyd. This experiment was carried out in the laboratory of Professor Robert Boyd in Rochester. This work was supported by the U.S. Office of Naval Research, CERC, CONACYT, and SEP.

The work presented in Chapter 5 was adapted from a paper published in Applied Physics Letters [5] and led by Omar S. Magaña-Loaiza. This work was performed in collaboration with Professor John C. Howell and involved efforts of Gregory Howland,

Mehul Malik, Professor Howell and Professor Boyd. This experiment was performed in the laboratory of Professor John Howell. This work was supported by the DARPA AFOSR GRANT FA9550-13-1-0019 and the CONACYT.

The research discussed in Chapter 6 was conceived and led by Omar S. Magaña-Loaiza. This work was performed in collaboration with Israel de Leon, Mohammad Mirhosseini, Robert Fickler, Akbar Safari, Mick Uwe, Brian McIntyre, Peter Banzer, Brandon Rodenburg, Professor Gerd Leuchs and Professor Boyd. This experiment was performed in the laboratory of Professor Boyd at the University of Ottawa. This work was supported by CERC, KBN optics and internal funds from the University of Rochester.

Table of Contents

List of Figures

Chapter 1

Key Concepts

1.1 Introduction

The superposition principle underlies the most fundamental and beautiful effects in physics. This interesting property is at the heart of any wave theory, including quantum mechanics and coherence theory [7]. Despite the fact that these theories are the result of hundreds of years of intense research performed by the most brilliant minds in physics, the superposition principle and some of its remarkable manifestations, such as interference effects, have not been completely deciphered and keep amazing the scientific community [8]. Nowadays, interference is considered as the only mystery of quantum physics [9].

Undoubtedly, the understanding of the properties of light have permitted scientists to formulate some of the most exciting postulates in modern physics. For example, in the early 19th century the first demonstration of interference was performed by

Thomas Young utilizing sunlight [10]. This experiment played a fundamental role in the acceptance of the wave theory of light and demonstrated to be of paramount importance in the formulation of quantum mechanics and the wave-particle duality of quantum particles [7–10]. In recent years, this experiment has been utilized to demonstrate the difference between classical and quantum interference and to illustrate the probabilistic nature of the former [11]. The two-slit experiment devised by Young involves a single field of light (one-photon field), however interference effects have been observed with two-photon fields, three- and four-photon fields and some other excitation modes [8]. The study of interference and coherence effects that involve multi-photon processes started with the experiments performed by Hanbury-Brown and Twiss (HBT) in the nineteen fifties [12]. Interestingly, their experiment now known as the HBT experiment unveiled novel and surprising aspects of light. The ability to observe interference from chaotic light produced by independent sources on the disk of a star and detected at different locations on Earth resulted in very intriguing because at that time it appeared that classical and quantum theories of light offered different predictions. This experiment started the field of quantum optics and motivated a wide variety of experiments such as the Hong-Ou-Mandel and the Franson interferometers just to mention a few [13, 14]. Surprisingly, even in these days, interference effects with light offer the possibility to study fundamental problems that represent open questions in physics [9].

In this thesis we describe a series of experiments that we performed to unveil novel and exceptional behaviors of light [15]. We believe that our findings contribute in a significant manner to the field of optical coherence. Furthermore, we discuss how some of these effects have serious implications in the development of new generations of optical technologies. This first chapter is organized as follows. In section 1.2 we present a conceptual description of first-order interference and coherence. The orbital angular momentum (OAM) of light is discussed in section 1.3. The basic concepts of first-order interference in the angular degrees of freedom are provided in section 1.4. In section 1.5, we discuss weak values and how they can be understood as an interference phenomenon. Finally, a summary of the topics treated in this thesis is presented in section 1.6.

1.2 Spatial first-order interference of light

The advent of the laser gave an enormous impulse to the development of the theory of optical coherence. A theory that deals with the study of the correlation properties of light, more specifically, coherence theory provides a metric for the similarities among different temporal periods or spatial positions associated to an electromagnetic field [15]. In this section, we provide a brief review of the concept of spatial coherence, a property that will be used in several parts of this thesis.

Young's experiment has been widely used in different fields of physics. Originally this setup was utilized to prove the wave nature of light. However, this experiment can also be utilized to illustrate the concept of the spatial degree of first-order mutual coherence of two interfering waves [7–10, 15]. For this purpose, we utilized the setup depicted in Fig. 1.1. We assume that the slits are illuminated with a quasi monochromatic source of light with a beam waist located at $z = 0$. We also assume that the transverse profile of the source is partially coherent.

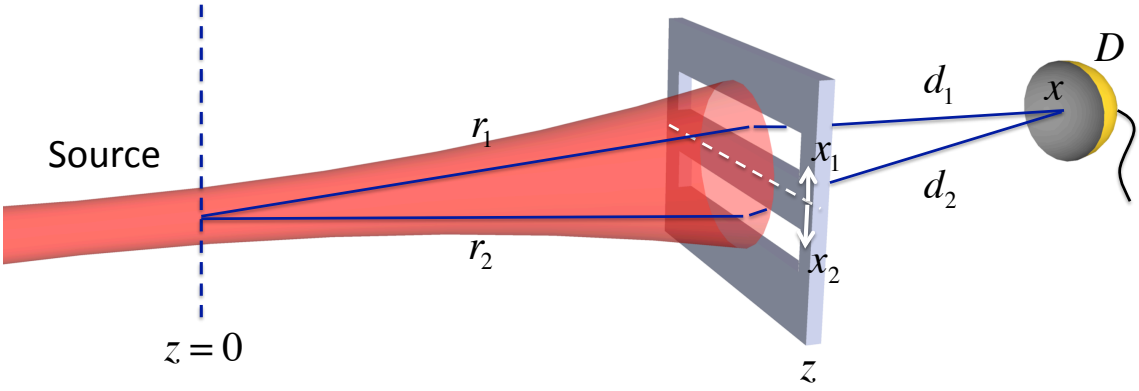

Figure 1.1: Schematic representation of a Young's double-slit interferometer used to illustrate first-order interference and first-order coherence. The quantities r_1 and r_2 represent the distances from the center of the source beam at plane $z = 0$ to the upper and lower slits, respectively. The two slits are separated by Δx defined as $x_1 - x_2$, where x_1 represents the transverse position of the upper slit and x_2 represents the position of the lower slit. The distances from the upper and lower slits to the detector D are represented by d_1 and d_2 respectively.

The definition of first-order coherence can be quantified through the evaluation of the intensity measured by the detector located in the far-field of the two-slit arrangement at the transverse position x. The total electric field at the detector $E_d(x)$ is given by the sum of the field amplitudes $E(x_1, z)$ and $E(x_2, z)$ produced by each of

the slits. This can be expressed as

$$E_d(x) = a_1 E(x_1, z) e^{ik_0 d_1} + a_1 E(x_2, z) e^{ik_0 d_2}. \tag{1.1}$$

The magnitude of the wave-vector in vacuum is represented by k_0 and the distances from the upper and lower slits to the detector D are represented by d_1 and d_2 respectively. The coefficients a_1 and a_2 represent the amount of light transmitted from the slits, the values for a_1 and a_2 are defined by the geometry of the slits. The intensity measured by the detector is given by the ensemble average of the instantaneous intensities $E_d^*(x)E_d(x)$. This quantity is defined as

$$I_d(x) = \langle E_d^*(x)E_d(x)\rangle = a_1^2 I_1(x_1, z) + a_2^2 I_2(x_2, z) + a_1 a_2 \Gamma(x_1, x_2, z) e^{-ik_0(d_1 - d_2)} + c.c., \tag{1.2}$$

where I_1 is defined as $\langle E^*(x_1, z)E(x_1, z)\rangle$ and I_2 as $\langle E^*(x_2, z)E(x_2, z)\rangle$. These quantities describe mutual field correlations and are examples of first-order coherence functions. The cross-field correlation at plane z is described by $\Gamma(x_1, x_2, z)$. The Gaussian Schell-model beams are a common example of a partially coherent beam [16]. Such a beam is defined by having a Gaussian intensity $I = e^{-x^2/2\sigma_I^2}$, as well as a Gaussian degree of coherence $\Gamma(x_1, x_2) = \sqrt{I_1(x_1, z) I_2(x_2, z)} e^{-|x_1 - x_2|^2/2\sigma_\mu^2} e^{-ik_0(r_1 - r_2)}$, where r_1 and r_2 are the distances from the center of the beam at the origin to slit 1

and 2, respectively. Now the intensity measured by the detector can be rewritten as

$$I_d(x) = a_1^2 I_1(x_1, z) + a_2^2 I_2(x_2, z) + 2a_1 a_2 \sqrt{I_1(x_1, z) I_2(x_2, z)} e^{-|\Delta x|^2 / 2\sigma_\mu^2} \cos(k_0 \Delta s), \quad (1.3)$$

where Δs is equal to $r_1 + d_1 - r_2 - d_2$. This result demonstrates that the formation of interference fringes occurs only when the length of the spatial coherence of the illuminating beam is larger than the separation of the two slits. In Chapter 5, we discuss a case in which interference fringes are formed even for a situation in which the length of spatial coherence is smaller than the separation of the two slits, in this case coherence is induced by the presence of exotic looped trajectories.

1.3 Orbital angular momentum of light

In addition to spin angular momentum (SAM) of light that arises from its polarization properties, light can also carry OAM [17]. For example, a beam of light with a helical phase front given by an azimuthal phase dependence of the form $e^{i\ell\phi}$ carries OAM, in general these beams have the following form

$$E(x, y, z, \phi) = u_0(x, y, z) e^{-ikz} e^{i\ell\phi}, \quad (1.4)$$

which describes a beam of light with a slowly varying amplitude distribution $u_0(x, y, z)$ propagating along z, k represents the wave number. Interestingly, beams with these

properties are solutions to the paraxial approximation of the Helmholtz equation, which is written in a cartesian coordinate system as

$$\left(\frac{\partial^2}{\partial x^2}+\frac{\partial^2}{\partial y^2}+2ik\frac{\partial^2}{\partial z^2}\right)E(x,y,x)=0. \tag{1.5}$$

This equation is satisfied by cylindrical Laguerre-Gaussian modes $LG_p^\ell(\rho,\phi,z)$, which consist of a family of orthogonal modes that have a well defined value of OAM. The field amplitude of a normalized Laguerre-Gauss mode is given by

$$\begin{aligned} LG_p^\ell(\rho,\phi,z) = \sqrt{\frac{2p!}{\pi(|\ell+p|)!}}\frac{1}{w(z)}\left[\frac{\sqrt{2}\rho}{w(z)}\right]^{|\ell|} L_p^\ell\left[\frac{2\rho^2}{w^2(z)}\right]\exp\left[-\frac{\rho^2}{w^2(z)}\right] \\ \exp\left[-\frac{ik^2\rho^2 z}{2(z^2+z_R^2)}\right]\exp\left[i(2p+|\ell|+1)\tan^{-1}\left(\frac{z}{z_R}\right)\right] \end{aligned} \tag{1.6}$$

where p is the radial mode index, $w(z)$ is the beam waist given by $\sqrt{2(z^2+z_R^2)/k_{z_R}}$, z_R is the Rayleigh range defined as $kw^2(0)/2$, $L_p^{|\ell|}$ is the associated Laguerre polynomial and r, ϕ denote the transverse coordinates. Each photon in a Laguerre-Gaussian mode carries an orbital angular momentum of $\ell\hbar$ [17].

The simplest examples of the modes that carry OAM are shown in Fig. 1.2. These modes have a top-hat intensity structure and their azimuthal phase dependence is shown from Fig. 1.2 a) to c). These phase distributions correspond to the values of OAM given by $\ell=1$, $\ell=2$ and $\ell=3$ respectively. The twisted wavefront of the beam shown in Fig. 1.2 d) is a consequence of the OAM of light induced by the azimuthal phase dependence of the form $e^{i\ell\phi}$.

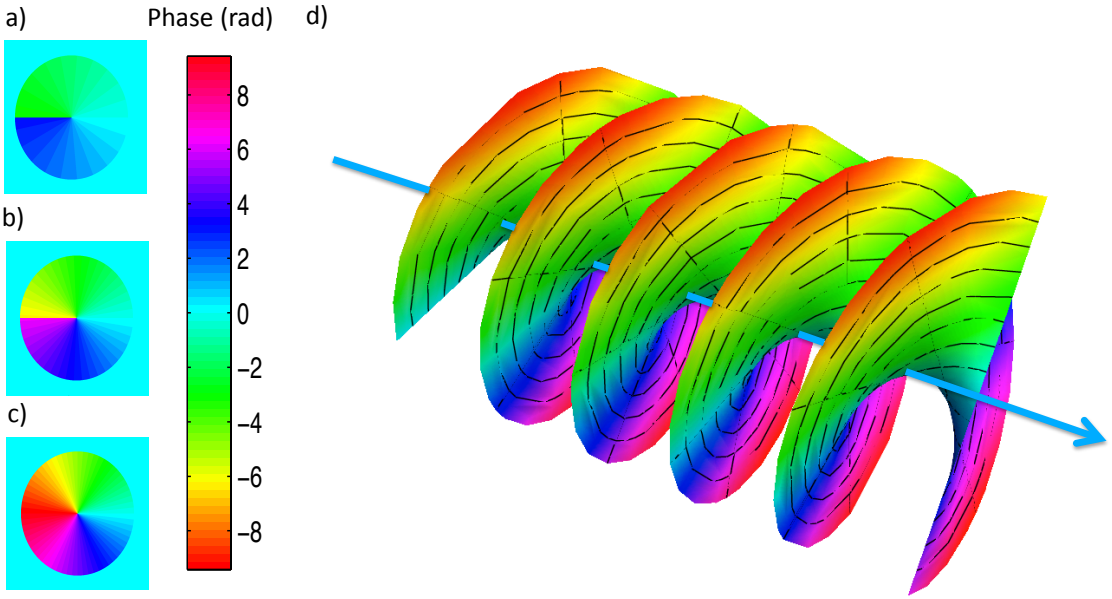

Figure 1.2: The azimuthal phase dependence for beams of light carrying different values of OAM is shown from a) to c). The value for $\ell = 1$ is shown in a), $\ell = 2$ in b) and $\ell = 3$ in c). The wavefront of a beam of light carrying OAM is shown in d).

There are different ways in which beams carrying OAM can be generated and detected [18]. In the work presented in this thesis, we utilized computer generated holograms and spatial light modulators (SLMs). The encoded holograms contain the phase information that endows light with OAM and a diffraction grating that allows one to increase the quality of the generated modes [18]. As shown in Fig. 1.3 a), a SLM and a lens allows one to select a diffracted beam that carries specific values of OAM. Interestingly, the exact same technique can be used in reverse to characterize the OAM spectrum of light, see Fig. 1.3 b). The fact that the singularity of a beam carrying OAM can be removed by projecting it onto the conjugate azimuthal phase allows one to determine the OAM spectrum of light. In Fig. 1.3 b) a beam of light

carrying a specific value of OAM ℓ is projected onto $-\ell$, this produces a Gaussian mode, which is the only mode that couples efficiently onto a single mode fiber. If the beam is projected onto a different mode only a small amount of light is coupled to the fiber. In general this procedure allows for the determination of the OAM spectrum of light.

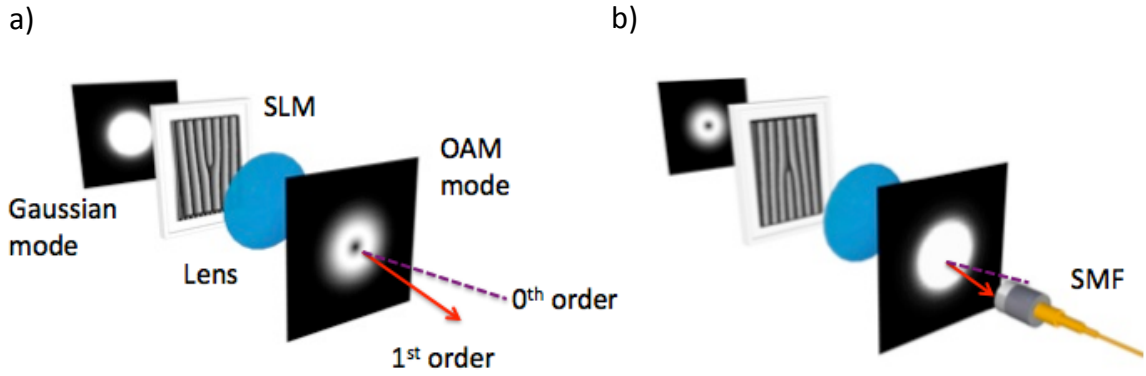

Figure 1.3: Generation and detection of beams of light carrying OAM. a) shows a spatial light modulator (SLM) displaying a computer-generated hologram that allows one to generate beams of light carrying specific values of OAM. The engineered mode is selected from the first diffraction order in the Fourier plane of the SLM. As shown in b) a similar forked diffraction grating displayed onto the SLM can also be utilized to measure the OAM spectrum of light.

1.4 Azimuthal first-order interference of light

Several experiments presented in this thesis exploit the azimuthal properties of light. Consequently, it is convenient to devote a section of this chapter to discuss the Fourier relationship existing between the angular position and OAM variables of an optical

beam [19, 20]. Later, these concepts are utilized to illustrate the simplest form of azimuthal interference also known as azimuthal first-order interference.

Similarly to linear position and linear momentum, angular position and OAM are conjugate variables and they form a Fourier pair [19, 20]. The Fourier relations are expressed as follows

$$\hat{\psi}(\ell) = \frac{1}{\sqrt{2\pi}} \int_{-\pi}^{\pi} d\phi \psi(\phi) \exp\left(-i\ell\phi\right); \tag{1.7}$$

$$\psi(\phi) = \frac{1}{\sqrt{2\pi}} \sum_{\ell=-\infty}^{\infty} \hat{\psi}(\ell) \exp\left(i\ell\phi\right). \tag{1.8}$$

Here $\hat{\psi}(\ell)$ represents the probability amplitude that a photon is carrying the OAM number ℓ, whereas $\psi(\phi)$ is the probability amplitude that the angular position of the photon is ϕ. From these relations, it is important to note that a rotation $\Delta\phi$ will induce a phase that is ℓ-dependent and is given by $\Delta\phi\ell$.

The Fourier relations described by Eqs. 1.7 and 1.8 can be illustrated with the cartoon shown in Fig. 1.4. It is shown that a beam with a uniform spatial profile does not carry OAM and consequently the OAM spectrum is centered at zero. In contrast, a beam shaped in a form of angular wedge shows a broader OAM spectrum. The spectrum is broad for angular modes with narrow widths and narrow for broad angular modes. This behavior is a manifestation of the uncertainty principle for the azimuthal variables of angular position and OAM.

The existence of a Fourier relationship for the angular variables of angular position and OAM gives rise to interesting interference effects [4, 21]. For example, let

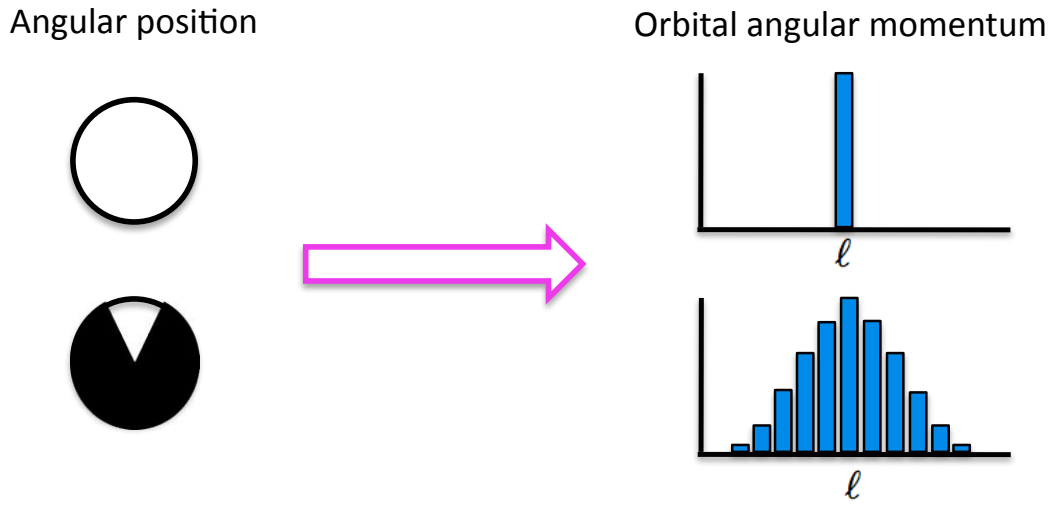

Figure 1.4: Fourier relationship between angular position and OAM. A broad OAM spectrum is observed for an angular mode with narrow width. This is a manifestation of the uncertainty principle for the conjugate variables in azimuthal degree of freedom.

us consider the azimuthal version of the famous Young's double-slit interferometer depicted in Fig. 1.5 a). In this case we assume that a spatially coherent beam illuminates a pair of angular slits of width α that are separated by the angle $\Delta\phi$. As one would expect, interference fringes must be formed in the conjugate variable, in this case in the OAM domain. As explained in the previous section of this chapter, a direct form of accessing to the OAM of light is by performing a series of OAM projections by means of a SLM. The light diffracted by the SLM is collected by a single mode fiber (SMF) and measured by a detector.

The interference fringes in this experimental setup are produced by the following superposition

$$\psi(\ell_t) = \psi(\ell_s) + e^{i\ell\Delta\phi}\psi(\ell_s), \tag{1.9}$$

in this case the wavefunction $\psi(\ell_s)$ describes the OAM spectrum produced by any of the two slits, this wavefunction is determined by the Fourier transform of the angular slit as defined in Eq. 1.7. However for the characteristics of the slit, this can be simplified to

$$\psi(\ell_s) = \frac{1}{\sqrt{2\pi}} \int_{-\alpha/2}^{\alpha/2} d\phi e^{-i\ell\phi}, \tag{1.10}$$

in this case $\psi(\ell_s)$ is defined as $\frac{\alpha}{\sqrt{2\pi}} \operatorname{sinc}(\frac{\ell\alpha}{2})$. Consequently, the probability amplitude $\psi(\ell_t)$ at the detector can be rewritten as

$$\psi(\ell_t) = \frac{\alpha}{\sqrt{2\pi}} \operatorname{sinc}\left(\frac{\ell\alpha}{2}\right)[1 + e^{-i\ell\Delta\phi}]. \tag{1.11}$$

This superposition produces an intensity distribution in the OAM spectrum given by

$$I(\ell_t) = \frac{\alpha^2}{\pi} \operatorname{sinc}^2\left(\frac{\ell\alpha}{2}\right)[1 + \cos(\ell\Delta\phi)]. \tag{1.12}$$

An example of the interference pattern described by Eq. 1.12 for a situation in which α is $\pi/6$ and $\Delta\phi$ is $\pi/12$ is shown in Fig. 1.5 b). The discreteness of the pattern is caused by the discrete measurements of OAM performed by means of a SLM.

1.5 Weak Values

Bayes's theorem has played a fundamental role in classical and quantum measurement theory.

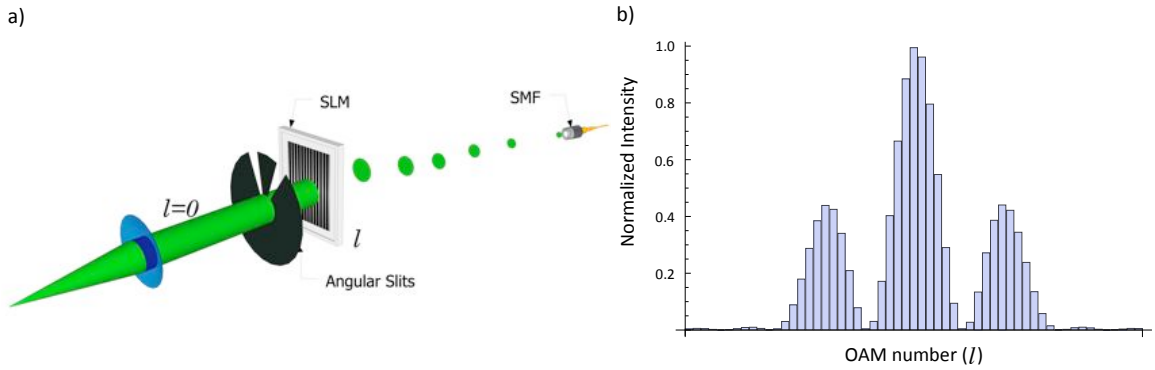

Figure 1.5: Azimuthal version of the Young's double-slit interferometer. An schematic version of the setup used to observe first-order azimuthal interference is depicted in a). An example of the interference pattern measured by a detector after the single mode fiber (SMF) is shown in b). In this case α is $\pi/6$ and $\Delta\phi$ is $\pi/12$.

As in any branch of science, the measurement process is of fundamental importance in quantum physics. However due to the nature of the formulation of quantum mechanics, different forms of measurements, or exotic implementations of Bayesian statistics, have led to the observation of counter intuitive physical effects [22]. Examples include superluminal pulse propagation, the determination of the trajectory followed by a single photon in a two-slit interferometer, amplification of observables, etc. [6, 22–25]. In addition to the fundamental character of these effects, recent work suggests that some of them could have strong implications for technological applications, such as in quantum communication, quantum information, and metrology [1, 26–36].

In 1988 Aharonov, Albert and Vaidman introduced a generalized form of quantum measurement known as weak measurement [22]. The original paper with the title "How the result of a measurement of a component of the spin of a spin-$\frac{1}{2}$ particle

can turn out to be 10" created heated debates and motivated a new generation of experiments that eventually verified the counterintuitive prediction [6, 23–25, 37]. In this section, we discuss some of the effects that give rise to the apparent "weird" features that make weak measurements interesting and controversial.

In this introductory section we use the von Neumann model to explain weak measurements. In this model, the total system is composed of two subsystems, one is the system we wish to measure, described by the state $|\Psi_{\rm s}\rangle$, typically called the probe. The other is the pointer device $|\Psi_{\rm d}\rangle$ that provides information about the measured system [26]. The correlation between these subsystems arises when the observable of the system $\hat{\sigma}$ is coupled or entangled to the pointer, through its linear momentum $\hat{p}$. This can be described by the following interaction Hamiltonian

$$\hat{H}_{\rm int} = g\hat{\sigma}\hat{p}, \tag{1.13}$$

where g is a real quantity that acts as coupling constant. The initial state can be described as the product of the state of the system or probe and the state of the pointer device as $|\Psi_{\rm i}\rangle = |\Psi_{\rm s}\rangle\,|\Psi_{\rm d}\rangle$. Further, the state $|\Psi_{\rm s}\rangle$ can be expressed as $\sum_{\rm n} s_{\rm n}\,|S_{\rm n}\rangle$, in terms of the eigenstates of the operator $\hat{\sigma}$ as a consequence of the spectral theorem. After the interaction of duration Δt, the subsystems are coupled in the following manner

$$|\Psi_{\rm f}\rangle = e^{-i\hat{H}_{\rm int}\Delta t}\,|\Psi_{\rm i}\rangle = \sum_{\rm n} s_{\rm n}\,|S_{\rm n}\rangle\,|\Psi_{\rm d}(x-\chi s_{\rm n})\rangle\,, \tag{1.14}$$

where χ equals $g\Delta t$. In obtaining this result we have recalled the fact that the momentum $\hat{p}$ is the generator of translations in x. The state $|\Psi_{\mathrm{f}}\rangle$ demonstrates that system and pointer have been coupled; this effect is sometimes referred as classical entanglement [38, 39]. In addition, the position of the center of the pointer state has been shifted. If one were to calculate the expectation value of the position operator $\langle\hat{X}\rangle$ in the final state $|\Psi_{\mathrm{f}}\rangle$, under ideal circumstances this will be equal to $\chi\langle\hat{\sigma}\rangle$. This result shows that the position of the pointer can be used to estimate the expectation value of the operator $\hat{\sigma}$, which explains the origin of the name of pointer. It is worth noticing that the strength of the coupling constant has not been constrained. This form of measurement is known as strong perturbative measurement [22]. Typically, the probability distribution of the pointer is assumed to be a Gaussian function; however, different pointers and their advantages have been studied [40]. The random noise or error associated with a measurement or read-out process is typically described by a Gaussian distribution.

An example of strong measurement is depicted in Fig. 1.6 a). Here, the transverse spatial position of a Gaussian beam acts as the pointer and its polarization as the probe. The beam of light with diagonal polarization passes through a tilted birefringent crystal, which provides the interaction Hamiltonian for measuring the operator $\hat{\sigma}$. At the output of the crystal, the position and polarization of the emerging beams are well defined due to the strong interaction that occurred in the crystal, caused by its birefringence. In a typical (strong) measurement, the separation between the

horizontally and vertically polarized beams is much larger than the sum of the beam waist sizes, making it easy to resolve the two beams with minimal uncertainty in the measurement of the polarization state of each photon.

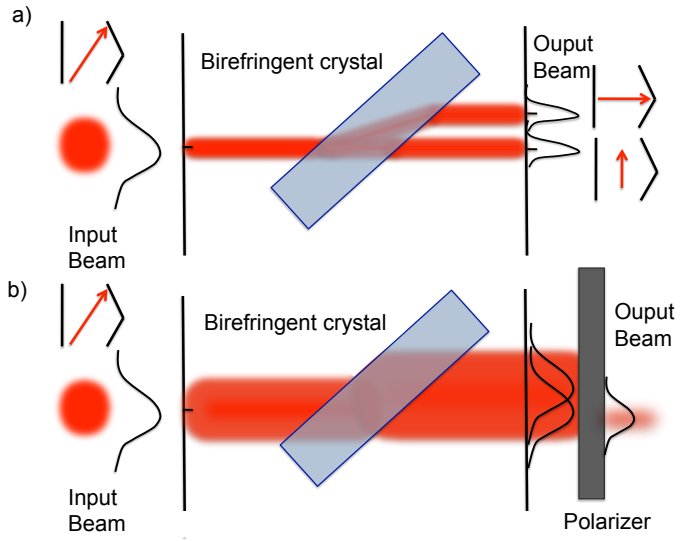

Figure 1.6: Schematic diagram of the experimental setup used to perform strong and weak measurements. a) a birefringent crystal shifts the horizontal and vertical polarized components of the input beam, which is diagonally polarized. The induced shift is larger than the beam waist diameters of the emerging beams; this strong interaction thus allows the determination of the polarization of the two beams, via strong or projective measurement. The measurement process permits one to infer information about the strength of the interaction, in this case the birefringence of the material. b) a weaker interaction between the input beam and the birefringent crystal produces a small displacement between the two emerging beams. In this case, the beam displacement is much smaller than the waist diameter of the beams. Thus it is difficult to determine the polarization of each beam. In this case, the post-selection process forces the two beams to coherently interfere, producing another beam with a Gaussian profile. When the position of the post-selection polarizer is almost orthogonal to the input polarization, the center of the post-selected beam is shifted by an amount proportional to the small separation between the two emerging beams multiplied by the weak-value amplification factor.

In weak measurements, the initial state of the system remains mostly intact, and information is obtained by weakly disturbing the system. As a consequence, the

uncertainty in each single-photon measurement is large. However, the uncertainty is generally overcome by averaging over a large number of events. The post-selection process makes weak measurements interesting. For example, the outcome of a weak measurement, called a weak value (WV), need not be an eigenvalue of the measurement operator [6, 22, 26]. In addition, WVs can be complex or exceed the eigenvalue range of a strong or projective measurement. The properties of WVs can be understood if we use the von Neumann model. In this case, we assume that the perturbation or coupling χ is small. The state after the weak perturbation can be written by expressing the interaction Hamiltonian as a power series

$$|\Psi_{\mathrm{f}}\rangle = e^{-i\hat{H}_{\mathrm{int}}\Delta t}\,|\Psi_{\mathrm{i}}\rangle = |\Psi_{\mathrm{s}}\rangle\,|\Psi_{\mathrm{d}}\rangle - i\chi\hat{\sigma}\,|\Psi_{\mathrm{s}}\rangle\,\hat{p}\,|\Psi_{\mathrm{d}}\rangle + ... \tag{1.15}$$

After the weak perturbation, a post-selection is applied to the system. In general, the post-selection can be performed on any variable, such as polarization, linear momentum, OAM, etc. In fact, this flexibility has allowed scientists to apply weak measurements to different scenarios and degrees of freedom [1, 25, 27, 28, 30–34]. Therefore, our post-selection is performed by applying the projective operator $|\mathrm{Ps}\rangle\langle\mathrm{Ps}|$ to the state $|\Psi_{\mathrm{f}}\rangle$, leading to the following state

$$|\Psi_{\mathrm{F}}\rangle = |\mathrm{Ps}\rangle\langle\mathrm{Ps}|\,|\Psi_{\mathrm{f}}\rangle = [\langle\mathrm{Ps}|\Psi_{\mathrm{s}}\rangle\,|\Psi_{\mathrm{d}}\rangle - i\chi\,\langle\mathrm{Ps}|\,\hat{\sigma}\,|\Psi_{\mathrm{s}}\rangle\,\hat{p}\,|\Psi_{\mathrm{d}}\rangle + ...]\,|\mathrm{Ps}\rangle\,. \tag{1.16}$$

Due to the weakness of the interaction, this expression can be approximated to the first order and then normalized to give

$$|\Psi_{\mathrm{F}}\rangle \approx \left(|\Psi_{\mathrm{d}}\rangle - i\chi \frac{\langle \mathrm{Ps}|\,\hat{\sigma}\,|\Psi_{\mathrm{s}}\rangle}{\langle \mathrm{Ps}|\Psi_{\mathrm{s}}\rangle}\hat{p}\,|\Psi_{\mathrm{d}}\rangle\right)|\mathrm{Ps}\rangle\,. \tag{1.17}$$

The post-selection process collapses the state of the probe, in this case $|\Psi_{\mathrm{s}}\rangle$. In addition, the post-selection reveals the weak value of the operator $\hat{\sigma}$. The weak value is defined as

$$\sigma_{\mathrm{w}} = \frac{\langle \mathrm{Ps}|\,\hat{\sigma}\,|\Psi_{\mathrm{s}}\rangle}{\langle \mathrm{Ps}|\Psi_{\mathrm{s}}\rangle}, \tag{1.18}$$

and it is important to stress that this is a general definition that can be applied to any operator defined for any degree of freedom or in any Hilbert space. Besides the collapse of the state of the system $|\Psi_{\mathrm{s}}\rangle$, the post-selection process also induces a shift in the state of the pointer device $|\Psi_{\mathrm{d}}\rangle$. Remarkably, this shift is proportional to the weak value and to the small disturbance χ as described by

$$|\Psi_{\mathrm{F}}\rangle = |\Psi_{\mathrm{d}}(x - \chi\sigma_{\mathrm{w}})\rangle\,|\mathrm{Ps}\rangle\,. \tag{1.19}$$

The WV σ_{w} can take very large values when the states $|\mathrm{Ps}\rangle$ and $|\Psi_{\mathrm{s}}\rangle$ are almost orthogonal, as can be seen from Eq. 1.18. Furthermore, when one of the coefficients of either of the two states is complex, the weak value can be complex. Such unusual

features have generated a great amount of interest in weak measurements. A detailed review of this field can be found in [26].

Under many practical circumstances, weak values and weak measurements can be understood in terms of entirely classical interference arguments. Nonetheless, much of the recent work on weak measurements employs the simple and mathematically elegant language of quantum mechanics to describe these effects. The reason is that quantum mechanics provides a simpler description and the results apply to a wider range of phenomena than for the case of a classical description.

In 1991, Ritchie *et al.* performed the first realization of a weak value [25]. A simplified version of their experimental setup is depicted in Fig. 1.6 b). Here, we assume a weak interaction between the beam and the crystal. This interaction produces a weak coupling of the spatial profile with the polarization degree of freedom, which means that the two polarization components of the beam travel along different optical paths and become transversely separated. In this weak-interaction regime, the two beams emerging from the quartz plate are spatially separated by an amount that is much smaller than the beam waist size. For example, if one were to determine the birefringence of the material by measuring the actual position of the two beams, this will be an ineffective technique. The variance of the pointer is large, and thus the measurement will not be precise. However, the post-selection process makes this experiment interesting, since it allows discarding results that do not provide useful information and keeping those that convey relevant and conditioned information. As

we will discuss, this exotic form of performing statistics can be implemented in different forms. In Ritchie's experiment the post-selection is performed with a polarizer. When the position of the post-selection polarizer is almost orthogonal to the polarization of the injected beam, the amount of transmitted light is low. Nevertheless, because of the optical interference between the two emerging beams, the spatial centroid of the post-selected beam is shifted by an amount proportional to the product of the small separation between the two beams and the weak value. So, weak values offer an alternative form of determining small quantities or weak effects.

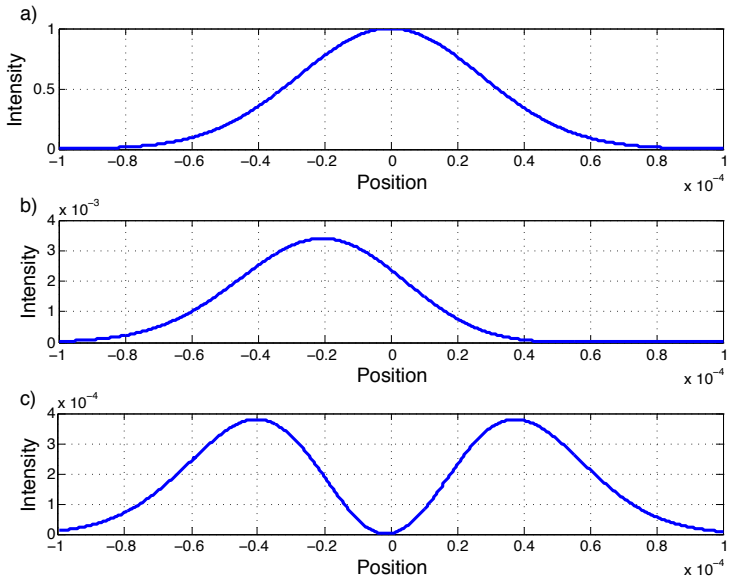

Figure 1.7: Numerical simulations that illustrate three regimes of the experimental setup depicted in Fig. 1.6 b). The transverse profile produced by constructive interference between two identical Gaussian beams with a beam waist of 55 μm separated by 2.5 μm is shown in a). One of the beams is horizontally polarized whereas the other is vertically polarized, the post-selection angle of the polarizer is 45°. b) the angle of the post-selection polarizer is set to $90° + \epsilon$ with respect to the polarization of the input beam, where ϵ equals 2.8°, this is the weak measurement regime. The shift in the pointer is proportional to the product of the weak value and the small separation between the two interfering beams. c) in this case ϵ is 0° and the weak value is not defined.

The essence of Ritchie's experiment is shown in Fig. 1.7. We have simulated different regimes for the experimental setup depicted in Fig. 1.6 b). We assume a beam with a Gaussian intensity distribution and a beam waist of 55 μm. The result of the constructive interference between the two beams separated by 2.5 μm is shown in Fig. 1.7 a). In Fig. 1.7 b) the angle of the post-selection polarizer is set to $90^\circ + \epsilon$ with respect to the polarization of the input beam, where ϵ equals 2.8°; this is the weak measurement regime. The shift in the state of the pointer is eight times larger than the separation of the beams emerging from the crystal. This value can be increased by decreasing either ϵ or the separation between the two beams; however, the amount of light passing through the post-selection polarizer would then decrease. In fact, this is an important limitation in the protocols for weak value amplification (WVA); stronger post-selections or larger amplifications imply the loss of more photons through post selection. Furthermore, the weak value is not defined for very small values of ϵ. Fig. 1.7 c) illustrates a situation where the post-selection angle is orthogonal to the polarization of the input beam, that is, $\epsilon = 0^\circ$.

In the work of Ritchie and co-workers, the measured weak value was real and this was measured by observing the shift in the position of the pointer. Nonetheless, as we have pointed out earlier, a weak value can be complex, and therefore one should be able to measure both the real and imaginary part of the weak value. Several authors have shown that the shift in the position and momentum of the pointer is proportional to the real and imaginary part of the weak value [41, 42], respectively.

The expectation values of the position and momentum operator for the post-selected state $|\Psi_{\mathrm{F}}\rangle$ described by Eq.1.19 can be calculated as

$$\langle \hat{X} \rangle_{\mathrm{F}} = \chi \Re \left(\frac{\langle \mathrm{Ps}| \, \hat{\sigma} \, |\Psi_{\mathrm{s}}\rangle}{\langle Ps|\Psi_{\mathrm{s}}\rangle} \right), \tag{1.20}$$

$$\langle \hat{P} \rangle_{\mathrm{F}} = \frac{2\chi}{\sigma^2} \Im \left(\frac{\langle \mathrm{Ps}| \, \hat{\sigma} \, |\Psi_{\mathrm{s}}\rangle}{\langle Ps|\Psi_{\mathrm{s}}\rangle} \right). \tag{1.21}$$

These relations have motivated a wide variety of experiments during the last 10 years.

In 2011, Lundeen *et al.* proposed a technique known as direct measurement of the quantum wavefunction. This technique utilizes weak values to measure the wavefunction of a quantum particle in a direct fashion [6]. The simplicity of this technique and the fact that it does not require a time-consuming post-processing makes it attractive. The principles of quantum mechanics forbid the exact determination of the wave function of a particle in a single measurement. However, direct measurement utilizes many measurements on identically prepared systems to determine the weak values and subsequently the quantum state.

Efficient characterization of a quantum state is a crucial part of a variety of experiments in quantum optics. Recently, direct measurement has been utilized to reconstruct complicated wavefunctions and high-dimensional states defined on different Hilbert spaces [2, 35, 36].

The main idea behind this technique is to perform a weak measurement of the position followed by a strong measurement of the momentum of the particle, in this

case a photon. The weak value then takes the following form:

$$\pi_{\mathrm{w}} = \frac{\langle p|x\rangle\langle x|\Psi_{\mathrm{s}}\rangle}{\langle p|\Psi_{\mathrm{s}}\rangle} = e^{ipx/\hbar}\frac{\Psi_{\mathrm{s}}(x)}{\Phi(p)}. \tag{1.22}$$

As can be seen, the weak value takes a different form to the one obtained in protocols for weak value amplification. Furthermore, if the post-selection is carried out at p=0, the expression above can be simplified to

$$\pi_{\mathrm{w}} = k\Psi_{\mathrm{s}}(x), \tag{1.23}$$

where k is equal to $1/\Phi(0)$ which can be considered to be a normalization constant. This remarkable result shows that this recipe produces a weak value that is directly related to the transverse quantum wavefunction of the measured photons.

The experimental implementation of this method used the relatively simple apparatus depicted in Fig. 1.8. The complete technique comprises three stages. The first part can be understood as a weak measurement in the position variable. This measurement is performed by using a rectangular sliver of a half-wave plate (HWP), labeled it as WP1, to weakly rotate the polarization of light at a specific position. A Fourier transforming lens and a small pinhole allows one to perform the post-selection at $p = 0$ in the momentum basis. The last part is the strong measurement process. Here a HWP or a quarter wave plate (QWP), labeled as WP2, together with a polarizing

beam splitter (PBS) permits the measurement of the real or imaginary part of the WV, respectively.

The interaction Hamiltonian that describes the effect of the weak disturbance in the position variable is $H_{\text{int}} = \alpha\hat{\sigma}_{\text{y}}\hat{\pi}$, where α is a small polarization rotation angle, $\hat{\sigma}_{\text{y}}$ is one of the Pauli matrices defined as $-i\left|H\right\rangle\left\langle V\right| + i\left|V\right\rangle\left\langle H\right|$ and $\hat{\pi}$ is the position operator $\left|x\right\rangle\left\langle x\right|$. After the post-selection at $p = 0$, the final state (which can be described as in Eq. 1.17) takes the following form

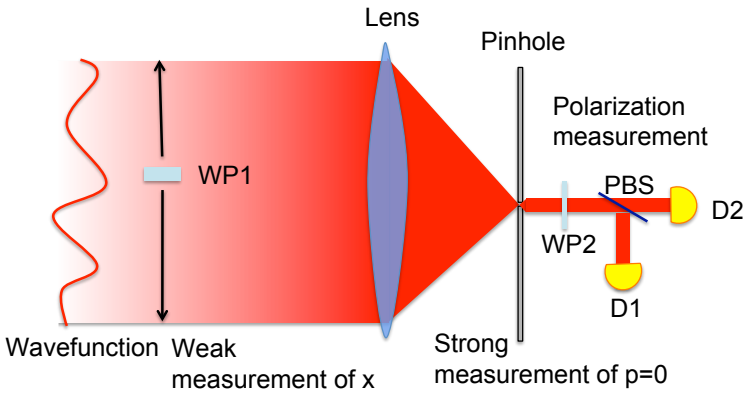

Figure 1.8: Experimental apparatus used by Lundeen and co-workers to measure the spatial wavefunction of a single photon [6]. A weak rotation of polarization, via HWP (WP1) is followed by a strong measurement of the momentum. A series of polarization measurements allow the reconstruction of the spatial quantum wavefunction.

$$\left|s_{\text{f}}\right\rangle = \left|V\right\rangle + \frac{i\alpha}{2}\pi_{\text{w}}\hat{\sigma}_{\text{y}}\left|V\right\rangle . \tag{1.24}$$

It is important to point out that the above state provides information about the wavefunction only at a specific position x. In order to retrieve the full wavefunction, one has to repeat this measurement at various positions x. After the operator $\hat{\sigma}_{\text{y}}$ is

applied to the polarization state, $|s_{\mathrm{f}}\rangle$ takes the form

$$|s_{\mathrm{f}}\rangle = |V\rangle + \frac{\alpha}{2}\pi_{\mathrm{w}}\,|H\rangle\,. \tag{1.25}$$

Since the pointer is the polarization degree of freedom, in order to reconstruct the quantum wavefunction one has to fully characterize the polarization of the detected photons. One way of doing this is by measuring the Pauli operators $\hat{\sigma}_{\mathrm{x}}$ and $\hat{\sigma}_{\mathrm{y}}$ in the final state $|s_{\mathrm{f}}\rangle$. Notably, measurement of $\langle s_{\mathrm{f}}|\,\hat{\sigma}_{\mathrm{x}}\,|s_{\mathrm{f}}\rangle$ provides information about the real part of the weak value

$$\begin{aligned}\langle s_{\mathrm{f}}|\,\hat{\sigma}_{\mathrm{x}}\,|s_{\mathrm{f}}\rangle &= \langle s_{\mathrm{f}}|\,(|H\rangle\langle V| + |V\rangle\langle H|)\,|s_{\mathrm{f}}\rangle \\ &= \alpha\Re[\pi_{\mathrm{w}}].\end{aligned} \tag{1.26}$$

The state above can be measured by using a HWP for WP2 and a PBS. In addition, replacing the HWP with a QWP allows the measurement of the Pauli operator $\hat{\sigma}_{\mathrm{y}}$, which is proportional to the imaginary part of the weak value

$$\begin{aligned}\langle s_{\mathrm{f}}|\,\hat{\sigma}_{\mathrm{y}}\,|s_{\mathrm{f}}\rangle &= \langle s_{\mathrm{f}}|\,(-i\,|H\rangle\langle V| + i\,|V\rangle\langle H|)\,|s_{\mathrm{f}}\rangle \\ &= -\alpha\Im[\pi_{\mathrm{w}}].\end{aligned} \tag{1.27}$$

Therefore the wavefunction can be reconstructed from the measurements of $\langle s_{\mathrm{f}}| \hat{\sigma}_{\mathrm{x}} |s_{\mathrm{f}}\rangle$ and $\langle s_{\mathrm{f}}| \hat{\sigma}_{\mathrm{y}} |s_{\mathrm{f}}\rangle$ as follows

$$\Psi_{\mathrm{s}}(x) = \frac{1}{k\alpha}(\langle s_{\mathrm{f}}| \hat{\sigma}_{\mathrm{x}} |s_{\mathrm{f}}\rangle - i \langle s_{\mathrm{f}}| \hat{\sigma}_{\mathrm{y}} |s_{\mathrm{f}}\rangle). \tag{1.28}$$

This protocol for measuring the wavefuntion can be described in terms of self interference, however, such a description is complicated.

In the following chapter, we describe some experimental interferometric implementations that utilize weak values. We introduce a novel form of weak value amplification in the azimuthal variables of angular position and OAM. We also demonstrate a protocol that utilizes compressive sensing to improve the performance of the direct measurement technique.

1.6 Summary

In this chapter we discussed fundamental concepts that are used in this thesis. We started this chapter by briefly discussing first-order interference and coherence. We then discussed the OAM of light and the standard techniques used for its generation and detection. Fundamental aspects of azimuthal first-order interference and coherence were also provided. We concluded the chapter with a discussion on weak values and how these can be understood as an interference phenomenon. In Chapter 2, we will introduce two interferometric techniques that exploit the potential of weak values for

amplification of angular rotations and measurement of the quantum wavefunction. Chapter 3 is devoted to the study of angular interference in phase space. A novel family of second-order interference effects that correspond to the azimuthal Hanbury Brown and Twiss effect is introduced in Chapter 4. In Chapter 5, we discuss a protocol that utilizes quantum correlations of entangled photons for object tracking. We described the first demonstration and measurement of exotic looped trajectories of light in Chapter 6. The conclusions of this thesis are presented in Chapter 7.

Chapter 2

Interferometric Weak Values

2.1 Introduction

In this chapter we introduce two schemes that utilize interferometric weak values for amplification of small quantities and for quantum state tomography, these weak values are mediated through interference effects. In the first half of this chapter we present a weak measurement protocol that permits a sensitive estimation of angular rotations based on the concept of weak-value amplification. The shift in the state of a pointer, in both angular position and the conjugate orbital angular momentum bases, is used to estimate angular rotations. This is done by an amplification of both the real and imaginary parts of the weak-value of a polarization operator that has been coupled to the pointer, which is a spatial mode, via a spin-orbit coupling. Our experiment demonstrates the first realization of weak-value amplification in the azimuthal degree of freedom. We have achieved effective amplification factors as large as 100, providing

a sensitivity that is on par with more complicated methods that employ quantum states of light or extremely large values of orbital angular momentum.

In the second half of this chapter we introduce a method that exploits sparsity for the compressive measurement of the transverse spatial wave function of photons. The procedure involves weak measurements of random projection operators in the spatial domain followed by postselection in the momentum basis. Using this method, we experimentally measure a 192-dimensional state with a fidelity of 90% using only 25 percent of the total required measurements. Furthermore, we demonstrate the measurement of a 19 200-dimensional state, a task that would require an unfeasibly large acquiring time with the standard direct measurement technique.

2.2 Antecedents of Weak Value Amplification and Measurement of Angular Rotations

As discussed in Chapter 1, in weak measurements, information is gained by weakly probing the system, while approximately preserving its initial state. The uncertainty in each measurement is large due to the weak perturbative nature of the information extraction; however, this is generally overcome by averaging over a large number of identically prepared states. The process of post-selecting the prepared system makes weak measurements interesting. Under certain conditions the outcome, which is called a weak value, is not an eigenvalue of the measurement operator. In fact, WVs can

even exceed the eigenvalue range of a typical strong or projective measurement and in general are complex. These features have allowed a wide range of applicability in classical and quantum contexts. For example, they have resulted in the measurement via amplification of small transverse [30, 34] and longitudinal [31, 32, 43] shifts, the direct measurement of the quantum wave function [6, 35, 36], the development of tomographic techniques [44], the amplification of optical nonlinearities [27], and the clarification of controversial debates in quantum physics [23, 24].

Recently, there has been a strong impetus to employ weak-value amplification as an effective tool in metrology [29, 31, 33, 43]. A WVA protocol involves the preparation of an ensemble of particles with two independent degrees of freedom. These two degrees of freedom are then coupled by means of a weak perturbation and post-selected to collapse one of the them, typically called the probe. Due to the coupling existing between the probe and the other degree of freedom, called the pointer, the post-selection induces a shift in the linear position of the pointer which is proportional to the weakly induced perturbation and the WV. This has allowed the use of WVA to estimate small quantities with sensitivities comparable to quantum-enhanced metrology [29, 31, 33, 43, 45], due to the fact that the use of quantum protocols does not guarantee sensitivities beyond the standard quantum limit, which is the limit for classical protocols [46, 47].

Besides the extensive work on the estimation of longitudinal displacements [31–33, 43, 46–49], high sensitivity measurement of angular displacements has been another

topic of interest. Historically, inquiries regarding relativistic dynamics stimulated interest on the azimuthal degree of freedom [50]. A remarkable example is the Sagnac effect. Atomic versions of the Sagnac interferometer have led to sensitive gyroscopes that permit a precise measurement of rotations [51, 52]. In addition, the use of light endowed with OAM has motivated interest in new forms of rotations. These beams have been used for rotational control of microscopic systems [18], and exploration of effects such as the rotational Doppler shift [53] which has been recently used in techniques for detecting spinning objects [54]. Recent efforts to increase the sensitivity in the measurement of angular rotations involve the generation of large values of OAM [55], quantum entanglement of high OAM values [56], or the use of N00N states in the OAM bases [57]. These protocols require complicated schemes to generate and measure photons in such exotic states. However, the concepts behind them constitute valuable resources not only for optical metrology, remote sensing, biological imaging or navigation systems [54, 58], but also for the understanding of light-matter interactions [59–61].

In this section, we describe WVA in the azimuthal degree of freedom and the processes that give rise to these effects. The first observation of these kinds of WVs suggests interesting physics from the fundamental and applied perspective. For instance, the spin-orbit coupling in our experiment gives rise to an interesting optical effect in which the perturbation of polarization induces a shift in the angular position and OAM spectrum of the pointer. We show that the real and the imaginary part

of the WV for the polarization operator can be accessed by measuring the angular position and its conjugate variable of OAM, respectively. Using this new form of WVs based on spin-orbit coupling, we propose a scheme for the measurement of small rotations. We demonstrate an amplification in the measurement of angular rotations that is as large as 100. The simplicity of our scheme, namely lack of need for exotic quantum state of lights or extremely large values of OAM, makes this technique potentially attractive for applications in optical metrology, remote sensing and optical manipulation of microscopic systems.

2.3 Amplification of Angular Rotations using Weak Measurements

Consider the experimental setup depicted in Fig. 2.1. This scheme comprises three parts: state preparation, a weak perturbation, and post-selection. The state preparation involves the generation of a light beam with diagonal polarization and a well-defined spatial profile. We select the initial polarization state using a polarizer and a HWP; this state will serve as a probe and can be described by the polarization qubit $|\Psi_{pr}\rangle = \frac{1}{\sqrt{2}}(|H\rangle + |V\rangle)$. The preparation of the spatial mode or pointer consists of the generation of an angular mode (ANG) $f(\phi) \propto \exp(-\phi^2/2{\eta_\phi}^2)$, which is a Gaussian-apodized angular slit of width η_ϕ. This is shaped by impressing amplitude and phase information onto the beam by means of modulation of the blaze parameters

on a SLM, used together with a 4f optical system containing a spatial filter in the Fourier plane [62]. The beam is injected into a Sagnac interferometer, where the horizontally and vertically polarized components of the beam circulate in opposite directions. The dove prism (DP) is rotated by a small angle $\Delta\phi/4$ with respect to the plane of the interferometer, which causes the two counter-propagating beams to be rotated by an amount of $\pm\Delta\phi/2$ in opposite directions. This setup enables a coupling between the polarization, marked by the two counter propagating beams, and the transverse azimuthal degree of freedom. In the next step we use two QWPs and a HWP to induce a geometric phase between the two circulating beams in the interferometer, permitting the existence of complex WVs, see Fig. 2.2. Finally, the post-selection is carried out by setting the angle of a polarizer almost orthogonal with respect to the angle of the polarizer used in the pre-selection. At this stage, a full characterization of the complex wavefunction in the transverse angular basis and the conjugate basis of OAM reveals information about the real and the imaginary part of the WV, respectively.

The interaction in our experiment can be described by the spin-orbit interaction Hamiltonian $\hat{H}_{SO} = \mu\hat{\sigma}\hat{\ell}_z$ and a Hamiltonian that describes the action of the wave plates $\hat{H}_g = \delta\hat{\sigma}$, where $\hat{\sigma}$ is the Pauli operator defined by $\hat{\sigma} \equiv |H\rangle\langle H| - |V\rangle\langle V|$, $\frac{\Delta\phi}{2} = \mu\Delta t$, $(\frac{\theta_H}{2} - \frac{\pi}{2}) = \delta\Delta t$ and $\frac{\theta_H}{2}$ is the induced geometric phase. Our state at the input of the interferometer has the following form $|\Psi_i\rangle = |\Psi_{pr}\rangle\,|f(\phi)\rangle$. The interaction

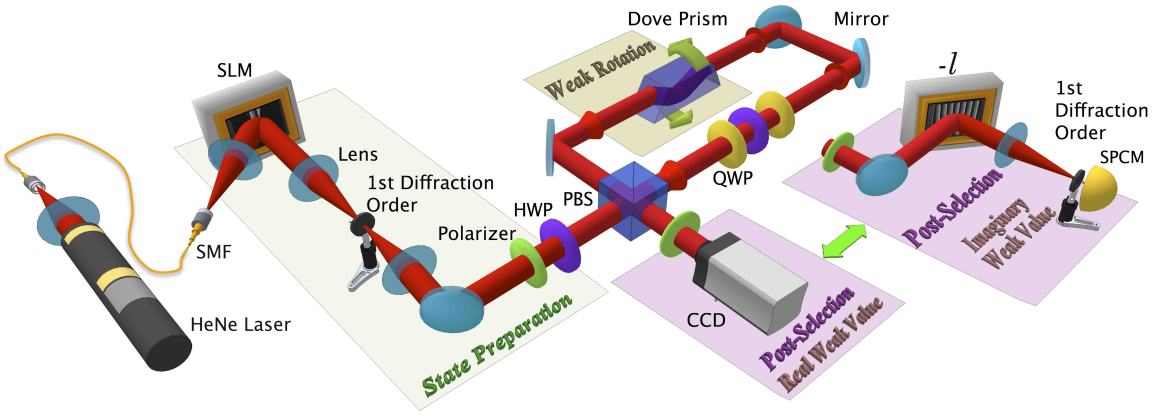

Figure 2.1: Experimental setup. A light beam from HeNe laser working at 632.8 nm is coupled into a SMF and the output is then collimated. The beam is sent to a phase-only SLM and then to a 4f optical system containing a spatial filter in the Fourier plane. A polarization state is prepared by means of a polarizer and a HWP. A Dove prism, a HWP and two QWPs are placed inside the Sagnac interferometer that uses a polarizing beam splitter (PBS). The DP induces a small rotation between the counterpropagating beams; this is the weak perturbation. The QWPs together with the HWP induce a geometric phase between the H and V polarized beams. After postselection, measurements of angular rotations and OAM spectra are performed to access the real or imaginary part of the weak value.

which occurs in the DP couples the two DoFs as follows:

$$\begin{aligned} |\Psi_f\rangle &= e^{-i\frac{\Delta\phi}{2}\hat{\sigma}\hat{\ell}_z} e^{-i\hat{\sigma}(\frac{\theta_H}{2}-\frac{\pi}{2})} |\Psi_i\rangle \\ &= \frac{1}{\sqrt{2}}\left(e^{-i\frac{\theta}{2}}|H\rangle\left|f\left(\phi-\Delta\phi/2\right)\right\rangle + e^{i\frac{\theta}{2}}|V\rangle\left|f\left(\phi+\Delta\phi/2\right)\right\rangle\right), \end{aligned} \tag{2.1}$$

where $\hat{\ell}_z$ acts as the generator of rotations and is proportional to the angular momentum operator projected along the optical axis $\hat{L}_z = \hbar\hat{\ell}_z$, and θ equals $\theta_H - \pi$. As demonstrated by Eq. 2.1, the weak coupling creates entanglement between probe and pointer. It should be noted that since the probe and the pointer are different degrees of freedom of a single beam rather than separate systems or particles, then this is an example of classical entanglement and thus can be described classically [38, 39, 63]. Be-

cause of this, most traditional weak measurement experiments, such as those described in Refs. [6, 31, 34–36, 40, 43, 44], are classically explainable. This also demonstrates what is required to perform a non-classical weak measurement experiment. We have chosen to use the mature language of weak measurement theory, since it provides a simpler description and the results readily apply to a wider range of phenomena including non-classical systems.

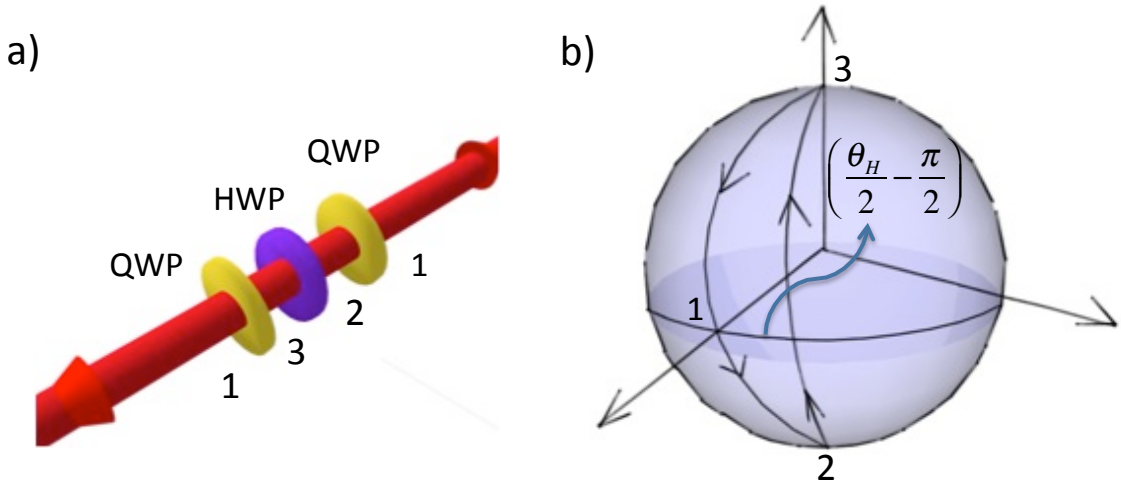

Figure 2.2: Geometric phase. The geometric phase is introduced by means of two QWPs and a HWP, this geometric phase determines the magnitude of imaginary part of the weak value. The first QWP converts horizontal or vertical polarization into circular polarization, this is defined by the trajectory (1)-(2). The HWP allows one to move from the south pole to the north pole in the Poincaré sphere, or vice-versa ((2)-(3)). The last QWP converts circular polarization into linear polarization ((3)-(1)), the closed circuit ((1)-(2)-(3)-(1)) in the Poincaré sphere defines the value of the geometric phase, which is defined by the angle of the HWP.

The post-selection is performed by projecting the perturbed state into $|\Phi_{ps}\rangle = \sin\left(\frac{\gamma}{2}-\frac{\pi}{4}\right)|H\rangle + \cos\left(\frac{\gamma}{2}-\frac{\pi}{4}\right)|V\rangle$, where γ is controlled by the polarizer. The post-selection collapses the polarization state of the probe and causes a shift in the angular

position and the OAM spectrum of the pointer that can be described as

$$|\Psi_p\rangle = |\Phi_{ps}\rangle \left\langle \Phi_{ps} \middle| \Psi_f \right\rangle \approx |\Phi_{ps}\rangle \left| f\left(\phi - \sigma_w \Delta\phi/2\right) \right\rangle. \tag{2.2}$$

Here, σ_w is the complex WV given by

$$\sigma_w \equiv \frac{\left\langle \Phi_{ps} \middle| \hat{\sigma} \middle| \Psi_{fpr} \right\rangle}{\left\langle \Phi_{ps} \middle| \Psi_{fpr} \right\rangle}, \tag{2.3}$$

$|\Psi_{fpr}\rangle$ is defined as $\frac{1}{\sqrt{2}}\left(e^{-i\frac{\theta}{2}}|H\rangle + e^{i\frac{\theta}{2}}|V\rangle\right)$. If the induced phase θ and polarizer selection angle $\gamma/2$ are small, the WV can be approximated as

$$\sigma_w \approx -\frac{2\gamma}{\gamma^2+\theta^2} + i\frac{2\theta}{\gamma^2+\theta^2}. \tag{2.4}$$

The post-selected state described in Eq. 2.2 shows a change in angle as $\phi \to \phi - \sigma_w\Delta\phi/2$. If σ_w is real, which will be the case for $\theta = 0$, then this leads to the rotation of the pointer by the amount σ_w. However if σ_w is complex then

$$\begin{aligned} f(\phi - \sigma_w\Delta\phi/2) &= e^{\left(-(\phi-\sigma_w\Delta\phi/2)^2/2\eta_\phi^2\right)} \\ &\propto e^{\left(-(\phi-\Re(\sigma_w)\Delta\phi/2)^2/2\eta_\phi^2\right)} e^{\left(i\phi\Im(\sigma_w)\Delta\phi/2\eta_\phi^2\right)} \\ &= e^{\left(-(\phi-\Delta\langle\phi\rangle)^2/2\eta_\phi^2\right)} e^{\left(i\phi\Delta\langle\ell\rangle\right)}, \end{aligned} \tag{2.5}$$

where $\Delta\langle\phi\rangle = \Re(\sigma_w)\Delta\phi/2$ sets the amount of the pointer's rotation. In addition, the pointer experiences a shift in its OAM spectrum that equals $\Delta\langle\ell\rangle = \Im(\sigma_w)\Delta\phi/2\eta_\phi^2$.

We have used the angular representation of the spatial mode of the photons, and utilized the Fourier relation between the conjugate pairs of azimuthal angle and angular momentum. Alternatively, the same results can be derived by using the commutation relation between angular position and OAM operators, which is given by $[\hat{\phi}, \hat{L}_z] = i\hbar(1-2\pi P(\phi))$ where $P(\phi)$ represents the angular probability at the boundary of the angle range [20]. The shift in the OAM spectrum can be understood as a form of interaction between SAM and OAM. This interesting optical effect is a consequence of the polarization-sensitive nature of the interactions in the interferometer, and should not be confused with the standard spin-orbit coupling in the vector beams where both the SAM and OAM are directed along the same axis [64].

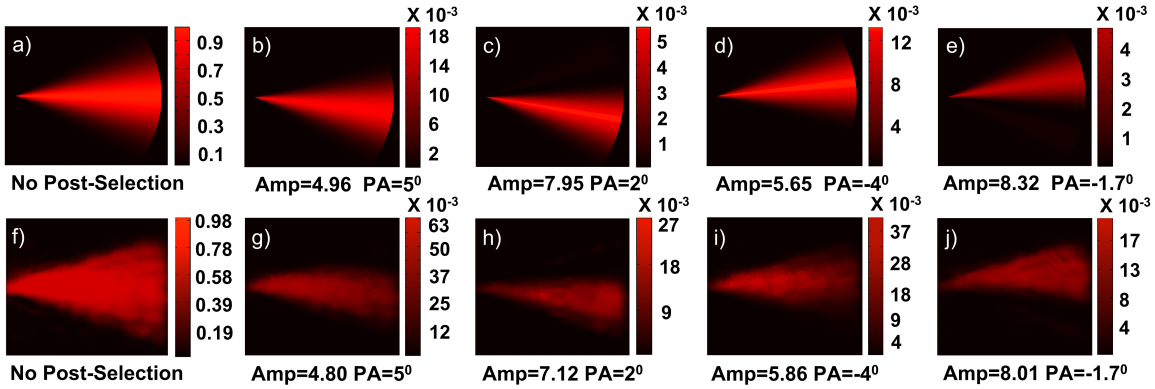

Figure 2.3: Amplification of angular displacements using real weak values. a) – e) show simulations of our scheme for $\Delta\phi = 1.2°$, different post-selection angles (PA) and amplification factors (Amp). f) – j) show experimental evidence of our protocol under the same conditions.

In the experiment we use a 3 mW He-Ne laser (632.8 nm) which is coupled to a single-mode fiber (SMF) and then expanded to a spot size of 1.8 cm. The central part of the beam homogeneously illuminates the display of the SLM that has an active area

of $9.3 \times 7\text{mm}^2$. Due to the reflectance of the SLM and the efficiency of the encoded diffractive grating on it, the power drops to 470 nW once an ANG mode of width $\eta_\phi = 13.7^\circ$ is generated. The DP in the Sagnac interferometer is rotated by 0.3°, this angle is determined by measuring a relative rotation of 1.2° between two identical ANG modes propagating in the opposite directions. The induced displacement $\Delta\phi$, is chosen to be much smaller than the width of the ANG mode, in order to guarantee the conditions for the weak perturbation. The post-selection polarizer is set to an angle $\gamma/2$, with respect to the polarization state of the pre-selected state. For this part, we have set θ to zero.

Since our interest is in the amplification of the weak-value, the angle $\gamma/2$ is set to a small number. The post-selection polarizer forces the two ANG modes to coherently interfere, producing another ANG mode which is rotated due to the azimuthal Gaussian intensity distribution impressed in the ANG [25]. Such rotation is proportional to the angular displacement $\Delta\phi$ and the real part of the WV $\Re(\sigma_w)$. Since the WV can take values larger than one, this scheme allows the amplification of small rotations. However, as $\Re(\sigma_w)$ is increased more photons are lost as shown for different post-selection angles (PA) in Fig. 2.3 (a)–(e). In order to detect this effect, a CCD camera is placed after the polarizer. This is equivalent to measuring the expected value of the angular position in the state $|\Psi_p\rangle$. As shown in Fig. 2.3(f)–(j), the measured power is in the range of 10–30 nW, however these images were taken using long exposure times. As can be seen in Fig. 2.3, an aggressive post-selection leads to a larger rotation. The

amplification factor (Amp) is defined as the ratio between the angular position of the post-selected mode $\Delta\langle\phi\rangle$ and $\Delta\phi$. This is equal to $\Re(\sigma_w)/2$. Both $\Delta\langle\phi\rangle$ and $\Delta\phi$ were determined by using centroid measurements. The amplification limit is given by the extinction ratio of the polarizer and the magnitude of the weak perturbation or the angle of post-selection. Larger amplifications can be measured if the width of ANG is increased and the post-selection angle is decreased.

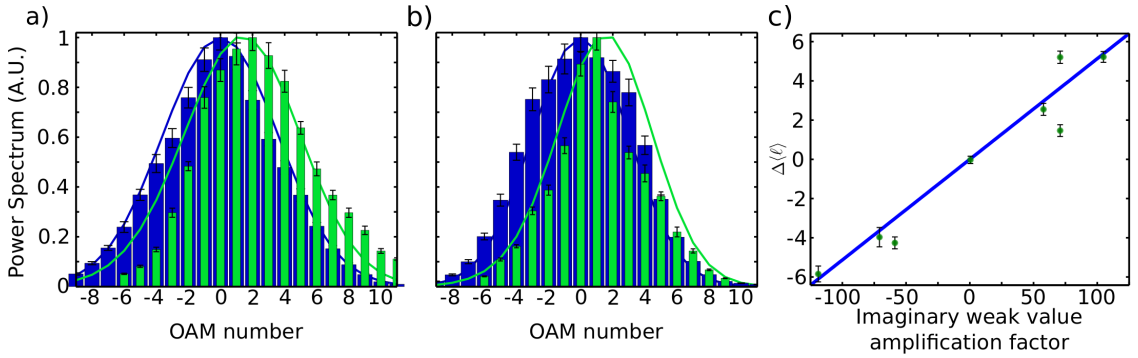

Figure 2.4: Measured OAM power spectra of $|\Psi_p\rangle$ without post-selection (blue) and with post-selection (green) demonstrating the shift in $\langle\ell\rangle$ due to $\Im(\sigma_w)$ for a) $\eta_\phi = 11.4^0$, $\gamma/2 = 6^0$ and b) $\eta_\phi = 13.7^0$ and $\gamma/2 = 5^0$. The angle $\theta/2$ equals 5^0 for all the cases. Histograms represent measured data, while lines represent theoretically predicted shifts. c) OAM centroid shift $\Delta\langle\ell\rangle$ for various measured OAM power spectra plotted against the imaginary WV amplification factor, $\Im(\sigma_w)/2\eta_\phi^2$. Dots represent data, while the line is the theoretical linear curve predicted by Eq. 2.5.

The imaginary part of the WV can be determined by analyzing the shift of the OAM spectrum of the ANG. We have chosen the rotation angle of the DP to be approximately 0.4° and we have tried different angular widths for the input state. In order to allow $\Im(\sigma_w)$ to be nonzero, the phase θ must also be nonzero. This is done by inducing a geometric phase between the polarization states $|H\rangle$ and $|V\rangle$. This phase is created using three rotatable wave plates as shown in Fig. 2.1 and 2.2. The angle

of the QWPs is set to $\pi/4$ and the HWP is rotated by a small angle, see Appendix A. We have set the HWP to an angle such that $\theta/2 = 5^\circ$ and tried several different post-selection angles for the polarizer. As discussed in Chapter 1, measurement of the OAM spectrum associated with a beam can be done using a wide variety of techniques [65–68]. We measured the OAM using a series of projective measurements for various values of ℓ. Using a similar procedure as was used for generating the angular slits, a hologram was impressed onto a SLM and then a Fourier transforming lens and a spatial filtering from a SMF couples photons to an APD which allows measurement at single photon levels, see Appendix A. We summed the counts during a 0.2 second window and averaged it for 30 measurements for each projection over different OAM modes. This procedure was repeated for each mode and the reconstructed spectra are shown in Fig. 2.4 (a)–(b). The error bars represent the standard deviation over the ensemble of 30 measurements. The spectrum is broader for angular modes with narrower widths due to uncertainty relation between angular position and OAM [20]. As predicted by Eq. 2.5, and shown in Fig. 2.4, the larger amplifications are obtained for angular modes with narrow widths. However, such narrow ANG modes have physically smaller cross sections and hence carry proportionally less power. Each OAM power spectra was fitted using a weighted least-squares minimization to a shifted Gaussian function. The mean values are plotting in Fig. 2.4 (c) along with error bars representing the 3σ confidence interval. By exploiting the measurement process we

have amplified small rotations by a magnitude of 100 without using high OAM nor entanglement.

We have made the first step towards the study of WVA in the azimuthal degree of freedom. This has been approached by describing the mechanisms that lead to a shift in the angular position and OAM of an optical beam. The OAM spectrum is shifted as a consequence of the breakup in the polarization symmetry, realized by a differential geometric phase. Furthermore, we have implemented the first realization of WVA in the angular position and OAM bases. The results presented here provide a proof-of-principle demonstration of the scope of WVA in this degree of freedom. We believe that our protocol opens the possibility for new schemes in optical metrology. In addition, our approach shows an alternative fashion to study the exchange between SAM and OAM in optical systems.

2.4 Compressive direct measurement of the transverse wavefunction

We now describe an experiment related to the direct measurement of the wave function. We start this section by introducing a technique called compressive direct measurement (CDM) [2]. This scheme combines the benefits of direct measurement with a computational technique known as compressive sensing (CS) [69, 70]. CS uses a nonlinear algorithm to recover a sparse n-dimensional signal from a series of m

projective measurements. Unlike the case of linear reconstruction, the number of measurements m in a compressive scheme can be much smaller than the dimension n of the signal. CS provides an efficient alternative to raster scanning in the application where arrayed-detectors are either costly or not available such as quantum optics and low-light-level measurements. Specific examples include single-photon level imaging, entanglement characterization, and quantum ghost imaging [5, 71–73].

We use the polarization of the photon as the pointer. The initial system-pointer state can be written as

$$|\Omega\rangle = |\psi\rangle |V\rangle = \sum_{i=1}^{N} \psi_i |x_i\rangle |V\rangle , \tag{2.6}$$

where $|V\rangle$ indicates that the initial polarization is vertical and where $|\psi\rangle$ is the initial spatial wavefunction. We next perform a series of random weak measurements in order to retrieve the spatial wave function $|\psi\rangle$. Each measurement is described by the projection operator $\hat{Q}_{\mathrm{m}}$, that can be expanded as a weighted sum of position projection operators $\hat{\pi}_j$ at all the points

$$\hat{Q}_{\mathrm{m}} = \sum_{\mathrm{j}} Q_{\mathrm{m,j}} \hat{\pi}_{\mathrm{j}}. \tag{2.7}$$

For the purpose of simplifying the experiment we consider the special case where $Q_{\mathrm{m,j}}$ a real coefficient that can be either 1 or 0. The state of the particle after the

measurement can be approximately described as

$$e^{i\alpha}\left|\Omega\right\rangle \approx \left|\Omega\right\rangle + \alpha\sum_{i=1}^{N} Q_{\mathrm{m,j}}\psi_i \left|x_i\right\rangle \left|H\right\rangle . \tag{2.8}$$

Following the weak measurement, we perform a projection onto the zeroth order momentum state. This will erase the spatial structure of the photons and we are left with a beam with the polarization state

$$\left|s_m\right\rangle = \left|V\right\rangle + \frac{\alpha}{\phi_0\ \sqrt{N}}\sum_j Q_{m,j}\psi_j \left|H\right\rangle . \tag{2.9}$$

At this stage the information about the state-vector ψ_j is encoded in the expected values of the polarization of the post-selected state

$$\begin{aligned} \bar{\sigma}_{\mathrm{x,m}} &= \left\langle s_{\mathrm{m}}\right| \hat{\sigma}_x \left|s_{\mathrm{m}}\right\rangle = k\sum_{\mathrm{j}} Q_{\mathrm{m,j}}\Re[\phi_{\mathrm{j}}], \\ \bar{\sigma}_{\mathrm{y,m}} &= \left\langle s_{\mathrm{m}}\right| \hat{\sigma}_y \left|s_{\mathrm{m}}\right\rangle = -k\sum_{\mathrm{j}} Q_{\mathrm{m.j}}\Im[\phi_{\mathrm{j}}]. \end{aligned} \tag{2.10}$$

where $\hat{\sigma}_x = \left|H\right\rangle\left\langle V\right| + \left|V\right\rangle\left\langle H\right|$, $\hat{\sigma}_y = -i\left|H\right\rangle\left\langle V\right| + i\left|V\right\rangle\left\langle H\right|$ and $\kappa = \frac{2\alpha}{\phi_0\sqrt{N}}$. After repeating the measurement M times, one obtains a linear relation between the measurement results and the unknown wavefunction

$$\begin{pmatrix} \phi_1 \\ \phi_2 \\ \vdots \\ \phi_M \end{pmatrix} = \begin{pmatrix} Q_{1,1} & Q_{1,2} & \cdots & Q_{1,N} \\ Q_{2,1} & Q_{2,2} & \cdots & Q_{2,N} \\ \vdots & \vdots & \ddots & \vdots \\ Q_{M,1} & Q_{M,2} & \cdots & Q_{M,N} \end{pmatrix} \begin{pmatrix} \psi_1 \\ \psi_2 \\ \vdots \\ \psi_N \end{pmatrix}. \tag{2.11}$$

Here, $\phi_m = \frac{1}{\kappa}[\bar{\sigma}_{x,m} - i\bar{\sigma}_{y,m}]$, and $m \in \{1 : M\}$ and $n \in \{1 : N\}$, where M is the number of times the measurement is repeated with different random projections. For the case where $M = N$, the solutions of the system above can be exactly solved for a non-singular matrix $\hat{Q}$. However, for the case when $M \leq N$ there exists multiple (and typically many, for small Ms) solutions to the system of equation.

Compressive sensing provides a method for finding the solution by using the prior knowledge of sparsity of the unknown function in a known basis. This is often achieved by solving an optimization problem that can be formulated in multiple forms. In our experiment, we assume sparsity in the gradient basis, which leads to the following optimization problem

$$\min_{\psi'} \sum_j ||\nabla\psi'_j||_{l_1} + \frac{\mu}{2}||\hat{Q}\psi' - \phi||^2_{l_2}. \tag{2.12}$$

Here, $\nabla\psi'$ is the discrete gradient of ψ' at position x_j, and μ is a weighting factor that penalizes deviations from experimental data. Heuristically, the solution of the optimization problem allows the determination of the *smoothest* state ψ', that is *approximately* in agreement with the experimental data.

Fig. 2.5 shows the schematic of the experiment. A vertically polarized Gaussian beam illuminates a SLM, which together with two QWPs (WP1 and WP2) performs the polarization rotation. The amount of rotation can be controlled at each pixel

by setting the grayscale values on the SLM. After the Fourier transforming lens, the post-selection in the momentum basis is performed by using a pinhole that projects on a single spatial mode. As derived in Chapter 1, the real part of the WV is retrieved by using a HWP (shown as as WP3 on Fig. 2.5) and a PBS. Similarly, the imaginary part of the WV is measured by using a QWP before the PBS. The flux of photons at the two output ports of the PBS are detected with APDs.

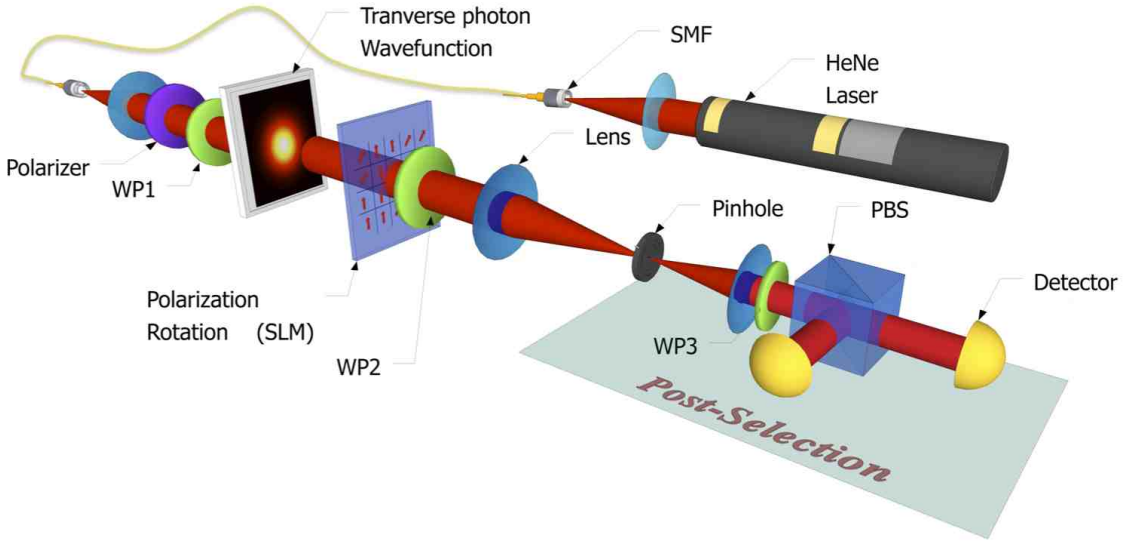

Figure 2.5: A collimated vertically polarized Gaussian beam illuminates a SLM, which is used along with two QWPs (WP1and WP2) to rotate the polarization at each pixel. A lens focuses the beam onto a pinhole with a diameter of 10 μm. The polarization measurement is performed on the light collected from the pinhole using a QWP/HWP (WP3) and a PBS.

For each measurement m, a pre-generated random binary matrix $\hat{Q}_m$ is displayed on the SLM. The photon fluxes measured at the APDs are used to find the expectation values of the Pauli matrices for each measurement and subsequently ϕ_m. The wavefunction is then retrieved via post processing on a computer. We use the algorithm

known as Total Variation Minimization by Augmented Lagrangian and Alternating Direction [74] (TVAL3) to solve Eq. 2.12.

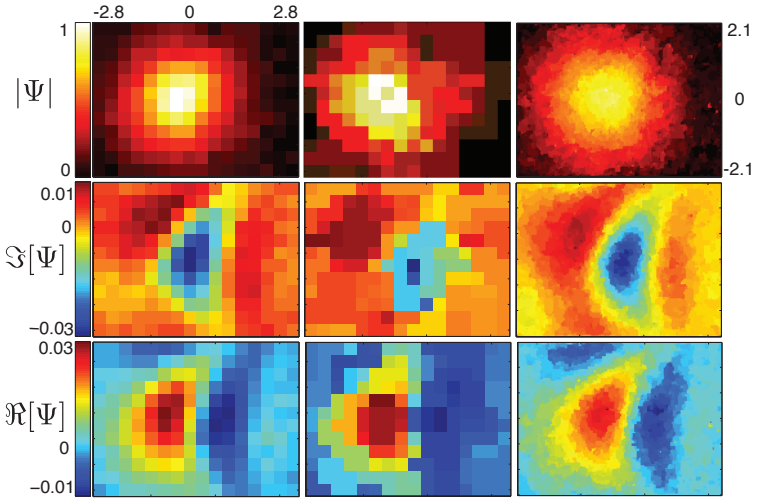

Figure 2.6: The amplitude, real, and imaginary parts of an aberrated Gaussian state measured experimentally. The left column shows data from a pixel-by-pixel scan of the state for $N = 192$. The middle column presents the reconstructed wavefront for $N = 192$, and $M/N = 20\%$ of total measurements from the CDM method. The right column demonstrates reconstruction of a higher dimensional state for $N = 19200$, and $M/N = 20\%$ of total measurements. The transverse dimensions of the state are shown in millimeters.

We perform the experiment on an aberrated Gaussian beam. This corresponds to a complex wavefunction with non-trivial real and imaginary parts. First, the wavefunction is reconstructed via standard direct measurement. The real and imaginary parts from a pixel-by-pixel raster scan are shown on the left column of Fig. 2.6 for an $N = 12$ x $16 = 192$ dimensional Hilbert space. On the middle column, we have shown the real and imaginary parts of the wavefunction reconstructed from CDM using $N = 192$ and M/N x $100 = 20\%$. It is evident that a reconstruction with 20% of measurements can find all the main features of the wavefunction. Nevertheless, a high

quality reconstruction requires a more sparse signal. To achieve this, we use a smaller pixel size. This results in a wavefunction with a larger dimension size. Moreover, the increased sampling results in a more sparse representation in the gradient basis. On the right column of Fig. 2.6 the reconstructions for $N = 120$ x $160 = 19200$ and M/N x $100 = 20\%$ are shown. It can be seen that an experiment with 20% of measurements provides an accurate reconstruction.

We use fidelity as a metric for quantifying our results. For a pair of pure states, fidelity is defined as

$$F(|\psi'\rangle, |\psi\rangle) = |\langle\psi'|\psi\rangle|. \tag{2.13}$$

Here, the retrieved state $|\psi'\rangle$, via CDM, is compared with the target state $|\psi\rangle$ that is retrieved from standard direct measurement. The results are shown in Fig. 2.7. The horizontal axis represents the percentage of measurements. The blue line shows the fidelity of the retrieved state with the CDM method. The red curve represents the average fidelity of the reconstructed state using the data from a partial pixel-by-pixel measurement. It is remarkable that the compressive method results in a drastic increase of fidelity for the first few measurements and gradually settles to a value close to 1. For example, a fidelity as high as 90% is achieved by performing 25% of measurements, while the standard direct measurement (this is, a raster scan) requires of approximately 80% of all the measurements to achieve the same fidelity.

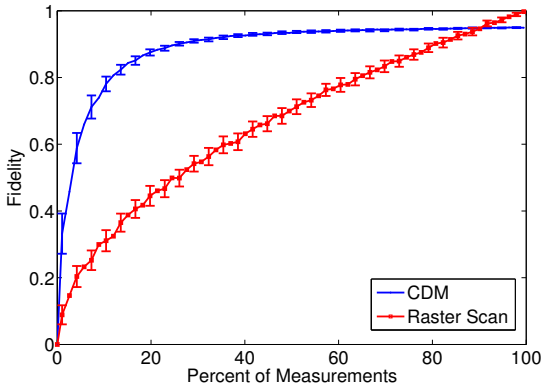

Figure 2.7: The fidelity of the reconstructed state with the target wavefunction as a function of the percentage of total measurements for a 192 dimensional state. The fidelity of the state reconstructed with CDM is shown in blue. The fidelity of the retrieved state from a partial pixel-by-pixel scan with the same number of measurements is shown in red. The error-bars represent standard deviation calculated from 100 repetitions of the experiment.

The measurement of the quantum wavefunction has been one of the great experimental challenges in quantum physics. Over the past 20 years, many seminal contributions have been made to this field [75, 76]. Despite this achievements, the reconstruction of high-dimensional states remains challenging. The direct measurement approach, introduced by Lundeen *et.al*, which can be explained in terms of self interference, has provided a straight-froward experimental techniques that can be easily adopted for measuring multi-level states. We have introduced the compressive direct measurement as an efficient and fast technique for the direct measurement of quantum wavefunctions with very large dimensions. In addition to quantum optics, our technique can be used for application in classical regimes were an array of detectors is not available, such as the imaging and wavefront sensing with Terahertz waves.

2.5 Summary

In this chapter we discussed two interference effects that led to remarkable forms of weak values. In the first part of the chapter, we discussed how a spin-orbit interaction in a polarization sensitive Sagnac interferometer induced a shift in the angular position and orbital angular momentum of an optical beam when post-selection is performed. We found that the real part of the weak value is responsible for the shift in angular position whereas the imaginary part induces a shift in the OAM spectrum of the beam.

In the second part of the chapter, we used direct measurement and compressive sensing to reconstruct the quantum wavefunction with only a small fraction of the total numbers of measurements required in direct measurement. We used fidelity to characterize the performance of our technique. We demonstrated that a fidelity of 90 % can be obtained by using only 25 % of the required measurements. Along this chapter we point out that both techniques rely on interference effects, the first exploits angular coherence whereas the second is based on self interference.

Chapter 3

Angular Interference in Phase Space

3.1 Introduction

In this chapter we introduce the Wigner distribution in the azimuthal space described by the angular position and orbital angular momentum variables. The Wigner distribution in the angular domain provides valuable insight into understanding the wave behavior of the light field in the conjugate bases of OAM and azimuthal angle. In addition, we discuss how our technique allows one to determine the azimuthal first-order degree of coherence of a partially coherent beam [3]. In the context of quantum optics, this novel technique allows the reconstruction of density matrices for pure and mixed high-dimensional OAM states. We hope that this method for characterization of the azimuthal Wigner distribution will constitute an essential part of quantum information protocols that employ the azimuthal structure of single photons [77–79] .

3.2 Wigner distribution and its application in OAM science

Ever since its introduction in 1932, the Wigner distribution has been widely applied in different fields of science [80]. For example in statistical mechanics, optics, quantum physics, electrical engineering and even seismology [81, 82]. In optical physics, the Wigner distribution has been utilized to bring the machinery of phase-space statistical mechanics into the study of optical coherence [83]. The Wigner distribution provides a comprehensive characterization of the system and, as a quasiprobability distribution, the negativity of the Wigner distribution signals a wavelike behavior.

A wide variety of interferometric techniques have been employed to measure the Wigner distribution in different contexts. For example, the Wigner distribution for transverse spatial modes of light has been measured using displaced Sagnac interferometers [83]. In addition, the Wigner distribution in the time-frequency quadratures for optical pulses has been measured by means of auto-correlators [84]. In the context of quantum optics, different forms of homodyne measurements have been employed to determine the quadratures of the field for different excitation modes [85]. Remarkably, this powerful representation has not been utilized to experimentally measure properties of light in the azimuthal domain. This despite the remarkable challenges involved in the measurement of OAM.

Quantum mechanically, a pure state in the Hilbert space of OAM is described by a discrete state vector. Thus, the probability distribution provided by projective measurements along with the knowledge of relative phase between the different OAM components found by interferometry adequately describes a pure state [35]. Nevertheless, pure states are only a restricted set of physical states, because the vast majority of conceivable states are mixed states [86]. The most general description of a quantum state requires knowledge of its density matrix, which can be found through use of standard quantum state tomography [85]. However, quantum state tomography in the OAM basis requires the capability to perform projective measurements on arbitrary superpositions of two or more OAM eigenstates [87], a task that remains challenging due to technical limitations such as variations in the efficiency of measuring different OAM modes and the cross talk between neighboring modes [88].

3.3 Wigner distribution in the angular quadratures

In this section we would like to introduce the Wigner distribution for the angular quadratures and how we determined the density matrix in the basis of angular position by using polarization as a pointer.

We begin our analysis by considering a quantum system with an unknown density matrix, $\hat{\rho}$, in the basis of azimuthal angle, θ. We choose to work in a finite-dimensional state space spanned by the orbital-angular-momentum eigenvector $|\ell\rangle$ with $\{|\ell| \leq N\}$.

In this subspace, the discrete Wigner distribution reads [89]

$$W(\theta,\ell)=\frac{1}{d}\sum_{\phi=-N}^{N}\exp\Big(-\frac{4\pi i}{d}\ell\phi\Big)\left\langle\theta-\phi\right|\hat{\rho}\left|\theta+\phi\right\rangle. \tag{3.1}$$

The dimensionality of the state d is defined as $2N+1$, and $\theta\in\{N,...,N\}$ denotes the discrete angular coordinate. We have defined an angular eigenstate (ANG) through the Fourier transform of the OAM states

$$\left|\theta\right\rangle=\frac{1}{\sqrt{d}}\sum_{\ell=-N}^{\ell=+N}\exp\Big(-\frac{2\pi i}{d}\ell\theta\Big)\left|\ell\right\rangle. \tag{3.2}$$

The ANG states were utilized in the previous chapter for angular amplification and have been widely used in the context of quantum key distribution and for violation of Bell inequalities with angular variables [1, 78, 90]. Now we introduce the theoretical idea behind our scheme for measuring the Wigner distribution. To some extend, this technique shares some similarities to the idea introduced in Chapter 2 for amplification of angular rotations. In this case, we prepare an arbitrary OAM state in diagonal polarization $\left|+\right\rangle=(\left|H\right\rangle+\left|V\right\rangle)/\sqrt{2}$, where $\left|H\right\rangle$ and $\left|V\right\rangle$ represent horizontal and vertical polarization, respectively. The density matrix associated with the two degrees of freedom of the beam is given by $\hat{\Omega}=\hat{\rho}\left|+\right\rangle\left\langle+\right|$. In the next step, we consider the

unitary evolution of the joint system-pointer state characterized by the operator

$$\hat{U}(\tau) = \exp\Big(-\frac{2\pi i}{d}\tau\hat{L}\hat{\sigma}_z\Big). \tag{3.3}$$

Here, $\hat{L}$ is the orbital angular momentum operator directed along the optical axis and $\sigma_z = |H\rangle\langle H| - |V\rangle\langle V|$. As in the experiment for angular amplification [1], the operator $\hat{U}$ describes a polarization sensitive rotation by the angle τ. After this transformation, the system-pointer state is found as $\hat{\Lambda}(\tau) = \hat{U}(\tau)\hat{\Omega}\hat{U}(\tau)$

The interaction described by the operator $\hat{U}$ results in an entangled system pointer state. Post-selection on a specific angular state θ leads to a reduced density matrix of the pointer

$$\hat{\sigma} = \frac{\langle\theta|\,\hat{\Lambda}\,|\theta\rangle}{\mathrm{Tr}[\langle\theta|\,\hat{\Lambda}\,|\theta\rangle]}. \tag{3.4}$$

Interestingly, the expectation value of the Pauli operators $\hat{\sigma}_x$ and $\hat{\sigma}_y$ in the post-selected state is directly proportional to the density matrix $\hat{\rho}$. This calculation can be performed by using the shift property of the angular eigenstates, $\exp[-i(2\pi i/d)\tau\hat{L}]\,|\theta\rangle = |\theta+\tau\rangle$. Here, we have $\theta_\pm = \theta \pm \tau$. Using this notation we find that

$$\begin{aligned}\langle\hat{\sigma}_x(\theta,\tau)\rangle &= \mathrm{Tr}[\hat{\sigma}_x\hat{\sigma}] = \frac{2}{N(\theta,\tau)}\Re[\langle\theta_+|\,\hat{\rho}\,|\theta_-\rangle],\\ \langle\hat{\sigma}_y(\theta,\tau)\rangle &= \mathrm{Tr}[\hat{\sigma}_y\hat{\sigma}] = \frac{2}{N(\theta,\tau)}\Im[\langle\theta_+|\,\hat{\rho}\,|\theta_-\rangle].\end{aligned} \tag{3.5}$$

The normalization factor $N(\theta, \tau)$ is given by $\mathrm{Tr}[\langle\theta|\,\hat{\Lambda}\,|\theta\rangle]$. The pair of equation in Eq. 3.5 can be inverted readily to find $\langle\theta_+|\,\hat{\rho}\,|\theta_-\rangle$. Thus, one can find the elements of the density matrix in the ANG basis by performing rotation of value τ, followed by a post-selection on $|\theta\rangle$. In this procedure, we separately find the real and imaginary parts of the density matrix by measuring the expectation values of the two conjugate variables of the pointer, $\hat{\sigma}_x$ and $\hat{\sigma}_y$. This approach provides the density matrix in the angular basis of $|\theta\rangle$. Having found the density matrix in the angular basis, we use Eq. 3.1 to find the azimuthal Wigner distribution.

3.4 Experimental determination of the azimuthal Wigner distribution

The technique described above can be experimentally implemented by means of a Sagnac interferometer. The experimental setup is shown in Fig. 3.1, similar to the interferometer used in Chapter 2, we use the light beam from a 3 mW He-Ne laser (633 nm), that is coupled to a single-mode fiber and the expanded to uniformly illuminate a SLM. The SLM is used to realize computer generated holograms for creating arbitrary spatial modes. We use a Dove prism inside a Sagnac interferometer for realizing the rotational transformation $\hat{U}$. The polarization state of the beam injected to the input port of the interferometer is diagonal. We use QWPs and HWPs along with a PBS for performing the measurement of $\langle\hat{\sigma}_x\rangle$ and $\langle\hat{\sigma}_y\rangle$.

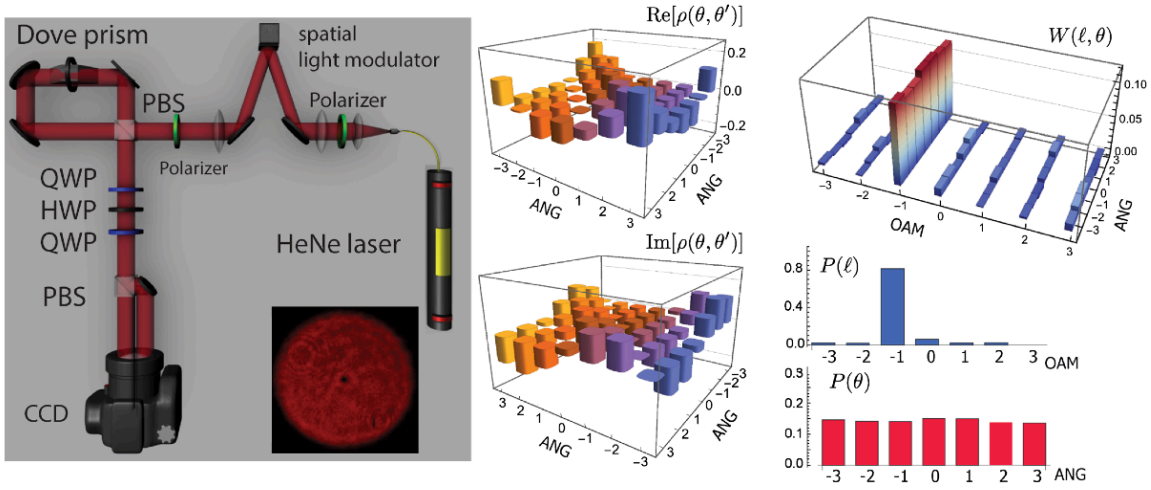

Figure 3.1: Left: Diagram for the experimental setup utilized for measuring the Wigner distribution of a structured laser beam. Middle and right: Experimental results for characterization of an OAM mode with $\ell = -1$. The plots in the middle column show the real and imaginary part of the of the density matrix in the ANG basis, and the plots in the right column present the azimuthal Wigner distribution along with the corresponding marginal distributions in the ANG and OAM bases.

The post-selection process consists on the measurement of the interference patterns at specific angular positions defined by an angular wedge with sharp boundaries. This task is performed in post-processing by analyzing an image of the beam at the two output ports of the PBS. Once we record the intensity in the form of an image, it can be binned to a sequence of numbers that correspond to post-selection on multiple angular states.

Experimental results for the characterization of an OAM mode with $|\ell = -1\rangle$ is shown in Fig. 3.1. It is evident that most part of the photon population is in $|\ell = -1\rangle$ for this state, and consequently it has approximately equal components of ANG states. The fidelity of the state, which is estimated in 90%, testifies the high quality of the generation and characterization of the procedure. We use the standard method of

maximum-likelihood estimation to find positive-definite density matrices in the ANG basis from the experimental data.

We also test our technique with more complicated OAM states, we generate and characterize a pure and a mixed superposition of the OAM states $|\ell = 1\rangle$ and $|\ell - 1\rangle$. A pure and equal superposition state is generated directly through the use of a computer generated hologram. To create a mixed state, we use a computer to randomly switch the SLM between two holograms designed for generating $\ell = 1$ and $\ell = -1$ modes [16]. The mode switching occurs at a rate of 60 Hz, and we use long (10 s) exposure time on the CCD to guarantee uniform averaging over the changing beam structure. The results in Fig. 3.2 (a) show the intensity pattern and the measured Wigner distributions for the coherent and incoherent superpositions of the two states. As one would expect, the marginal distributions in the OAM bases are nearly identical, demonstrating the two contributions from $|\ell = 1\rangle$ and $|\ell = -1\rangle$ in both cases. Interestingly, our technique unveils the coherence properties of the state. For example, we observe an interference pattern in the ANG marginal, and negative values on the $|\ell = 0\rangle$ portion of the Wigner distribution. For the incoherent mixture, we see no interference in the ANG marginals, and the $|\ell = 0\rangle$ portion of the Wigner distribution remains positive. This is a manifestation of a well known property of the Wigner distribution. Namely, wave interference gives rise to negative values on the Wigner distribution, whereas such a pattern is absent for an incoherent mixture.

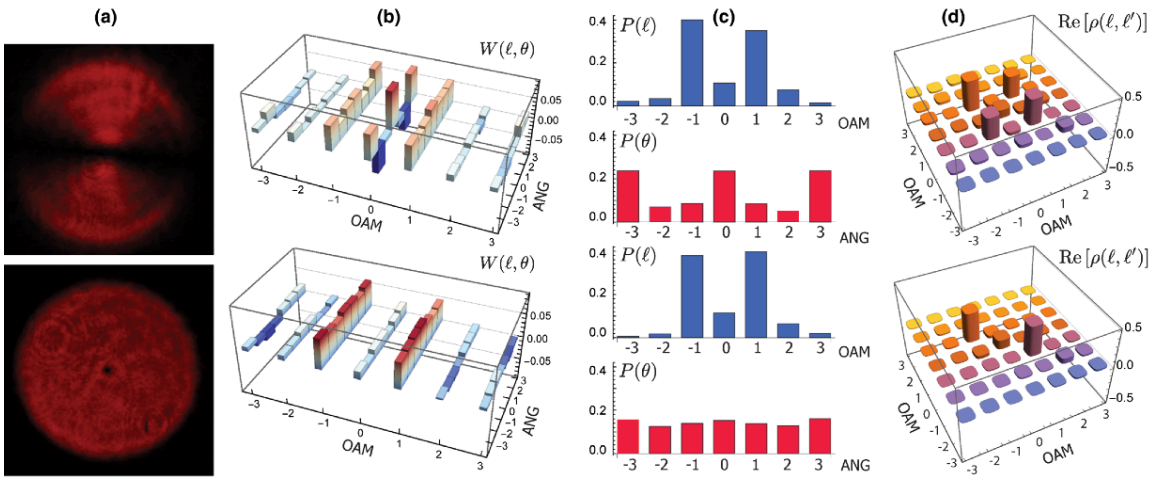

Figure 3.2: (a) The intensity pattern of a pure superposition (top) and (bottom) an incoherent mixture of $\ell = 1$ and $\ell = -1$ OAM modes with equal weights. (b) The azimuthal Wigner distribution from the experiment. (c) The marginal distributions in the OAM and ANG bases. (d) The real part of the OAM density matrices.

We have mapped the Wigner distribution onto the OAM density matrix for the states presented in Fig. 3.2. The degree of coherence between the OAM components $|\ell = 1\rangle$ and $|\ell = -1\rangle$ can now be quantified by the magnitude of the off-diagonal elements of the density matrix. The degree of coherence is calculated by using the relation

$$\gamma = \frac{|\rho(-1,1)|}{\sqrt{|\rho(1,1)||\rho(-1,-1)|}} \tag{3.6}$$

We find the degree of first-order coherence for the two states under consideration as $\gamma_{pure} = 0.80$ and $\gamma_{mixed} = 0.06$. For the pure superposition state, the apparent low coherence is attributed to the imperfections in the generation of the state and the averaging over the nonuniform radial structure of the laser beam.

We demonstrate the photon efficiency of our method by characterizing the transverse structure of heralded single photons using the setup depicted in Fig. 3.3. The pairs of photons are generated by pumping a periodically poled potassium titanyl phosphate crystal (PPKTP) with the beam from 405 nm laser diode. In our case, he type-0 parametric down conversion converts a photon of the pump beam to a pair of signal and idler photons at the wavelength of 790 and 830 nm, respectively. We separate the two photons of each pair with a dichroic mirror. The idler photons are collected with a lens and detected using an APD. The signal photons are sent through a q plate that is sandwiched between two crossed polarizers. The q plate we used has a charge of 1/2 to shape the transverse structure of the photon to a superposition of $|\ell = 1\rangle$ and $|\ell = -1\rangle$ states. The structured photons are injected t the Sagnac interferometer described above. In our experiment we utilized an Andor iStar intensified charge coupled device (ICCD) camera for detecting the heralded single photons. Each detection event is triggered by the electronic signal from the APD in a 5 ns time window. Fig. 3.3 displays the structure of the shaped signal beam from a 1200 sec exposure. We combine our measurement results for the different rotation angles to find the Wigner distribution and subsequently map it to the OAM density matrix. The Wigner distribution exhibits regions of substantial negative value for $\ell = 0$ portion, which demonstrated quantum interference between $\ell = 1$ and $\ell = -1$ components of the state.

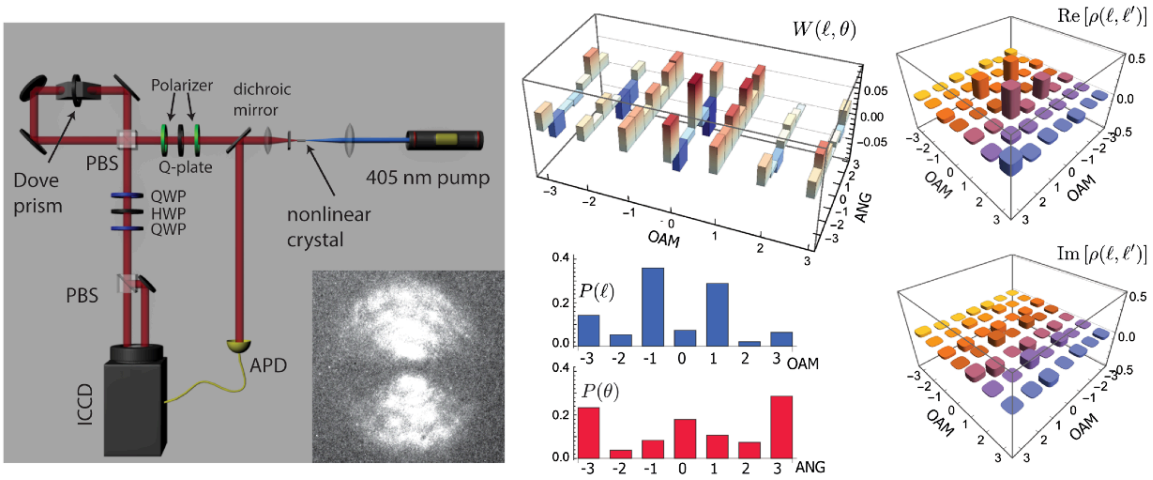

Figure 3.3: Left: Single photons from nondegenerate parametric down-conversion are separated by a dichroic mirror. The idler photons (830 nm) are detected by an APD, which heralds the detection of signal photons (790 nm) with an ICCD. A q plate ($q = 1/2$) is placed between two crossed polarizers to prepare an equal superposition of $\ell = 1$ and $\ell = -1$ OAM modes. Inset: The transverse structure of single photons captured with an accumulation of 5-ns coincidence events over 1200 sec exposure time. Right: The Wigner distribution, the OAM and ANG marginals, and the real and imaginary parts of the OAM density matrix from experiment.

3.5 Summary

In this chapter we described a technique that used to demonstrate the full characterization of the azimuthal structure of a photon wave function. For the first time, we measured the Wigner distribution in the azimuthal degree of freedom by performing projections in the angular basis. We have tested our technique by applying it to the characterization of both classical laser beams and heralded single photons. However the formalism presented here can be applied to the tomography of any finite-dimensional quantum system. Our approach readily scales to very large dimensions, involves no photon loss from post-selection, and is capable of characterizing partially coherent

OAM states. We anticipate that the presented method for characterization of the azimuthal Wigner distribution will constitute an essential part of quantum information protocols that employ the azimuthal structure of single photons.

Chapter 4

HBT Interferometry with Twisted Light

4.1 Introduction

The rich physics exhibited by random optical wave fields permitted Hanbury Brown and Twiss to unveil fundamental aspects of light. Furthermore, it has been recognized that optical vortices are ubiquitous in random light and that the phase distribution around these optical singularities imprints a spectrum of orbital angular momentum onto a light field. In this chapter, we demonstrate that random fluctuations of intensity give rise to the formation of correlations in the orbital angular momentum components and angular positions of pseudothermal light. The presence of these correlations is manifested through distinct interference structures in the orbital angular momentum-mode distribution of random light. These novel forms of interference correspond to the azimuthal analog of the Hanbury Brown and Twiss effect [4]. This family of effects can be of fundamental importance in applications where entanglement is not required

and where correlations in angular position and orbital angular momentum suffice. We also suggest that the azimuthal Hanbury Brown and Twiss effect can be useful in the exploration of novel phenomena in other branches of physics and in astrophysics

4.2 The rich physics in random fields of light

In 1956, Hanbury Brown and Twiss revolutionized optical physics with the observation of a new form of interference produced by correlations of the intensity fluctuations of light from a chaotic source. Their stellar interferometer collected light produced by independent sources on the disc of a star and detected at two different locations on Earth [12]. The observation of a second-order interference effect in this configuration was intriguing because at that time it appeared that classical and quantum theories of light offered different predictions [91]. Ever since, this effect has motivated extensive studies of higher-order classical correlations and their quantum counterparts in optics, as well as in condensed matter and particle physics [92–95]. Fundamental bounds have been established for the degree of correlation for a wide variety of degrees of freedom, such as in polarization, time, frequency, position, transverse momentum, angular position and orbital angular momentum (OAM) [21, 96, 97].

The random nature of light is an essential element of the HBT effect. Moreover, the random properties of light have been investigated and applied in a wide variety of other contexts. For example, speckled light, intimately related to pseudothermal light,

has played a fundamental role in the development of optical physics, imaging science, and nanophotonics. In addition, the study of fundamental processes such as transport phenomena, localization of light, optical vortices, and optical correlations has led to the development of novel physics produced as a consequence of the chaotic properties of light [98–103]. These results have motivated interest in the design of random lasers and of disordered structures that scatter light in random directions, which serve as sources of pseudothermal light [104].

As identified by Berry, optical vortices produced by the interference of random waves are intrinsic elements in chaotic light[105, 106]. Interest in this field has exploded since the recognition of a special class of vortices that carry OAM, characterized by an azimuthal phase dependence of the form $e^{i\ell\phi}$, where ℓ is the OAM mode number and ϕ is the azimuthal angle [17]. The azimuthal properties of light, described by the conjugate variables of angular position and OAM, have shown potential for technological applications in information science, remote sensing, imaging, and metrology [107]. In astrophysics, recent theoretical studies have predicted that rotating black holes can imprint an OAM spectrum onto light. The measurement of this spectrum could lead to an experimental demonstration of the existence of rotating black holes [108]. In addition, the optical vortex coronagraph has allowed the observation of dim exoplanets by canceling a diffraction-limited image of a star [109]. More recently, it has been proposed to use rotational Doppler shifts for astronomy [54].

In this chapter, we show that random fluctuations give rise to the formation of intensity correlations among the OAM components and among the angular positions of pseudothermal light. Furthermore, we show that the presence of these correlations leads to a variety of complex interference structures that correspond to the azimuthal analog of the HBT effect. In the original HBT experiment, two detectors were used at different locations to gain information about the physical size of a distant incoherent source. In our experiment, we use two detectors to measure intensity correlations between two OAM components of an incoherent source with controllable spatial and temporal coherence. We show that such correlations unveil the azimuthal structure of the source, which is shaped in the form of double angular slits in our realization. We study the far-field pattern by projecting it onto various OAM modes, and measure first- and second-order interference patterns of this structure. We identify two key signatures of the azimuthal HBT effect. The first is that HBT interference can show features in the OAM mode distribution at both the frequency and at twice the frequency of the first-order coherence produced by coherent light. The second consists of a shift of the interference structure when plotted as a function of OAM. We find that each of these effects depends on the strength of the fluctuations of the pseudothermal light. We also study the nature of the correlations between different OAM components and between different angular positions of pseudothermal light, and we find that these depend on the strength of the fluctuations as well. These effects correspond to the classical counterpart of azimuthal Einstein-Podolsky-Rosen (EPR) correlations [97],

and throughout this chapter, we highlight the similarities and differences between thermal and quantum correlations as manifested in the azimuthal degree of freedom.

4.3 Origin of HBT interference in the OAM domain

As in the original HBT experiment, we collect light from two portions of a random field. This is carried out through the use of two angular slits. We represent the optical field after the slits as

$$\Psi(r,\phi) = \mathcal{E}(r)\Phi(r,\phi)[A(\phi) + A(\phi - \phi_0)]. \tag{4.1}$$

Here, $\mathcal{E}(r)$ represents the coherent optical field produced by a laser, $\Phi(r,\phi)$ is a particular realization of a random phase screen, and $A(\phi)$ describes the transmission function of the angular slits. $A(\phi)$ is centered at 0 radians, and, therefore, $A(\phi - \phi_0)$ is centered at ϕ_0. We next consider the projection of the optical field of Eq. 4.1 onto a set of OAM modes. The result of such a measurement is described by the quantity $a_{p\ell}$ defined as $\int r\,dr\,d\phi\,(2\pi)^{-1/2}R_p^*(r)e^{-i\ell\phi}\Psi(r,\phi)$, where $R_p^*(r)$ is a radial mode function with radial index p and ℓ is the OAM index. Consequently, the measured intensity for each OAM projection I_ℓ is equal to $\sum_p \left|a_{p\ell}\right|^2$. The average of the intensity over an

ensemble of different realizations of the fluctuating field is then given by

$$\langle I_\ell \rangle = \frac{\alpha^2 \mathrm{sinc}^2\left(\alpha\ell/2\right)}{2\pi^2} \int r\, dr |\mathcal{E}(r)|^2 \left\{2 + e^{-i\ell\phi_0}\langle\Phi^*(r,0)\Phi(r,\phi_0)\rangle + e^{i\ell\phi_0}\langle\Phi^*(r,\phi_0)\Phi(r,0)\rangle\right\}, \tag{4.2}$$

where α is the width of the slits, and the ensemble average is denoted by $\langle ... \rangle$. It is evident that the angular double slit gives rise to Young's (first-order) interference in the OAM-mode distribution of the optical field and that this interference is dependent on the angular separation of the two slits, ϕ_0. Furthermore, the visibility of the interference pattern is determined by the terms $\langle\Phi^*(r,0)\Phi(r,\phi_0)\rangle$ and $\langle\Phi^*(r,\phi_0)\Phi(r,0)\rangle$, which quantify the field correlation between two different angular positions. These terms are sensitive to the phase difference of the field at two points. Consequently, the interference visibility becomes smaller as the degree as spatial coherence is reduced.

In direct analogy to the HBT experiment, in which two detectors measure the transverse momentum (far-field) distribution of a random field emitted from two locations of a star, we measure the correlation between two OAM components of light emitted from a random source shaped as two angular slits. Similar to linear position and linear momentum, angular position and OAM are conjugate variables and form a Fourier pair. Thus, we consider the second-order coherence function $G^{(2)}_{\ell_1,\ell_2} = \langle I_{\ell_1} I_{\ell_2} \rangle$, which is the key quantity that describes the azimuthal HBT effect. This quantity is a measure of the intensity correlations between the components of the the field with OAM values ℓ_1 and ℓ_2.

We consider a special case in which we measure the the second-order correlation at symmetrically displaced OAM values of ℓ and $-\ell$. In the context of the original experiment of HBT, this situation would involve measuring the receiving apertures by equal amounts in opposite directions. To analyze this situation, we need to determine the second-order coherence function $G^{(2)}_{\ell,-\ell} = \langle I_\ell I_{-\ell}\rangle$. We find that this quantity can be expressed (see Appendix B) as

$$\langle I_\ell I_{-\ell}\rangle = \mathcal{G}_0 + \mathcal{G}_\ell + \mathcal{G}_{2\ell}. \tag{4.3}$$

The intensity correlation function thus consists of three contributions. The first is a constant term denoted by $\mathcal{G}_0$ whose form is shown in the Appendix B. The second term, $\mathcal{G}_\ell$, describes an interference pattern that oscillates in ℓ at the same frequency as $\langle I_\ell\rangle$ and is given by

$$\mathcal{G}_\ell = \frac{\alpha^2 \operatorname{sinc}^2(\alpha\ell/2)}{2\pi^2} \int r_1 dr_1 r_2 dr_2 |\mathcal{E}(r_1)|^2 |\mathcal{E}(r_2)|^2 \Big(e^{-i\ell\phi_0}\{\langle\Phi^*(r_1,0)\Phi(r_1,\phi_0)\rangle + \langle\Phi^*(r_2,\phi_0)\Phi(r_2,0)\rangle\} + \text{c.c.}\Big). \tag{4.4}$$

The last term, $\mathcal{G}_{2\ell}$, shows an interference pattern that oscillates in the OAM value ℓ with twice the frequency of $\langle I_\ell\rangle$ and it is given by

$$\mathcal{G}_{2\ell} = \frac{\alpha^4 \operatorname{sinc}^4(\alpha\ell/2)}{4\pi^4} \int r_1 dr_1 r_2 dr_2 |\mathcal{E}(r_1)|^2 |\mathcal{E}(r_2)|^2 \Big(e^{-2i\ell\phi_0}\{\langle\Phi^*(r_1,0)\Phi(r_1,\phi_0) \times \Phi^*(r_2,\phi_0)\Phi(r_2,0)\rangle\} + \text{c.c.}\Big). \tag{4.5}$$

We see that the contribution $\mathcal{G}_\ell$ depends on a phase-sensitive term $\langle \Phi^*(r,0)\Phi(r,\phi_0)\rangle$ that decreases in magnitude with increasing randomness induced by field fluctuations. The visibility of this contribution to the interference pattern thus decreases with increasing field fluctuations. However the contribution $\mathcal{G}_{2\ell}$ is proportional to a positive-definite quantity $\langle |\Phi(r,0)|^2 |\Phi(r,\phi_0)|^2\rangle$ that survives even in the presence of the fluctuations in the chaotic field.

4.4 Experimental demonstration of azimuthal HBT interference

Our experimental setup is depicted in Fig. 4.1 (A and B). We use a solid state laser working at 532 nm along with a digital micro-mirror device (DMD) and a $4f$ optical system containing two lenses and a spatial filter in the Fourier plane to isolate one order of diffraction from the DMD. We first impress a sequence (at a 1.4-kHz writing rate) of random transverse structures having Kolmogorov statistics onto the beam to simulate thermal light [16, 110, 111]. For details, see Appendix C. This procedure modifies the spatial and temporal coherence of the beam in a fashion similar to the modification induced by a rotating ground glass plate [112] (see the intensity distribution of the beam in Fig. 4.1 C), which is often used to produce light with thermal statistics. We quantify the spatial coherence of the beam by means of the Fried coherence length r_0[113]. The strength of spatial phase variations within the beam increases as r_0

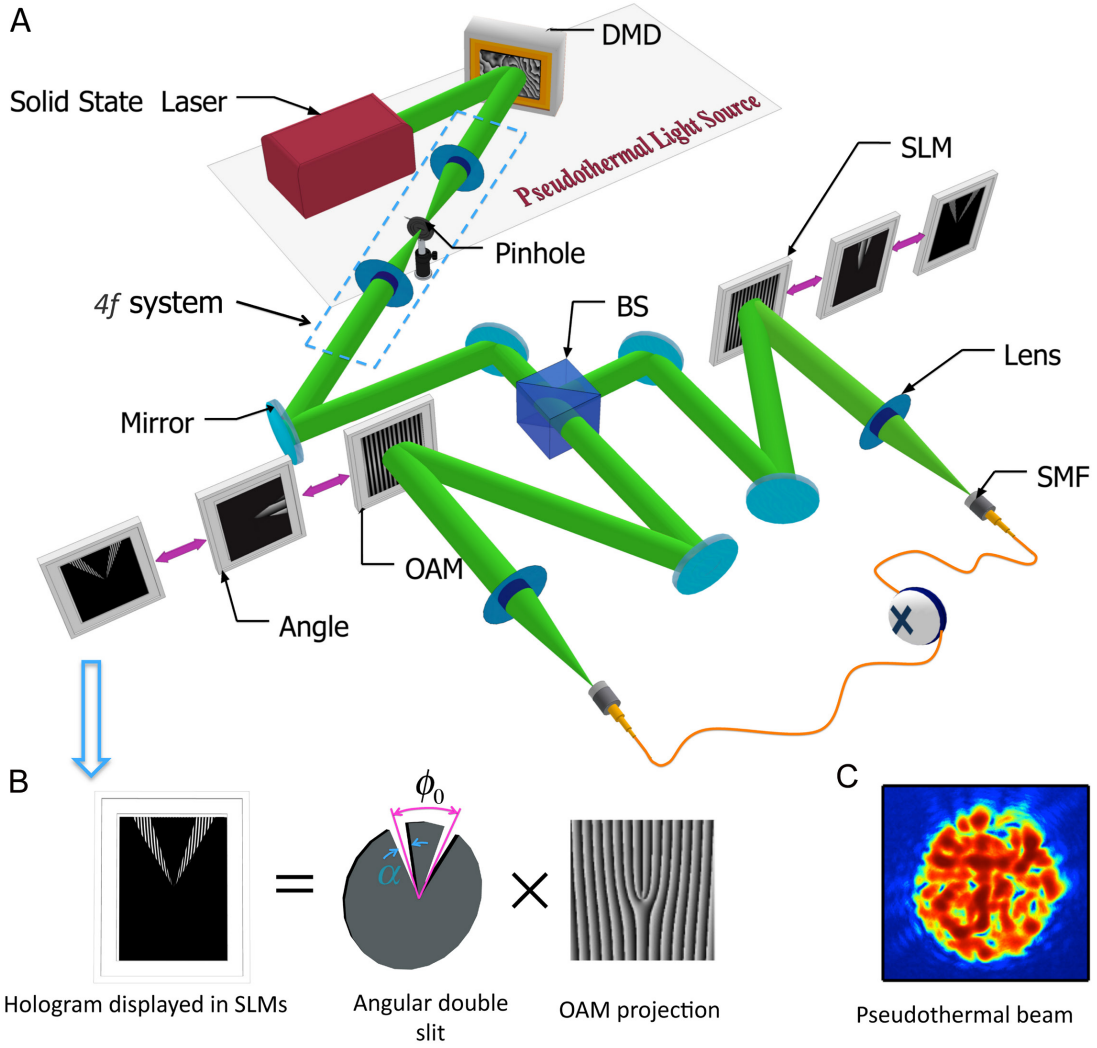

Figure 4.1: Experimental setup for the study of the azimuthal HBT effect. (A) The 532 nm output of a solid laser is directed onto a digital micro-mirror device (DMD), where a random transverse phase structure is impressed onto the beam. A $4f$ optical system consisting of two lenses with different focal lengths (figure not to scale) and a pinhole is used to isolate the first diffraction order from the DMD, which is a pseudothermal beam of light. This beam is then passed through a beam splitter (BS) to create two identical copies. Each copy is sent to a separate spatial light modulator (SLM) onto which a computer-generated hologram is encoded. (B) For the HBT measurements, a pair of angular slits is encoded onto the SLMs. In addition, forked holograms corresponding to OAM values are encoded onto the same holograms to project out controllable OAM components. For our measurements of the OAM and angular-position correlation functions, we do not use the double slit but simply project onto OAM values or angular wedges, respectively. (C) Intensity distribution of a generated pseudothermal beam of light.

decreases. By virtue of ergodicity, iterating through an ensemble of such holograms results in random phase fluctuations in time characterized by the parameter r_0. The structured beam is then split into two parts at a beam splitter, and each is imaged onto a spatial light modulators (SLM). On each SLM, a pair of angular slits and a forked diffraction grating are encoded (see Fig. 4.1B). The first diffraction order of the SLM is collected by a single-mode optical fiber (SMF), measured by avalanche photodiodes (APDs), and their degree of correlation is then computed. The time window for determining coincidence events is set to 42 ns, and the total accumulation time is set to 15 s.

We begin with the measurement of first-order (Young's) interference in the OAM domain, which can be observed in the OAM-mode distribution of light measured by either of the two detectors. For each value of ℓ, we impress several hundred random phase screens onto the DMD, all characterized by the same value of r_0, and we then calculate the correlation of the intensity. We repeat the experiment for all ℓ in the range $\ell = -15$ to $\ell = +15$. We perform this task by encoding holograms onto the SLMs in which the two angular apertures are multiplied by different forked diffraction gratings (see Fig. 4.1B). The OAM-mode distributions of the field as given by $\langle I_\ell \rangle$ are shown in Fig. 4.2 (A to D). Fig. 4.2 A shows the interference obtained when spatially coherent light is used, and Fig. 4.2 (B to D) shows the interference for different regimes of pseudothermal light, as characterized by successively decreasing values of r_0. The visibility is seen to decrease with the decrease of the spatial coherence of the source.

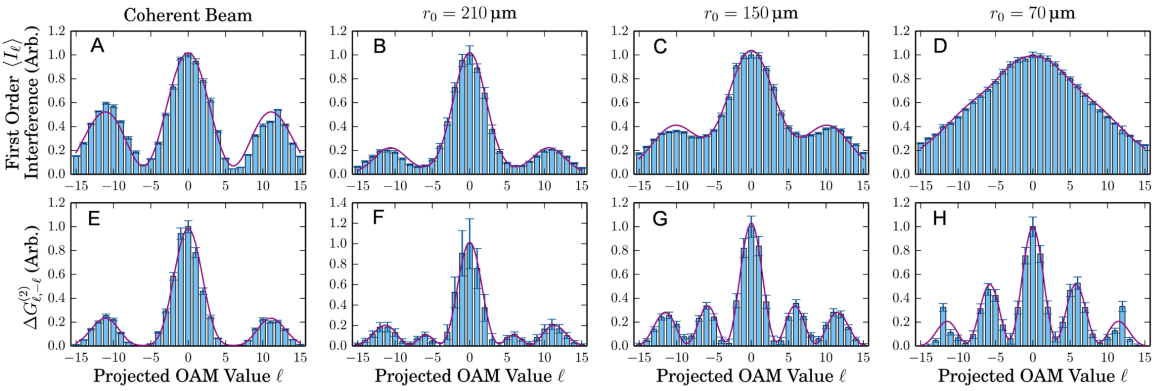

Figure 4.2: Interference transitions in the OAM-mode distribution of light. (A to D) First-order (Young's) interference. (E to H) Second-oder HBT interference. The first column (A and E) shows interference produced by coherent light, whereas the other panels show the measured interference for different strengths of the fluctuations of pseudothermal light, as characterized by the Fried coherence length. In each case, the angular width of the slits α is $\pi/12$ and the angular separation of the slits ϕ_0 is $\pi/6$. Bars represent data, whereas the line is the theoretical curve predicted by theory.

We next study second-order coherence. Our experimental results for the second-order coherence function $\Delta G^{(2)}_{\ell,-\ell}$, defined as $\mathcal{G}_\ell + \mathcal{G}_{2\ell}$, are shown in Figs. 4.2 (E to H). For a coherent beam (Fig. 4.2 E), $\mathcal{G}_\ell$ is the dominant contribution to $\Delta G^{(2)}_{\ell,-\ell}$. We reach this conclusion by noting that the data oscillate at the same frequency as the first-order interference shown in Fig. 4.2A and by recalling the discussions of Eqs. (4.4) and (4.5). We also note that $\mathcal{G}_\ell$ decreases as the degree of the spatial coherence of the source is reduced, making $\mathcal{G}_{2\ell}$ the dominant contribution in this case; we reach this conclusion by an examination of Eq. (4.5), which shows that $\mathcal{G}_{2\ell}$, in contrast to $\mathcal{G}_\ell$, does not decrease with decreasing degree of spatial coherence of the source. We see this behavior in the sequence of results shown in Figs. 4.2 (F to H). For example, in Fig. 4.2F, the contribution from $\mathcal{G}_{2\ell}$ is smaller than that from $\mathcal{G}_\ell$. This transition

is marked by the formation of second-order correlations in the angular position and OAM variables.

It is interesting that there is a regime of random fluctuations for which strong frequency-ℓ oscillations are seen in the first-order interference while strong frequency-2ℓ oscillations are seen in the second-order interference (see Figs. 4.2, B and F). Note also that, for the case of quantum correlations, entangled photons do not produce interference in singles but only in correlations such as those shown in Fig. 4.2 (D and H) [21, 100]. The interplay between $\mathcal{G}_\ell$ and $\mathcal{G}_{2\ell}$ might be useful to the study of the relationship between coherence and the quantum nature of light.

It is important to remark that different degrees of coherence define regimes of the HBT effect [114], as shown in Fig. 4.2. In our case, the varying relative magnitude of the three terms contributing to the second-order coherence $\mathcal{G}^{(2)}_{\ell,-\ell}$ results in different shapes (see Eq. 4.3). For example, $\mathcal{G}_{2\ell}$ makes the pattern in Fig. 4.2E sharper, but the same term changes the frequency of the interference structure in Fig. 4.2H.

The general form of the azimuthal HBT effect is obtained when the intensity correlations are calculated for arbitrary mode indices ℓ_1 and ℓ_2. As discussed above, the HBT effect depends on the degree of coherence of the source. Specifically, an interesting feature is observed for the partially coherent regime characterized by r_0 equal to 150 μm. In our experimental study of this situation, we hold the OAM value measured in one arm of our interferometer fixed at the value ℓ_0 whereas we vary the OAM value in the other arm. We set the value of ℓ_0 first to $+2$ and later to -2. In

the other arm, we perform measurements for each value in the range $\ell = -15$ to $+15$. The results of these measurements are shown in Fig. 4.3. It should be noted that the OAM spectrum plotted as a function of the the OAM value of arm 2 is shifted left (see Fig. 4.3A) or right (Fig. 4.3B) depending on the value of OAM chosen for arm 1. The procedure used in the measurement is analogous to using one fixed detector and one moving detector in the original setup of HBT [12]. The results of Fig. 4.3 (A and B) are described by the quantity $\langle I_\ell I_{\ell_0} \rangle$ and can be expressed in terms of five contributing terms (see Appendix B).

For the strength of fluctuations that we used for these measurements, one of the detectors measures an interference pattern equal to the one shown in Fig. 4.2C, whereas the other measures a noisy but constant signal. When the correlation of the two signals is calculated, the visibility of the interference pattern is dramatically increased and shifted in the OAM-mode distribution of the field. Effectively, we are using the random fluctuations of the field to increase the fringe visibility. For example, if instead of projecting an OAM value equal to 2 or -2 as we did, we could project on ℓ equal to zero and retrieve the original but improved pattern with increased visibility. This effect could find importance in realistic applications. These effects manifest the presence of second-order correlations in the OAM components and angular positions of pseudothermal light.

We would like to emphasize that although the angular slits and the forked holograms for OAM projections are realized on the same SLMs, they correspond to conceptually

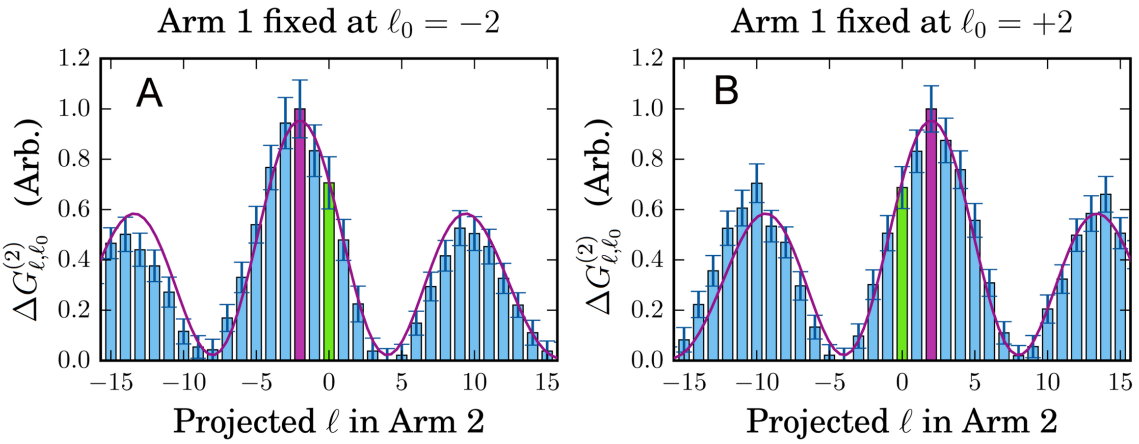

Figure 4.3: Experimental demonstration of the azimuthal HBT effect of light. (A and B) $\Delta G^{(2)}_{\ell,\ell_0}$ plotted as a function of the OAM value of arm 2 for two different values of the OAM number of arm 1. The green bar shows the center of the interference pattern for singles counts shown in Fig. 2C, whereas the purple bar shows the center of the displayed interference pattern.

distinct components of the experiment. The angular slits are used to provide a nontrivial azimuthal structure for the incoherent source, whereas the forked holograms are used to measure correlations in the OAM domain.

4.5 Measurement of angular momentum correlations and angular position correlations

Now we explore the nature of the underlying fluctuation-induced correlations in OAM and in angular position that lie at the origin of the HBT effect. The superposition of randomly fluctuating waves produces an OAM spectrum that broadens with the degree of fluctuation in the source of pseudothermal light. In the present experiment, the OAM spectrum is controlled by setting r_0 equal to 70 μm. This situation produces

a broad OAM spectrum that remains almost constant over the range of OAM values that we measure. We use the same setup as that of Fig. 4.1, although we omit the two angular slits that we used in the studies of azimuthal HBT interference effects reported above. On the first SLM (see Fig. 4.1), we display a forked hologram corresponding to a fixed value of OAM, whereas on the second SLM, we display a series of holograms with different values of OAM. The measured intensity for a single value of OAM $\langle I_\ell \rangle$ that is projected out using the SLM can be approximated as $\int r^2 dr^2 d\phi^2 |\mathcal{E}(r)|^2 \, g(r)^2$, where $g(r)$ is the Gaussian mode supported by the SMF (see Appendix B).

In Fig. 4.4A, we plot the measured value of $g^{(2)} = \langle I_{\ell_1} I_{\ell_2} \rangle / \langle I_{\ell_1} \rangle \langle I_{\ell_2} \rangle$. We find a strong positive correlation between the OAM values measured in the two arms. As shown in Appendix B, in the limit of a strong fluctuations, second-order correlations in the OAM degree of freedom can be described by

$$\langle I_{\ell_1} I_{\ell_2} \rangle = \langle I_{\ell_1} \rangle \langle I_{\ell_2} \rangle (1 + \delta_{\ell_1, \ell_2}). \tag{4.6}$$

Our experimental results show crosstalk between different OAM numbers that is not predicted by Eq. 4.6. This crosstalk results from experimental imperfections in the projective measurement process used to characterize OAM. The correlations in Fig. 4.4A show two significant differences from the quantum correlations observed in spontaneous parametric down conversion (SPDC). The first is that SPDC shows strong anti-correlations of the the two OAM values. This behavior is a consequence of the conservation of OAM in a parametric nonlinear optical process. The second

difference is the presence of a background term (the “1" in Eq. 4.6), which prevents the existence of perfect correlations.

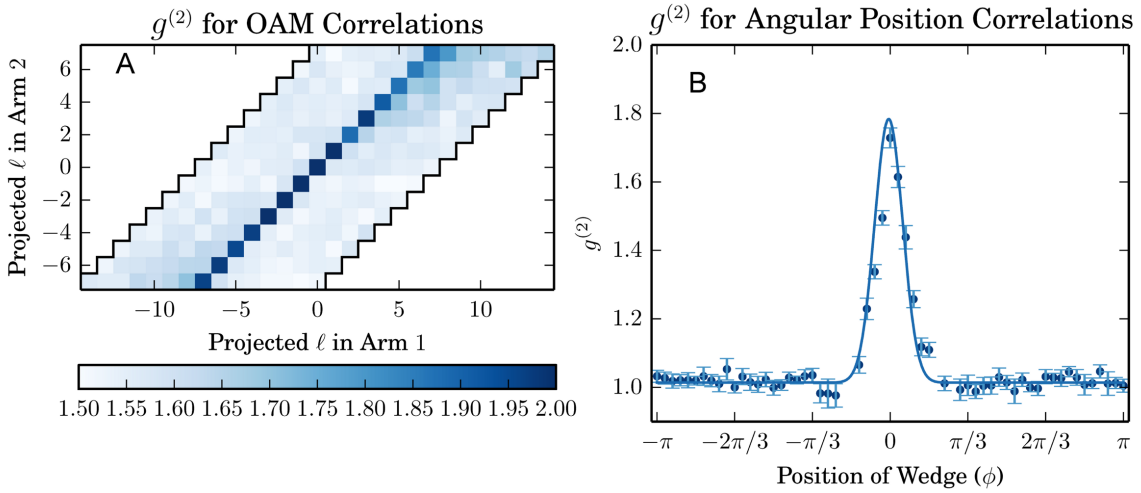

Figure 4.4: Measurement of intensity correlations in the angular domain for random light. (A) Normalized second-order correlation function in the OAM domain. (B) Presence of strong correlations for the conjugate space described by the angular position variable.

Randomly fluctuating beams also produce correlations in angular position. These correlations are investigated by encoding angular apertures onto the SLMs. In order to make our measurements precise, we utilize narrow angular apertures of $\pi/15$ radian size. We keep one aperture at a fixed location, and we measure correlations for 60 different angular positions of the other aperture. Because of rotational symmetry, this procedure permits the full characterization of correlations in angular position. As shown in Fig. 4.4B, for this level of fluctuation, the intensities of the projected angular apertures are strongly correlated, and the nature of these correlations can be approximated by $\langle I_\phi I_{\phi_0}\rangle = \langle I_\phi\rangle\langle I_{\phi_0}\rangle(1 + f(\phi - \phi_0))$. In this equation, the subscript ϕ refers to the arm where the variable-position angular aperture is placed and ϕ_0

represents the arm with the fixed-position aperture. Also, $f(\phi - \phi_0)$ represents some strongly peaked function (see Appendix B).

As we have shown throughout this paper, the HBT correlations of pseudothermal light lead to effects that show resemblance to those previously observed with entangled photons [21, 58, 97, 115]. The reason for this behavior is that, in contrast to the degree of second-order coherence that describes coherent light, the functions that describe second-order correlations in angular position and OAM for random fields are nonseparable. For example, Eq. 4.6 does not contain the product of the averaged intensities measured by each of the two detectors. The presence of a term that describes point-to-point correlations (in this case, the delta function δ_{ℓ_1,ℓ_2}) does not allow the factorization of the degree of coherence as the simple product of intensities between the two arms. As a consequence, the HBT structures are also described by a nonseparable function, and its frequency, visibility, and shifts increase with the fluctuations of the source or the strength of angular position and OAM correlations. As the strength of the fluctuations decreases, the nonseparable part of the function tends to vanish, and thus, the second order correlation function can be factorized in terms of OAM or angular position. A separable function will not lead to the HBT effect in the OAM-mode distribution of light; see the transition shown in Fig. 4.2.

Intensity correlation in the OAM components and angular position of pseudothermal light show similarities with the azimuthal EPR effect, observed in photons entangled in angular position and OAM [97]. However, our results show that for

pseudothermal light, the correlations are present but not perfect, unlike the case of entangled photons where the correlations are perfect. Thus, it is impossible to violate, for example, the azimuthal EPR criterion $(\Delta\ell)^2(\Delta\phi)^2 \geq 1/4$. However, as shown in Fig. 4.4, our correlations are stronger for same values of OAM or angular positions. For example, if background subtraction is performed, the variance product for $\Delta\ell$ and $\Delta\phi$ is similar to that achieved for nonclassical light. For our experimental results $(\Delta\ell)^2(\Delta\phi)^2$ is 0.054, of similar order to the one reported by Leach *et al*. [97]. The uncertainties were measured by performing a least squares fit of the data to a Gaussian distribution and recording the standard deviation of the result. Note that this does not imply a violation of the EPR criterion.

4.6 Summary

The azimuthal HBT effect unveils fundamental physics that can be applied to develop novel applications that exploit OAM correlations in random light. We believe that many interesting protocols for remote sensing and object identification that use azimuthal correlations in entangled photons will be able to exploit azimuthal correlations in random light and the azimuthal HBT effect [58, 115, 116]. Furthermore, in recent years, researchers have developed interest in utilizing beams carrying OAM for applications in astronomy, but unfortunately the propagation through random media produces chaotic phase fluctuations and optical vortices [116–120]. These effects pose serious problems for methods based on OAM of light, limiting their applications [107, 121].

However, it has been shown that second-order interference effects are less sensitive to the coherence properties of the source. This is one of the advantages of the HBT interferometer against the Michelson interferometer [122]. In addition, it has been demonstrated that imaging schemes based on second-order correlations are robust against turbulence [123]. Therefore, we suggest that the azimuthal HBT effect offers the possibility of exploring novel phenomena in astrophysics, one example being the relativistic dynamics produced by rotating black holes [108].

We have demonstrated that random fluctuations of light give rise to the formation of intensity correlations in the OAM components and angular positions of pseudothermal light. These correlations are manifested through a new family of interference structures in the OAM-mode distribution of pseudothermal light that can be described by the azimuthal HBT effect. We have shown how the strength of the random fluctuations of light determines various regimes for this effect. In addition, we identified two key features of the azimuthal HBT effect. The first is characterized by a structure in which the OAM frequency is doubled with respect to the interference produced by a coherent beam of light. The second is marked by a shift of the OAM spectrum with a change in the OAM reference value. We anticipate that these properties of random optical fields will be fundamentally important for applications where quantum entanglement is not required and where correlations in angular position and OAM suffice.

Chapter 5

Compressive Tracking using Quantum Correlations

5.1 Introduction

In the previous chapter we discussed the physical processes that give rise to the formation of second-order classical correlations in the azimuthal degree of freedom. However, quantum correlations in the variables of linear position and linear momentum have been an important subject of interest in the last 20 years and a wide variety of fundamental and applied research has been performed. One representative research area is quantum imaging, this area has progressed so fast and a wide variety of applications have been proposed. Here we present a compressive sensing protocol that tracks a moving object by removing static components from a scene. The implementation is carried out on a ghost imaging scheme to minimize both the number of photons and the number of measurements required to form a quantum image of the tracked object. This procedure tracks an object at low light levels with fewer than 3%

of the measurements required for a raster scan, permitting us to more effectively use the information content in each photon.

5.2 Compressive Sensing and Quantum Imaging

As discussed in Chapter 2, CS has recently been of great utility in quantum optical and low-light level applications, for instance, single-photon level imaging, entanglement characterization and ghost imaging [71, 73, 124, 125]. CS provides a resource-efficient alternative to single-photon arrayed detectors, permitting us to reduce operational problems involved in systems employing raster scanning [72].

Ghost imaging is a technique which employs correlations between two light fields to reproduce an image. For example, entangled photons exhibit strong correlations in many properties such as time-energy and position-momentum. One photon of an entangled pair illuminates an object and is collected by a bucket detector, which does not provide spatial information. Its entangled partner photon is then incident on a spatially resolving detector gated by the first photon's bucket detector. Remarkably, an image of the object appears on the spatially resolving detector, even though its photon never directly interacted with the object [126].

Compressive ghost imaging [71] allows one to replace the spatially resolving detector with a bucket detector. This procedure reduces both acquisition times for systems based on raster scanning and the required number of measurements for retrieving

images[72]. These improvements have motivated an ongoing effort to implement technologies based on ghost imaging such as image encryption [127], quantum sensors [128], object identification [129] and most recently ghost imaging ladar [130].

In spite of the advantages that technologies based on ghost imaging offer, they can be hard to implement in practice. Most current quantum optical technologies work at the single photon level, and are unfortunately vulnerable to noise and are inefficient, requiring many photons and many measurements [131]. To reduce these limitations, we apply an efficient form of compressive sensing. This allows us to overcome the main problems which undermine the practical application of many attractive correlated optical technologies. To demonstrate these improvements, we implement a ghost object tracking scheme that significantly outperforms traditional techniques. This opens the possibility of using correlated light in realistic applications for sparsity-based remote-sensing.

5.3 Compressive Object Tracking using Entangled Photons

We present a proof-of-principle experiment based on a quantum ghost imaging scheme that allows us to identify changes in a scene using a small number of photons and many fewer realizations than those established by the Nyquist-Shannon criterion. [132] Object tracking and retrieval is performed significantly faster in comparison to

previous protocols [71, 72, 101, 126, 133]. This scheme uses compressive sampling to exploit the sparsity of the relative changes of a scene with a moving object. With this approach we can identify the moving object and reveal its trajectory. Our strategy involves removing static components of a scene and reduces the environmental noise present during the measurement process. This leads to the reduction of the number of measurements that we take and the number of photons required to form an image, both important issues in proposals for object tracking and identification [129, 134]. The reduction of noise and removal of static components of a scene is carried out by subtracting two observation vectors, corresponding to two realizations of a scene. We call this technique ghost background subtraction. Our results demonstrate that this technique is adequate for object tracking at low light levels.

Consider the ghost imaging scheme depicted in Fig. 5.1. A laser pumps a nonlinear crystal oriented for type-I SPDC. The approximated output state is given by first order perturbation theory, which leads us to the following two-photon entangled state:

$$|\Psi\rangle = \int d\vec{k}_g d\vec{k}_o f(\vec{k}_g + \vec{k}_o)\hat{a}_g^\dagger(\vec{k}_g)\hat{a}_o^\dagger(\vec{k}_o)\,|0\rangle. \tag{5.1}$$

We refer to the down-converted photons as the ghost and object photons denoted by the subindices g and o, respectively. The two-photon probability amplitude, which is responsible for the transverse momentum correlations existing between the ghost and object photons, is represented by the non-factorizable function $f(\vec{k}_g + \vec{k}_o)$, where

k is the transverse wavevector of the ghost or object photon. The form of this function depends on the phase-matching conditions, but it is often approximated by a double gaussian function [135]. This two-photon entangled state is strongly anti-correlated in transverse momentum, such that if the transverse momentum of the object photon is measured, the transverse momentum of the ghost photon is found to have the same magnitude and opposite direction. These momentum anti-correlations allow us to perform quantum ghost imaging.

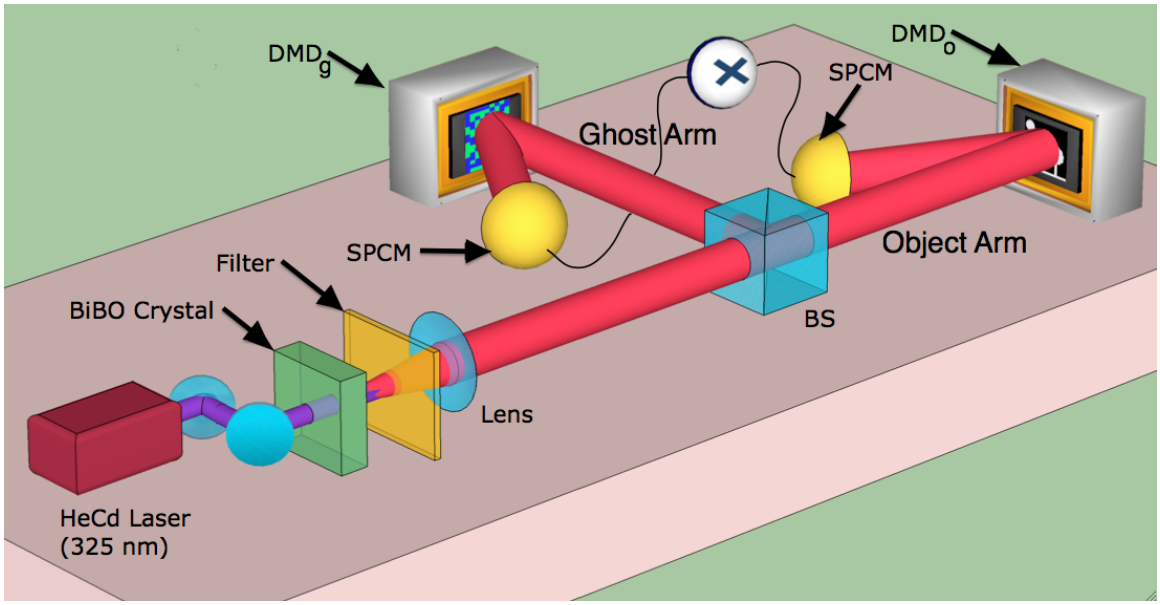

Figure 5.1: Entangled photons at 650 nm are generated in a Bismuth Barium Borate (BiBO) crystal through type-I degenerate SPDC. The far field of the BiBO crystal is imaged onto two DMDs with a lens and a BS. One DMD is used to display the object we want to track, while the other is used to display random binary patterns. Single-photon counting modules (SPCMs) are used for joint detection of the ghost and object photons.

In our experiment, we use DMDs to impress spatial information onto the entangled photon pair. The DMDs work by controlling the retro-reflection of each individual pixel on the display. After each photon is reflected by a DMD, a single-photon counting module (SPCM) counts the number of photons in it. The correlations between the two down-converted photons allows one to correlate the images displayed in the DMDs.

We jointly detect photons pairs reflected off a changing scene O and a series of random matrices A_m. The subindex m indicates the m-th realization. The coincidence counts between the two detectors are given by

$$J_m \propto \int d\vec{\rho}_{\mathrm{DMD}} \left| A_m \left(\frac{\vec{\rho}_{\mathrm{DMD}}}{m_r} \right) \right|^2 \left| O \left(\frac{\vec{-\rho}_{\mathrm{DMD}}}{m_o} \right) \right|^2, \tag{5.2}$$

where A_m and O are the reflectivity functions displayed on the DMD_g located in the ghost arm and on DMD_o in the object arm, respectively. Meanwhile m_r and m_o are their corresponding magnification factors. These are determined by the ratio of the distance between the nonlinear crystal to the lens and the distance from the lens to DMD_g or DMD_o. In our experiment m_r and m_o, are equal. $\vec{\rho}_{\mathrm{DMD}}$ represents the transverse coordinates of one of the DMDs.

Eq. 5.2 critically shows that the joint-detection rate is proportional to the spatial overlap between the images displayed on DMD_o and DMD_g. This behavior can be interpreted as a nonlocal projection, which demonstrates the suitability for implementing compressive sensing techniques nonlocally with ghost imaging [72].

Compressive sensing uses optimization to recover a sparse n-dimensional signal from a series of m incoherent projective measurements, where the compression comes from the fact that $m < n$. Image reconstruction via compressive sensing consists of a series of linear projections [136]. Each projection is the product of the image O consisting of n pixels, with a pseudorandom binary pattern A_m. Each pattern produces a single measurement, which constitutes an element of the observation vector J. After a series of m measurements, a sparse approximation $\hat{O}$ of the original image O can be retrieved by solving the optimization problem, known as total variation minimization [74], given by Eq. 5.3.

$$min_{\hat{O}\in C^n} \sum_i \left\| D_i\hat{O} \right\|_1 + \frac{\mu}{2} \left\| A\hat{O} - J \right\|_2^2. \tag{5.3}$$

$D_i\hat{O}$ is a discrete gradient of $\hat{O}$ at pixel i, μ is a weighting factor between the two terms, and A is the total sensing matrix containing all the pseudorandom matrices A_m. Each matrix A_m is represented into a 1D vector and constitutes a row of the total sensing matrix A. The algorithm known as "Total Variation Minimization by Augmented Lagrangian and Alternating Direction" (TVAL3) allows us to solve the aforementioned problem. The solution of the optimization problem allows us to recover the image $\hat{O}$, which is the compressed version of the original image O, with a resolution given by the dimensions of the matrix A_m. The original image O is characterized by a sparsity number k, which means that the image can be represented in a certain sparse basis where k of its coefficients are nonzero. The number of performed measurements

m is greater than the sparsity number k, but far fewer than the total number of pixels n contained in the original image. The constraints imposed in the recovery algorithm minimize the noise introduced during the measurement process.

We are able to compressively track and identify a moving object in a scene by discarding static pixels. A scene with a moving object possesses static elements that do not provide information about the object's motion or trajectory. These redundancies can be discriminated from the moving object as follows. Let us consider the projection of two different frames onto the same pseudorandom pattern. Each projective measurement picks up little information about the components of a frame. If the two projective measurements produce the same correlation value, it would imply that the two frames are identical and we are retrieving meaningless information which can be ignored. The opposite case would reveal information about the changes in a scene.

This protocol is formalized as follows. Two different correlation vectors, J^j and J^{j-1}, corresponding to two consecutive frames are subtracted, giving ΔJ. This introduces the following important modification to Eq. 5.3.

$$min_{\hat{O}\in C^n} \sum_i \left\| D_i \Delta\hat{O} \right\|_1 + \frac{\mu}{2} \left\| A\Delta\hat{O} - \Delta J \right\|_2^2. \tag{5.4}$$

The subtracted vector ΔJ is sparser than both J^j or J^{j-1}, thus requiring fewer measurements for its reconstruction. This corresponds to fewer realizations of A_m,

and hence smaller sensing matrix A. Furthermore, subtracting the background in this manner mitigates the environmental noise present during the tracking process. The retrieved image $\Delta\hat{O}$ will provide information about the relative changes in the scene.

5.4 Experimental Results

Our experimental setup is sketched in Fig. 5.1. A 325 nm, continuous-wave HeCd laser pumps a type-I phase matched BiBO crystal to produce degenerate entangled photon pairs at 650 nm. Two interference filters are placed after the nonlinear crystal. The first is a low pass filter that removes the pump and the second is a 650/12 nm narrowband filter that transmits the down-converted photons. A beam splitter probabilistically separates the two photons into ghost and object modes. An 88 mm focal length lens puts the far field of the crystal at the location of DMD. Two free space detectors receive the light reflected from the DMDs by means of two collection lenses with a 25 mm focal length. One DMD is used to display a scene with a moving object while the other is used to impress a series of random binary patterns. Coincidence counts are obtained within a 3 ns time window.

We apply this method to a scene with a flying object. The static components of the scene are a house, the moon and a tree. The object moves a certain distance in each iteration of the scene (insets of Fig. 5.2). We first reconstruct a compressed ghost image of the static frame of the scene, which represents the background. In order to

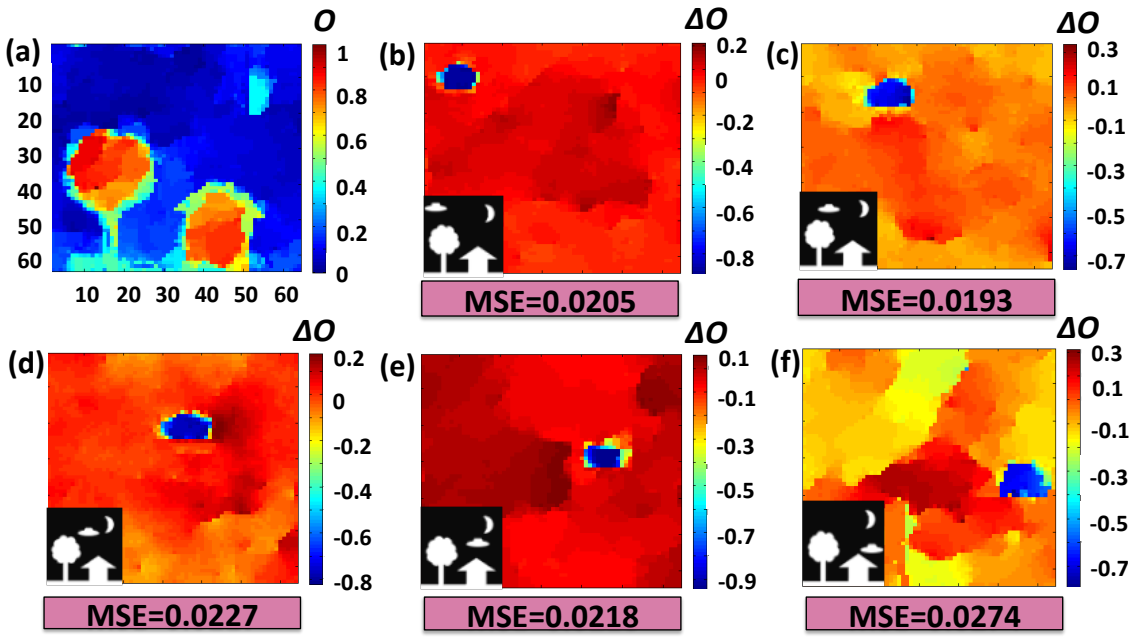

Figure 5.2: Compressed ghost image of (a) the background of the scene and (b-f) the tracked object in different positions. These reconstructions were obtained by defining different ΔJ vectors with 400 elements, corresponding to the number of measurements. The insets show the original frames of the scene displayed on the DMD.

do this, we put 2000 different random patterns on DMD_g, with DMD_o displaying the background scene. These realizations represent 49% of a raster scan. For each random pattern, we count coincidence detections for 8 s. Typical single count rates were 13.8 x 10^3 counts/s for the ghost and object arms with the coincidence counts approximately 2% of the single counts. Fig. 5.2(a) shows the retrieved background scene $\hat{O}$. After this, subsequent frames of the scene with the object in different positions are displayed on DMD_o. After applying the optimization algorithm, the moving object was clearly identified as shown in Figs. 5.2(b)-(f). The reconstructions were done using 400 patterns, which represents 9.7% the measurements of a raster scan. The negative values in the retrieved images are due to background subtraction and fluctuations in the measurements process.

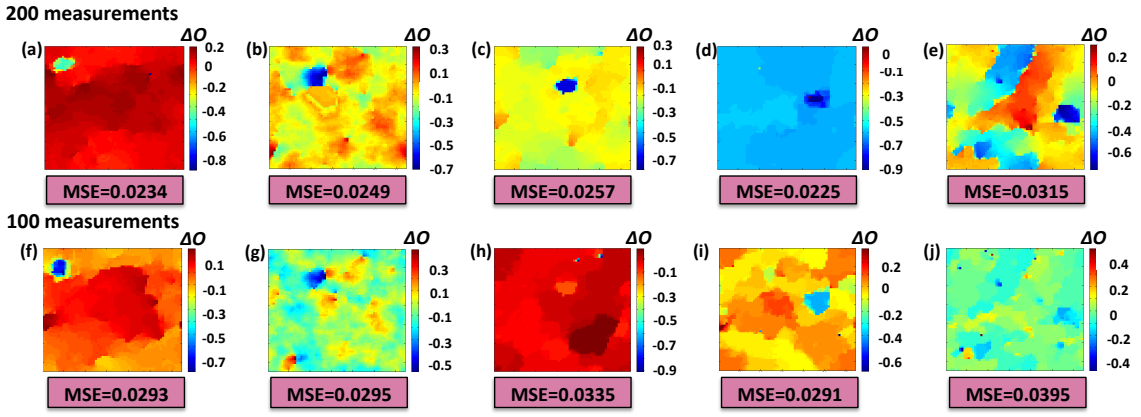

Figure 5.3: Reconstructed ghost image of (a-e) tracked object with 200 measurements. (f-j) same object with 100 measurements.

A straightforward examination of the limits of our protocol is carried out by reducing the number of measurements used to track an object. The images shown in Fig. 5.3 were reconstructed with only 200 and 100 measurements, corresponding

to 4.88% and 2.44% of the measurements of a raster scan. The metric employed to characterize the fidelity of these reconstructions is the mean-squared error[71] defined as $MSE = (1/n)\|O - \hat{O}\|^2$. The MSE is seen to increase as the number of measurements is decreased. Although, it is still possible to detect the object trajectory with just 100 measurements.

The photon efficiency is studied by estimating the dependence of the MSE on the number of photons per measurement, for a fixed number of measurements. A simulation of the protocol was carried out by using the data employed in the experiment. In order to achieve realistic experimental conditions, dark and shot noise were introduced by means of poissonian distributions. The amount of dark noise was modeled based on the frequency distribution of counts obtained when both of the DMDs were turned off. We have considered reconstructions employing 100 and 400 measurements. Fig. 5.4 shows the dependence of image quality on the number of detected photons per measurement. The minimum number of photons per measurement needed to distinguish the silhouette of the object by eye are 500 photons/measurement and 200 photons/measurement for 100 and 400 measurements respectively. The estimated thresholds correspond to a MSE oscillating around 0.04. For the situation where an object was tracked with 100 measurements and 500 photons/measurement, we estimate that we can impress approximately 0.082 bits/photon. This is considering that for a binary image the number of pixels corresponds to the number of bits [137].

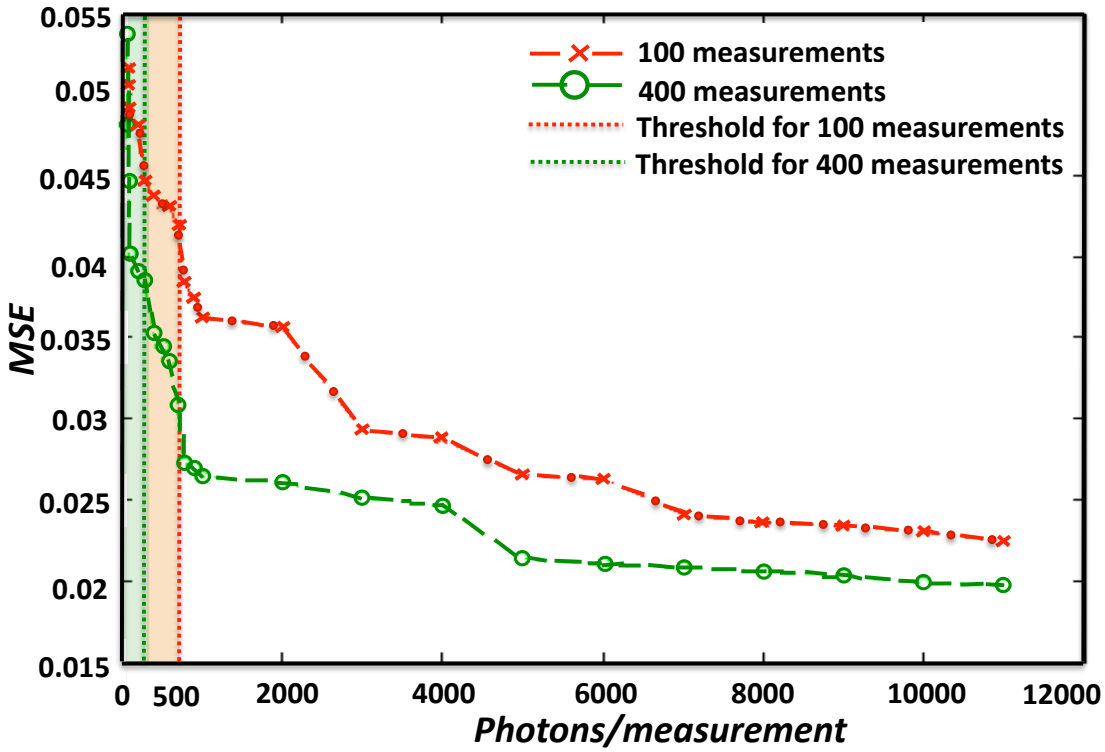

Figure 5.4: (Color online) Calculated mean-squared error of the compressed tracked object at the position shown in Fig. 2(b). Green (Red) line indicates the MSE using 400 (100) measurements. The thresholds indicate that a low quality image is retrieved and is not possible to track the object.

5.5 Summary

In this chapter we have proposed and demonstrated a proof-of-principle object-tracking protocol in a ghost imaging scheme. This protocol uses compressive sensing to exploit the sparsity existing between two realizations of a scene with a moving object. It also reduces the environmental noise introduced during the measurement process. Further, it allows us to perform image retrieval significantly faster by employing single pixel detectors. Our method is photon-measurement efficient, allowing us to track an object with only 2.44 % of the number of measurements established by the Nyquist criterion, even at low light levels. This economic procedure shows potential for real-life applications.

Chapter 6

The Born Rule and Looped Trajectories of Light

6.1 Introduction

The validity of the superposition principle and of Born's rule are well-accepted tenants of quantum mechanics. Surprisingly, it has recently been predicted that the intensity pattern formed in a three-slit experiment is seemingly in contradiction with the predictions of the most conventional form of the superposition principle when exotic looped trajectories are taken into account. However, the probability of observing such paths is typically very small and thus rendering them extremely difficult to measure. In this work, we confirm the validity of Born's rule and present the first experimental observation of these exotic trajectories as additional paths for the light by directly measuring their contribution to the formation of optical interference fringes. We accomplish this by enhancing the electromagnetic near-fields in the vicinity of the slits through the excitation of surface plasmons. This process effectively increases

the probability of occurrence of these exotic trajectories, demonstrating that they are related to the near-field component of the photon's wavefunction.

6.2 The Born Rule

The phenomenon of interference has been recognized as "the only mystery" of quantum mechanics [7]. The enormous interest and history of this fundamental effect can be traced back to the two-slit experiment devised by Thomas Young in the early 19th century. Young's experiment is conceptually the simplest method for demonstrating the superposition principle, as the appearance of interference fringes in the far-field is unexplainable unless it is understood that the particle seemingly travels through both slits simultaneously. Such an experiment, originally performed with light, has since been conducted on particles ranging from individual photons, neutrons, and atoms, to large molecules consisting of dozens of atoms [8]. As the superposition principle lies at the core of quantum physics, many of its counterintuitive features such as entanglement, non-locality, wave-particle duality, and delayed-choice concepts can be demonstrated or tested using a two-slit system [9, 11, 24, 138–141].

The standard interpretation of the two-slit experiment is given by solving the wave equation for an initially prepared complex wavefunction, ψ. For example, if ψ_A represents the wavefunction at the detector for a photon emerging from slit A, and ψ_B is the wavefunction for a photon emerging from slit B, then the implementation

of the superposition principle is to assume that the wavefunction is a superposition of the different paths given by $\psi_{AB} = \psi_A + \psi_B$. The probability of detection is given by Born's rule as

$$P_{\mathrm{AB}} \equiv |\psi_{\mathrm{AB}}|^2 = P_{\mathrm{A}} + P_{\mathrm{B}} + \left(\psi_{\mathrm{A}}^* \psi_{\mathrm{B}} + \psi_{\mathrm{A}} \psi_{\mathrm{B}}^*\right), \tag{6.1}$$

where $P_{\mathrm{A}} = |\psi_{\mathrm{A}}|^2$ and $P_{\mathrm{B}} = |\psi_{\mathrm{B}}|^2$. From this equation it is clear that the outcome of the two-slit experiment is given by the sum of outcomes from each slit alone, plus an additional interference term.

Due to the inherent structure of any wave theory, Born's rule always bounds the complexity of any effect involving superpositions of an arbitrary number of wavefunctions to a sum of terms denoting the interference between pairs of wavefunctions [142]. For instance, in accordance with Born's rule, the interference pattern obtained in a three-slit experiment can be described by the following probabilities

$$P_{\mathrm{ABC}} = P_{\mathrm{AB}} + P_{\mathrm{BC}} + P_{\mathrm{AC}} - P_{\mathrm{A}} - P_{\mathrm{B}} - P_{\mathrm{C}}. \tag{6.2}$$

Note that this expression does not include a probability term that involves three slits, but is entirely described by probabilities involving only one and two slits. Any possible contribution from higher-order interference terms (i.e., a path involving the three slits) has been quantified by the so-called Sorkin parameter [142, 143]

$$\epsilon = P_{\mathrm{ABC}} - P_{\mathrm{AB}} - P_{\mathrm{BC}} - P_{\mathrm{AC}} + P_{\mathrm{A}} + P_{\mathrm{B}} + P_{\mathrm{C}}, \tag{6.3}$$

which should be identically zero if only the direct paths through the three individual slits are considered. Sinha *et al.* [143] showed that ϵ can be evaluated experimentally by making a set of measurements for each term in Eq. (6.3).

Although it might appear that the measurement of a non-zero ϵ implies a clear violation of quantum mechanics [143], De Raedt *et al.* demonstrated by numerically solving Maxwell's equations that a non-zero value of ϵ can exist without such violation [144]. Later it was found that this result is a consequence of the presence of exotic looped trajectories of light (e.g. red curve in Fig. 6.1a) that arise in the Feynman path integral formulation with extremely low probability of occurrence [145]. This interpretation was subsequently shown to agree with the exact numerical solution of the wave equation [146].

In this work we demonstrate that looped trajectories of photons are physically due to the near-field component of the wavefunction, which leads to an interaction among the three slits. As such, it is possible to increase the probability of occurrence of these trajectories by controlling the strength and spatial distribution of the electromagnetic near-fields around the slits. By a proper control of the conditions in a three-slit experiment, we successfully demonstrate a dramatic increase of the probability of photons to follow looped trajectories, and present the first successful measurement of a non-zero value of ϵ.

6.3 Origin of the looped trajectories of light

Under the scalar wave approximation, the propagation of light is described by the Helmholtz equation

$$\left(\nabla^2 + k^2\right)\psi(\mathbf{r}) = 0, \tag{6.4}$$

subject to the boundary conditions specifying the physical setup. This equation can be solved by computing the propagation from any point $\mathbf{r}_1$ to any other point $\mathbf{r}_2$ via the Green's function kernel, which according to Rayleigh-Sommerfeld theory is given by

$$K(\mathbf{r}_1, \mathbf{r}_2) = \frac{k}{2\pi i}\,\frac{e^{ik\,|\mathbf{r}_1 - \mathbf{r}_2|}}{|\mathbf{r}_1 - \mathbf{r}_2|}\chi, \tag{6.5}$$

where χ is an obliquity factor [147]. This equation satisfies Eq. (6.4) and the Fresnel-Huygens principle in the form of the following propagator relation

$$K(\mathbf{r}_1, \mathbf{r}_3) = \int \mathrm{d}\mathbf{r}_2 K(\mathbf{r}_1, \mathbf{r}_2) K(\mathbf{r}_2, \mathbf{r}_3). \tag{6.6}$$

If one repeatedly applies Eq. (6.6), the path-integral formulation of the propagation kernel is obtained in the form [148]

$$K(\mathbf{r}_1, \mathbf{r}_2) = \int \mathcal{D}[x(\mathbf{s})] \exp\left(ik \int \mathrm{d}\mathbf{s}\right), \tag{6.7}$$

where $\int \mathcal{D}[x(\mathbf{s})]$ is the functional integration over paths $x(\mathbf{s})$. The boundary conditions can be included by restricting the possible paths $x(\mathbf{s})$. If one is concerned only with

diffraction from slits in a single plane, then Eq. (6.7) can be perturbatively expanded as [145]

$$K = K_1 + K_2 + K_3 + \cdots , \tag{6.8}$$

where K_n represents the nth application of Eq. (6.6) and each integration is carried over the plane containing the slits, see Appendix C.

Solving the wave equation taking $K = K_1$ is equivalent to considering only direct paths, such as the paths in Fig. 6.1b. These paths propagate from the source and through one of the slits to the detector. We call these wavefunctions ψ_{A}, ψ_{B} and ψ_{C}. The higher-order terms in Eq. 6.8 are responsible for the looped trajectories of photons that propagate from the source to a slit, and *to at least one other slit* before propagating to the detector (see Fig. 6.1c). It follows that the wavefunction of a photon passing through the three slits is given by

$$\psi_{\mathrm{ABC}} = \psi_{\mathrm{A}} + \psi_{\mathrm{B}} + \psi_{\mathrm{C}} + \psi_{\mathrm{L}}, \tag{6.9}$$

where ψ_L represents the contribution of the looped trajectories to the wavefunction ψ_{ABC}. Note that in general ϵ, as defined by Eq. 6.3, is not zero because of the existence of these looped trajectories. Thus, the presence of looped paths leads to an apparent deviation of the superposition principle [145] (see Appendix C).

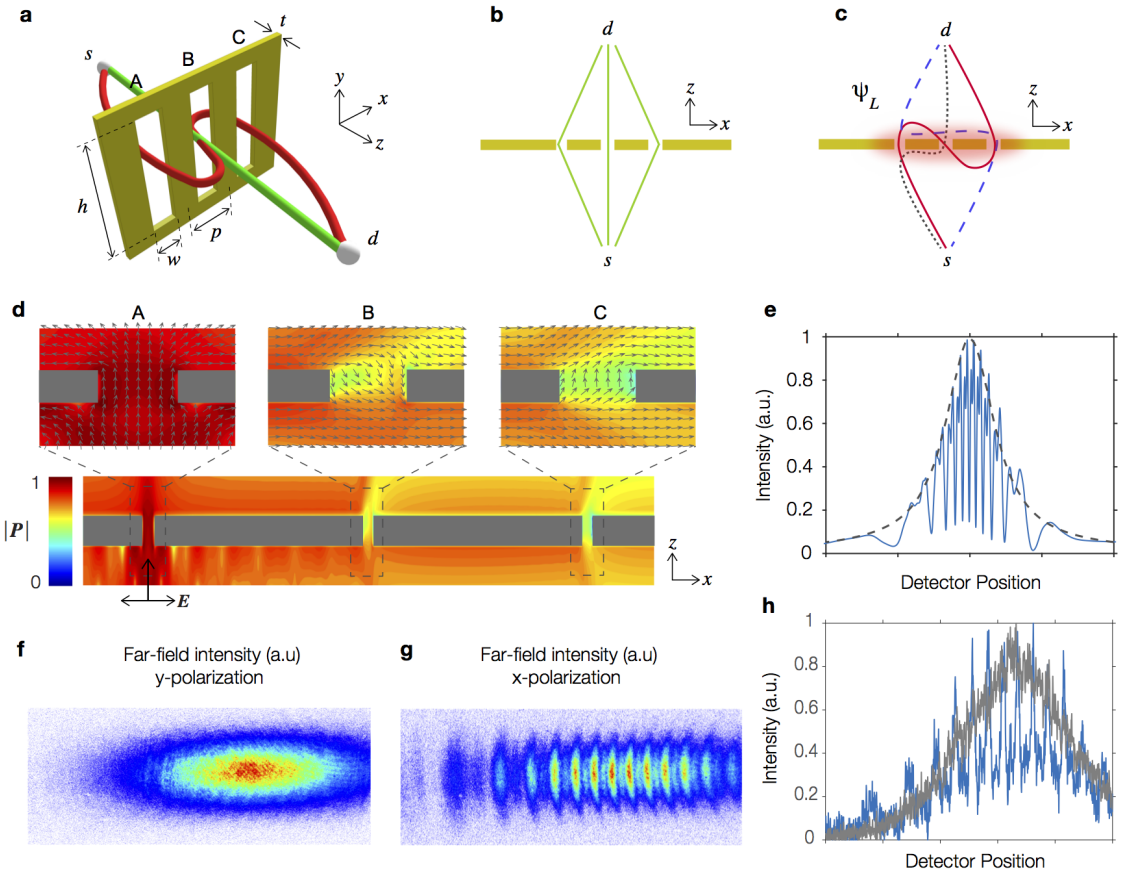

Figure 6.1: Trajectories of light in a three-slit interferometer. a, The three-slit structure considered in this study. The red path going from point s to point d illustrates a possible looped trajectory of light. b, Direct trajectories of light resulting from considering only the first term in Eq. (C.2). The widely used superposition principle, i.e. Eq. (6.1), accounts only for these direct trajectories. c, Examples of exotic looped trajectories arising from the higher order terms in Eq. (C.2). The red cloud in the vicinity of the slits depicts the near-field distribution, which increases the probability of photons to follow looped trajectories. d, Normalized Poynting vector $\mathbf{P}$ in the vicinity of the three slits obtained through full wave simulations at a wavelength $\lambda = 810$ nm, using $w = 200$ nm, $p = 4.6$ μm, $t = 110$ nm, and $h = \infty$. The simulations consider a Gaussian beam excitation polarized along x, and focused onto slit A. The Poynting vector clearly exhibits a looped trajectory such as the solid path in c. e, Far-field interference patterns calculated under x-polarized (solid) and y-polarized (dashed) optical excitation. Interference fringes are formed in the far field only when strong near fields are excited (x-polarization), and occur from the interference of light following a direct trajectory and a looped trajectory. f, Experimental evidence that shows the far-field pattern for a situation in which only one slit is illuminated with y-polarized light from an attenuated laser. g, The presence of exotic looped trajectories leads to an increase in the visibility of the far-field pattern. This effect is observed when x-polarized light illuminates one of the slits. h, The transverse profile of the patterns shown in f and g.

6.4 Increasing the probability of occurrence of the looped trajectories of light

The conclusion that ψ_{ABC} is not simply the superposition of the wavefunctions ψ_{A}, ψ_{B}, and ψ_{C} is a consequence of the actual boundary conditions in a three-slit structure. Changing the boundary conditions affects the near-field components around the slits, but it typically does not affect the far-field distribution because of the short range extension of the near fields [149]. As shown below, the looped trajectories of photons are physically due to the near-field components of the wavefunction. Therefore, by controlling the strengths and the spatial distributions of the near-fields around the slits, it is possible to drastically increase the probability of photons to undergo looped trajectories, thereby allowing a straightforward visualization of their effect in the far-field interference pattern. To demonstrate this phenomenon, a three-slit structure was designed such that it supports surface plasmons, which are strongly confined electromagnetic fields that can exist at the surface of metals [150, 151]. The existence of these surface waves results in near fields that extend over the entire region covering the three slits [152, 153], thereby increasing the probability of looped trajectories.

As a concrete example, we consider the situations depicted in Fig. 6.1d and 6.1e. First, we assume a situation in which the incident optical field is a Gaussian beam polarized along the long axis of the slit (y polarization) and focused to a 400-nm spot size onto the left-most slit. For this polarization, surface plasmons are not appreciably

excited and the resulting far-field distribution is the typical envelope, with no fringes, indicated by the dashed curve in Fig. 6.1e. This intensity distribution is described by the quantity $|\psi_{\mathrm{A}}|^2$. The presented results were obtained through a full-wave numerical analysis based on the finite-difference-time-domain (FDTD) method, on a structure with dimensions $w = 200$ nm, $p = 4.6$ μm, and $t = 110$ nm and at a wavelength $\lambda = 810$ nm (see Appendix C). The height of the slit, h, was assumed to be infinite. Interestingly, the situation is very different when the incident optical field is polarized along the x direction. The Poynting vector for this situation is shown in Fig. 6.1d. This result shows that the Poynting vector predominantly follows a looped trajectory such as that schematically represented by the solid path in Fig. 6.1c. The resulting far-field interference pattern, shown as the solid curve in Fig. 6.1e, is an example of the interference between a straight trajectory and a looped trajectory. Thus, it is clear that the naive formulation of the superposition principle does not provide an accurate description for the case where near fields are strongly excited.

6.5 Experimental Results

First, we experimentally verify the role that looped trajectories have in the formation of interference fringes. For this purpose we exclusively illuminate one of the three slits. This experiment is carried out in the setup shown in Fig. 6.2a. As shown in Fig. 6.1f, no interference fringes are formed when the light illuminating the slit is y-polarized. Remarkably, when the illuminating light is polarized along the x direction the visibility

of the far-field pattern is dramatically increased, see Fig. 6.1g and h. This effect unveils the presence of looped trajectories. In our experiment, the contributions from looped trajectories are quantified through the Sorkin parameter by measuring the terms in Eq. (6.3). To this end, we measured the interference patterns resulting from the seven arrangements of slits depicted in Fig. 6.2b, thus the illumination field fills each arrangement of slits. In this case, the experiment was carried out using heralded single-photons with wavelength of 810 nm produced via degenerate parametric down-conversion (see Appendix C). The single photons were weakly focused onto the sample, and the transmitted photons were collected and collimated by an infinity-corrected microscope objective (see Fig. 6.2c). The resulting interference pattern was magnified using a telescope and recorded using an ICCD camera, which was triggered by the detection event of the heralding photon. The strength of the near fields in the vicinity of the slits was controlled by either exciting or not exciting surface plasmons on the structure through proper polarization selection of the incident photons.

The scanning electron microscope images of the fabricated slits are shown in the first row of Fig. 6.3. The dimensions of the slits are the same as those used for the simulation in Fig. 6.1, with $h = 100$ μm being much larger than the beam spot size (~ 15 μm). The interference patterns obtained when the contribution from near-field effects is negligible (y polarization) are shown in the second row, while those obtained in the presence of a strong near fields in the vicinity of the slits (x polarization) are shown in the third row. These interference patterns are obtained by adding 60

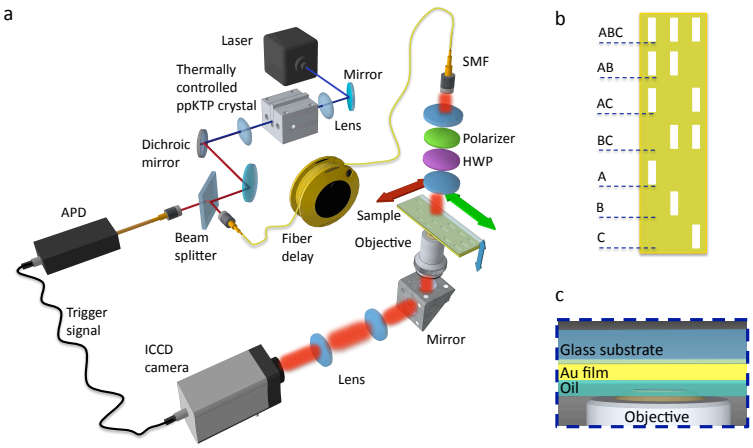

Figure 6.2: Experimental setup utilized to measure exotic trajectories of light. a, Sketch of the experimental setup used to measure the far-field interference patterns for the various slit configurations. b, The seven different slit arrangements used in our study. This drawing is not to scale; in the actual experiment each slit structure was well separated from its neighbors to avoid undesired cross talk. c, Detail of the structure mounted on the setup. The refractive index of the immersion oil matches that of the glass substrate creating a symmetric index environment around the gold film.

background-subtracted frames, each of which is captured within a coincidence window of 7 nsec over an exposure time of 160 sec (see insets in Fig. 6.3). Only the pattern for P_{AB} is shown in Fig. 6.3 because P_{AB} and P_{BC} produce nearly identical patterns in the far field, a similar situation occurs for P_{A}, P_{B} and P_{C}. The bottom panels show detail views of the interference patterns measured along an horizontal line.

Note that the intensities of the interference patterns (i.e., the probability amplitudes) for the two polarizations scale differently for each arrangement of slits. This is shown by the ratios of the position-averaged probabilities, P_x/P_y, indicated at the bottom of Fig. 6.3. The significant changes in the probabilities obtained with x-polarized photons ultimately lead to a value of ϵ that significantly deviate from zero. This interesting effect is produced by constructive and destructive interference among looped trajectories, whose probability has been increased through the enhancement of the near fields, see Appendix C.

We quantify the contribution from the looped trajectories through the normalized Sorkin parameter, defined as $\kappa \equiv \epsilon/I_{\mathrm{max}}$ with I_{max} being the intensity at the central maximum of the three-slit interference pattern [145]. Both theoretical and experimental values of this parameter are shown in Fig. 6.4a. The theoretical values were obtained via FDTD simulations, while the experimental values were calculated from the results in Fig. 6.3. Clearly, we observe that when the near fields are *not* enhanced, the parameter κ is much smaller than the uncertainty associated with our measurements. However, when the near fields are enhanced, κ is dramatically increased due to the

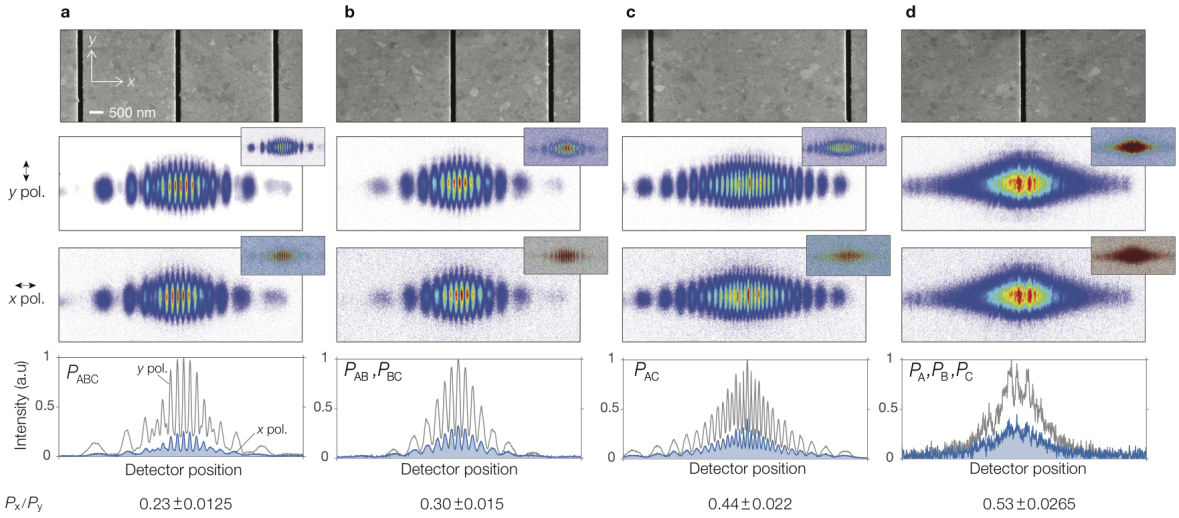

Figure 6.3: Experimental results. a–d, Measured interference patterns corresponding to the various probability terms in Eq. (6.3) (indicated as a label within each panel of the bottom). In this case the illumination field fills each arrangement of slits. The first row shows scanning electron microscope images of the slits used for the measurements. The second and third panels show, respectively, the background-subtracted interference patterns formed when 60 frames, such as those in the insets are added, for the situations in which the probabilities of looped trajectories are negligible (using y-polarized illumination), and when such probabilities are increased due to the enhancement of near fields (using x-polarized illumination). Each of the frames shown in the insets was taken with an ICCD camera using heralded single-photons as a source. The bottom show the intensity dependence of the interference pattern measured along a horizontal line on the second and third panels. The ratio of the average probabilities obtained using x-polarized illumination to those obtained using y-polarized illumination, P_x/P_y, is shown at the bottom. All the measurements are conducted at a wavelength $\lambda = 810$ nm, and using structures with dimensions $w = 200$ nm, $h = 100$ μm and $p = 4.6$ μm

increased probability for the looped trajectories [145], enabling the measurement of this parameter despite experimental uncertainties. Taking as a reference the central maximum of the κ profile, the experimental results indicate that the contribution of looped trajectories has been increased by almost two orders of magnitude.

Finally, we show that it is possible to control the probability of photons undergoing looped trajectories by modifying the dimensions of the three slit structure or by changing the wavelength of the optical excitation. Fig. 6.4b and 6.4c show theoretical predictions and experimental data at the central maximum for different slit parameters and wavelengths. These measurements were taken with classical light from a tunable diode laser. Fig. 6.4b shows the normalized Sorkin parameter for a situation in which looped trajectories significantly contribute to the formation of interference fringes, whereas Fig. 6.4c shows the same parameter for a situation in which near-field effects, and consequently looped trajectories, are negligible. In general, we note that the theoretical and experimental results are in good agreement, with the observed discrepancies being attributed to experimental uncertainties due to imperfections in the fabricated sample and due to the limited dynamic range of the camera.

6.6 Conclusions

We have demonstrated that exotic looped paths occur as a physical consequence of the near-field component of the wave equation. As such, it is possible to control

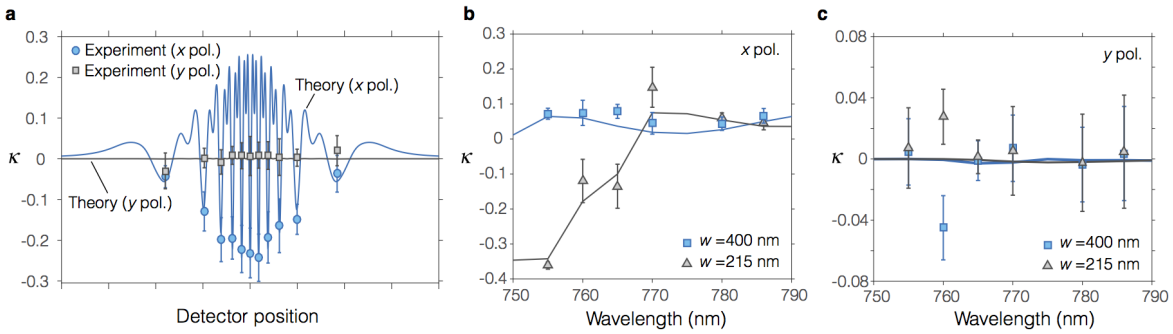

Figure 6.4: Quantifying the contribution of looped trajectories through the normalized Sorkin parameter, κ. a shows numerical and experimental results, for a sample with $w = 200$ nm, $h = 100$ μm and $p = 4.6$ μm and an illuminating field consisting of heralded single-photons at a wavelength of 810 nm. The experimental points are obtained by measuring κ at different peaks of the interference patterns shown in Fig. 3. b shows theoretical and experimental evidence at the central maximum for different widths and for various wavelengths for an attenuated laser diode, in this case the contributions from looped paths makes the κ different from zero. c shows a situation in which looped trajectories are not enhanced and consequently κ is almost zero. These results confirm that the strengths of looped trajectories can be controlled by engineering the size of the slits and the wavelength of the illuminating field. These values of κ were measured at the center of the interference pattern. The labels x and y indicate the polarization state of the incident light.

the probability of occurrence of such paths by controlling the strength and spatial distribution of the near-fields around the slits. By doing so, we have shown a drastic increase in the probability of photons to follow looped paths, leading to the first experimental observation of such exotic trajectories in the formation of interference fringes. We believe that looped paths can have important implications in the study of decoherence mechanisms in interferometry and to increase the complexity of protocols for quantum random walks, quantum simulators and other algorithms used in quantum computation.

Chapter 7

Conclusions

In this thesis we introduced a series of exotic interference effects that were utilized to unveil novel behaviors of light. These findings offer the possibility of exploring new physics of light in classical and quantum contexts. We also proposed different schemes that demonstrate the possibility of developing optical technologies for different purposes.

In the first chapters of this thesis we discussed weak measurements in the context of weak value amplification and direct measurement. We also pointed out that the underlying nature behind weak value amplification and direct measurement are interference effects. In addition, we introduced a new form of interferometric weak values in the variables of angular position and orbital angular momentum. We demonstrate that these weak values can be used to amplify angular rotations. In the second part of Chapter 2 we described how self-interference mediated by compressive

sensing can be utilized to effectively measure the spatial wave function of photons in a direct fashion.

The Wigner function has been recognized as a fundamental tool in optical physics and quantum optics, in Chapter 3 we introduced a technique that allows one to directly measure the Wigner distribution in the azimuthal quadratures described by the angular position and orbital angular momentum of light. In addition, we utilized our interferometric technique to measure the density matrix of high-dimensional states. We also showed how the first-order properties of coherence for a classical beam can be easily determined through our technique. Finally, we demonstrate its efficiency by measuring the Wigner function and density matrices for single photons carrying orbital angular momentum.

In Chapter 4, we exploited the rich physics behind random optical fields to demonstrate the formation of intensity correlation in the orbital angular momentum components and angular position of pseudothermal light. We showed that the presence of these correlations is manifested through distinct interference structures in the orbital angular momentum-mode distribution of random light. We found that these novel forms of interference correspond to the Hanbury Brown and Twiss effect for twisted light. We predict that this family of effects can be of fundamental importance in applications where entanglement is not required and where correlations suffice. We also suggest that the azimuthal Hanbury Brown and Twiss effect can be useful in the exploration of novel phenomena in other branches of physics and astrophysics.

Quantum imaging utilizes quantum correlations to form images that benefit greatly from the quantum properties of light. Unfortunately, the low photon flux in spontaneous parametric down conversion and the fragile nature of photons impose important limitations for realistic applications. In Chapter 5, we introduced a compressive sensing protocol that is implemented in a quantum imaging scheme to minimize both the number of photons and the number of measurements required to form a quantum image of a moving object. Our experiment demonstrated a form that allows one to more effectively use the information content in each photon.

As mentioned along this thesis, the famous two-slit interferometer revolutionized the field of physics in the early 19th century. Remarkably, this experiment keeps surprising the scientific community and it is the basis of many striking effects in quantum mechanics. In Chapter 6, we showed the first experimental evidence that demonstrates the existence of exotic looped trajectories in a three-slit interferometer. We also unveiled the physical process that lead to this remarkable effect. The evidence presented in this thesis opens the door for new research directions in the field of optical physics and quantum optics.

References

[1] O. S. Magana-Loaiza, M. Mirhosseini, B. Rodenburg, and R. W. Boyd. Amplification of Angular Rotations using Weak Measurements. *Phys. Rev. Lett.* **112**, 200401 (2014).

[2] M. Mirhosseini, O. S. Magana-Loaiza, S. M. Hashemi Rafsanjani, and R. W. Boyd. Compressive direct measurement of the quantum wavefunction. *Phys. Rev. Lett.* **115**, 090402 (2014).

[3] M. Mirhosseini, O. S. Magana-Loaiza, C. Chen, S. M. Hashemi Rafsanjani, and R. W. Boyd. Wigner Distribution of Twisted Photons. *Phys. Rev. Lett.* **116**, 130402 (2016).

[4] O. S. Magana-Loaiza, M. Mirhosseini, R. M. Cross, S. M. Hashemi Rafsanjani, and R. W. Boyd. Hanbury Brown and Twiss interferometry with twisted light. *Sci. Adv.* **2**, e1501143 (2016).

[5] O. S. Magana-Loaiza, G. Howland, M. Malik, J. C. Howell, and R. W. Boyd. Compressive Object Tracking using Entangled Photons. *Appl. Phys. Lett.* **102**, 231104 (2013).

[6] J. S. Lundeen, B. Sutherland, A. Patel, C. Stewart, and C. Bamber. Direct measurement of the quantum wavefunction. *Nature* **474**, 188–191 (2011).

[7] L. Mandel. Quantum effects in one-photon and two-photon interference. *Rev. Mod. Phys.* **71**, 6861 (1999).

[8] D. M. Greenberger, M. A. Horne, and A. Zeilinger. Multiparticle Interferometry and the Superposition Principle. *Phys. Today* **46**, 22 (1993).

[9] P. Shadbolt, J. C. F. Mathews, A. Laing, and J. L. O'Brien. Testing foundations of quantum mechanics with photons. *Nat. Phys.* **10**, 278–286 (2014).

[10] T. Young. The Bakerian Lecture: On the theory of light and colours. *Phil. Trans. R. Soc.* **92**, 12–48 (1802).

[11] M. O. Scully, B.-G. Englert, and H. Walther. Quantum optical tests of complementarity. *Nature* **351**, 111–116 (1991).

[12] R. Hanbury Brown and R. Q. Twiss. Correlation Between Photons in Two Coherent Beams of Light. *Nature* **177**, 1–3 (1956).

[13] C. K. Hong, Z. Y. Ou, and L. Mandel. Measurement of subpicosecond time intervals between two photons by interference. *Phys. Rev. Lett.* **59**, 2044 (1987).

[14] J. D. Franson. Bell inequality for position and time. *Phys. Rev. Lett.* **62**, 1989 (1989).

[15] M. Born and E. Wolf. *Principles of Optics*. Oxford, 6th ed. ed. (1986).

[16] B. Rodenburg, M. Mirhosseini, O. S. Magana-Loaiza, and R. W. Boyd. Experimental generation of an optical field with arbitrary spatial coherence properties. *J. Opt. Soc. Am. B* **A51**, 120406 (2014).

[17] L. Allen, M. W. Beijersbergen, R. J. C. Spreeuw, and J. P. Woerdman. Orbital angular momentum of light and the transformation of Laguerre-Gaussian laser modes. *Phys. Rev. A* **45**, 8185 (1992).

[18] A. M. Yao and M. J. Padgett. Orbital angular momentum: origins, behavior and applications. *Adv. Opt. Photon.* **3**, 161 (2011).

[19] S. M. Barnett. Quantum theory of rotation angles. *Phys. Rev. A* **41**, 3427–3435 (1990).

[20] S. Franke-Arnold, S. M. Barnett, E. Yao, J. Leach, J. Courtial, and M. Padgett. Uncertainty principle for angular position and angular momentum. *New J. Phys.* **6**, 103–103 (2004).

[21] A. K. Jha, J. Leach, B. Jack, S. Franke-Arnold, S. M. Barnett, R. W. Boyd, and M. J. Padgett. Angular Two-Photon Interference and Angular Two-Qubit States. *Phys. Rev. Lett.* **104**, 010501 (2010).

[22] Y. Aharonov, D. Albert, and L. Vaidman. How the result of a measurement of a component of the spin of a spin-1/2 particle can turn out to be 100. *Phys. Rev. Lett.* **60**, 1351–1354 (1988).

[23] Y. Aharonov, A. Botero, S. Popescu, and B. Reznik. Revisiting Hardy's paradox: counterfactual statements, real measurements, entanglement and weak values. *Phys. Lett. A* **301**, 130 (2002).

[24] S. Kocsis, B. Braverman, S. Ravets, M. J. Stevens, R. P. Mirin, L. K. Shalm, and A. M. Steinberg. Observing the Average Trajectories of Single Photons in a Two-Slit Interferometer. *Science* **332**, 1170–1173 (2011).

[25] N. Ritchie, J. Story, and R. Hulet. Realization of a measurement of a "weak value". *Phys. Rev. Lett.* **66**, 1107–1110 (1991).

[26] J. Dressel, M. Malik, F. Miatto, R. W. Boyd, and A. Jordan. Colloquium: Understanding quantum weak values: Basics and applications. *Rev. Mod. Phys.* **86**, 307 (2014).

[27] A. Feizpour, X. Xing, and A. M. Steinberg. Amplifying Single-Photon Nonlinearity Using Weak Measurements. *Phys. Rev. Lett.* **107**, 133603 (2011).

[28] G. I. Viza, J. Martínez-Rincón, G. A. Howland, H. Frostig, I. Shomroni, B. Dayan, and J. C. Howell. Weak-values technique for velocity measurements. *Opt. Lett.* **38**, 2949–2952 (2013).

[29] H. F. Hofmann. Uncertainty limits for quantum metrology obtained from the statistics of weak measurements. *Phys. Rev. A* **83**, 022106 (2011).

[30] O. Hosten and P. Kwiat. Observation of the Spin Hall Effect of Light via Weak Measurements. *Science* **319**, 787–790 (2008).

[31] X.-Y. Xu, Y. Kedem, K. Sun, L. Vaidman, C.-F. Li, and G.-C. Guo. Phase Estimation with Weak Measurement Using a White Light Source. *Phys. Rev. Lett.* **111**, 033604 (2013).

[32] G. Strübi and C. Bruder. Measuring Ultrasmall Time Delays of Light by Joint Weak Measurements. *Phys. Rev. Lett.* **110**, 083605 (2013).

[33] L. J. Salazar-Serrano, D. Janner, N. Brunner, V. Pruneri, and J. P. Torres. Measurement of sub-pulse-width temporal delays via spectral interference induced by weak value amplification. *Phys. Rev. A* **89**, 012126 (2014).

[34] P. Dixon, D. Starling, A. Jordan, and J. Howell. Ultrasensitive Beam Deflection Measurement via Interferometric Weak Value Amplification. *Phys. Rev. Lett.* **102**, 173601 (2009).

[35] M. Malik, M. Mirhosseini, M. P. J. Lavery, J. Leach, M. J. Padgett, and R. W. Boyd. Direct measurement of a 27-dimensional orbital-angular-momentum state vector. *Nature Communications* **5**, 4115 (2014).

[36] J. Z. Salvail, M. Agnew, A. S. Johnson, E. Bolduc, J. Leach, and R. W. Boyd. Full characterization of polarization states of light via direct measurement. *Nature Photonics* **7**, 316–321 (2013).

[37] C. Ferrie and J. Combes. Weak Value Amplification is Suboptimal for Estimation and Detection. *Phys. Rev. Lett.* **112**, 040406 (2014).

[38] X. F. Qian and J. H. Eberly. Entanglement and classical polarization states. *Opt. Lett.* **36**, 4110–4112 (2011).

[39] K. H. Kagalwala, G. Di Giuseppe, A. F. Abouraddy, and B. E. A. Saleh. Bell's measure in classical optical coherence. *Nature Photonics* **7**, 72–78 (2012).

[40] G. Puentes, N. Hermosa, and J. P. Torres. Weak Measurements with Orbital-Angular-Momentum Pointer States. *Phys. Rev. Lett.* **109**, 040401 (2012).

[41] J. S. Lundeen and R. K. J. Practical measurement of joint weak values and their connection to the annihilation operator. *Phys. Lett. A* **334**, 337 (2005).

[42] R. Jozsa. Complex weak values in quantum measurement. *Phys. Rev. A* **76**, 044103 (2007).

[43] N. Brunner and C. Simon. Measuring Small Longitudinal Phase Shifts: Weak Measurements or Standard Interferometry? *Phys. Rev. Lett.* **105**, 010405 (2010).

[44] H. Kobayashi, K. Nonaka, and Y. Shikano. Stereographical Tomography of Polarization State using Weak Measurement with Optical Vortex Beam. *arXiv:1311.3357* (2013).

[45] V. Giovannetti, S. Lloyd, and L. Maccone. Advances in quantum metrology. *Nature Photonics* **5**, 222–229 (2011).

[46] N. Thomas-Peter, B. J. Smith, A. Datta, L. Zhang, U. Dorner, and I. A. Walmsley. Real-World Quantum Sensors: Evaluating Resources for Precision Measurement. *Phys. Rev. Lett.* **107**, 113603 (2011).

[47] H. Shin, O. S. Magaña-Loaiza, M. Malik, M. N. O'Sullivan, and R. W. Boyd. Enhancing entangled-state phase estimation by combining classical and quantum protocols. *Opt. Express* **21**, 2816–2822 (2013).

[48] O. S. Magana-Loaiza, B. Gao, S. A. Schulz, K. M. Awan, J. Upham, K. Dolgaleva, and R. W. Boyd. Enhanced spectral sensitivity of a chip-scale photonic-crystal slow-light interferometer. *Opt. Lett.* **41**, 1431–1434 (2016).

[49] B. L. Higgins, D. W. Berry, S. D. Bartlett, H. M. Wiseman, and P. G. J. Entanglement-free Heisenberg-limited phase estimation. *Nature* **450**, 393–396 (2007).

[50] L. H. Thomas. The Motion of the Spinning Electron. *Nature* **117**, 514–514 (1926).

[51] T. L. Gustavson, P. Bouyer, and M. A. Kasevich. Precision rotation measurements with an atom interferometer gyroscope. *Phys. Rev. Lett.* **78**, 2046 (1997).

[52] J. K. Stockton, K. Takase, and M. A. Kasevich. Absolute Geodetic Rotation Measurement Using Atom Interferometry. *Phys. Rev. Lett.* **107**, 133001 (2011).

[53] J. Courtial, D. A. Robertson, K. Dholakia, L. Allen, and M. J. Padgett. Rotational Frequency Shift of a Light Beam. *Phys. Rev. Lett.* **81**, 4828 (1998).

[54] M. P. J. Lavery, F. C. Speirits, S. M. Barnett, and M. J. Padgett. Detection of a Spinning Object Using Light's Orbital Angular Momentum. *Science* **341**, 537–540 (2013).

[55] V. D'Ambrosio, N. Spagnolo, L. Del Re, S. Slussarenko, Y. Li, L. C. Kwek, L. Marrucci, S. P. Walborn, L. Aolita, and F. Sciarrino. Photonic polarization gears for ultra-sensitive angular measurements. *Nature Communications* **4**, 1–8 (2013).

[56] R. Fickler, R. Lapkiewicz, W. N. Plick, M. Krenn, C. Schaeff, S. Ramelow, and A. Zeilinger. Quantum Entanglement of High Angular Momenta. *Science* **338**, 640–43 (2012).

[57] A. K. Jha, G. S. Agarwal, and R. W. Boyd. Supersensitive measurement of angular displacements using entangled photons. *Phys. Rev. A* **83**, 053829 (2011).

[58] N. Uribe-Patarroyo, A. Fraine, D. S. Simon, O. Minaeva, and A. V. Sergienko. Object Identification Using Correlated Orbital Angular Momentum States. *Phys. Rev. Lett.* **110**, 043601 (2013).

[59] Y. Gorodetski, K. Y. Bliokh, B. Stein, C. Genet, N. Shitrit, V. Kleiner, E. Hasman, and T. W. Ebbesen. Weak Measurements of Light Chirality with a Plasmonic Slit. *Phys. Rev. Lett.* **109**, 013901 (2012).

[60] H. Luo, S. Wen, W. Shu, Z. Tang, Y. Zou, and D. Fan. Rotational Doppler effect in left-handed materials. *Phys. Rev. A* **78**, 033805 (2008).

[61] S. Franke-Arnold, G. Gibson, R. W. Boyd, and M. J. Padgett. Rotary Photon Drag Enhanced by a Slow-Light Medium. *Science* **333**, 65–67 (2011).

[62] J. A. Davis, D. M. Cottrell, J. Campos, M. J. Yzuel, and I. Moreno. Encoding Amplitude Information onto Phase-Only Filters. *Appl. Opt.* **38**, 5004–5013 (1999).

[63] S. M. Hashemi Rafsanjani, M. Mirhosseini, O. S. Magana-Loaiza, and R. W. Boyd. State transfer based on classical nonseparability. *Phys. Rev. A* **92**, 023827 (2015).

[64] E. Nagali, F. Sciarrino, F. De Martini, L. Marrucci, B. Piccirillo, E. Karimi, and E. Santamato. Quantum Information Transfer from Spin to Orbital Angular Momentum of Photons. *Phys. Rev. Lett.* **103**, 013601 (2009).

[65] A. Mair, A. Vaziri, G. Weihs, and A. Zeilinger. Entanglement of the orbital angular momentum states of photons. *Nature* **412**, 313–316 (2001).

[66] J. Leach, M. J. Padgett, S. M. Barnett, S. Franke-Arnold, and J. Courtial. Measuring the orbital angular momentum of a single photon. *Phys. Rev. Lett.* **88**, 257901 (2002).

[67] G. C. G. Berkhout, M. P. J. Lavery, J. Courtial, M. W. Beijersbergen, and M. J. Padgett. Efficient Sorting of Orbital Angular Momentum States of Light. *Phys. Rev. Lett.* **105**, 153601 (2010).

[68] M. Mirhosseini, M. Malik, Z. Shi, and R. W. Boyd. Efficient separation of the orbital angular momentum eigenstates of light. *Nature Communications* **4**, 2781 (2013).

[69] R. Baraniuk. Compressive Sensing [Lecture Notes]. *IEEE Signal Process. Mag.* **24**, 118–121 (2007).

[70] E. J. Candès and M. B. Wakin. IEEE Xplore - An Introduction To Compressive Sampling. *Signal Processing Magazine* (2007).

[71] O. Katz, Y. Bromberg, and Y. Silberberg. Compressive ghost imaging. *Appl. Phys. Lett.* **95**, 131110–131110–3 (2009).

[72] P. Zerom, K. W. C. Chan, J. Howell, and R. Boyd. Entangled-photon compressive ghost imaging. *Phys. Rev. A* **84**, 061804 (2011).

[73] G. A. Howland and J. C. Howell. Phys. Rev. X 3, 011013 (2013): Efficient High-Dimensional Entanglement Imaging with a Compressive-Sensing Double-Pixel Camera. *Physical Review X* (2013).

[74] L. C. An efficient algorithm for total variation regularization with applications to the single pixel camera and compressive sensing. *Master thesis, Rice University* (2010).

[75] M. G. Raymer, M. Beck, and D. McAlister. Complex wave-field reconstruction using phase-space tomography. *Phys. Rev. Lett.* **72**, 1137 (1994).

[76] D. James, P. Kwiat, and A. White. Measurement of qubits. *Phys. Rev. A* **64**, 052312 (2001).

[77] G. Gibson, J. Courtial, M. Padgett, M. Vasnetsov, V. Pasko, B. Stephen, and S. Franke-Arnold. Free-space information transfer using light beams carrying orbital angular momentum. *Opt. Express* **12**, 5448–5456 (2004).

[78] M. Mirhosseini, O. S. Magana-Loaiza, M. N Oullivan, B. Rodenburg, M. Malik, M. Lavery, M. Padgett, D. Gauthier, and R. W. Boyd. High-dimensional quantum cryptography with twisted light. *New J. Phys.* **17**, 033033 (2015).

[79] V. Potocek, F. M. Miatto, M. Mirhosseini, O. S. Magana-Loaiza, A. C. Liapis, D. K. L. Oi, R. W. Boyd, and J. Jeffers. Quantum Hilbert Hotel. *Phys. Rev. Lett.* **155**, 160505 (2015).

[80] E. Wigner. On the Quantum Correction For Thermodynamic Equilibrium. *Phys. Rev.* **40**, 749 (1932).

[81] L. Cohen. Time-frequency distributions-a review. *Proc. IEEE* **77**, 941 (1989).

[82] M. A. Alonso. Wigner functions in optics: describing beams as ray bundles and pulses as particle ensembles. *Adv. Opt. Photonics* **3**, 272 (2011).

[83] C.-C. Cheng and M. Raymer. Propagation of transverse optical coherence in random multiple-scattering media. *Phys. Rev. A* **62**, 023811 (2000).

[84] C. Dorrer and I. Walmsley. Accuracy criterion for ultrashort pulse characterization techniques: application to spectral phase interferometry for direct electric field reconstruction. *JOSA B* **19**, 1019–1029 (2002).

[85] A. Lvovsky and M. Raymer. Continuous-variable optical quantum-state tomography. *Rev. Mod. Phys.* **81**, 299 (2009).

[86] R. Blume-Kohout. Optimal, reliable estimation of quantum states. *New J. Phys.* **12**, 043034 (2010).

[87] N. Bent, H. Qassim, A. Tahir, D. Sych, G. Leuchs, L. L. Sanchez-Soto, K. E, and B. RW. Experimental Realization of Quantum Tomography of Photonic Qudits via Symmetric Informationally Complete Positive Operator-Valued Measures. *Phys. Rev. X* **5**, 041006 (2015).

[88] H. Qassim, F. M. Miatto, J. P. Torres, P. Miles, E. Karimi, K. E, and B. RW. Limitations to the determination of a Laguerreauss spectrum via projective, phase-flattening measurement. *JOSA B* **31**, A20–A23 (2014).

[89] U. Leonhardt. Quantum-State Tomography and Discrete Wigner Function. *Phys. Rev. Lett.* **74**, 4101 (1995).

[90] C. Borges, A. Khoury, S. Walborn, P. Ribeiro, P. Milman, and K. A. Bell inequalities with continuous angular variables. *Phys. Rev. A* **86**, 052107 (2012).

[91] P. L. Knight. The observation of matter wave fluctuations. *Science* **310**, 631–632 (2005).

[92] S. Oppel, R. Wiegner, G. S. Agarwal, and J. von Zanthier. Directional Superradiant Emission from Statistically Independent Incoherent Nonclassical and Classical Sources. *Phys. Rev. Lett.* **113**, 263606 (2014).

[93] Y. Bromberg, Y. Lahini, E. Small, and Y. Silberberg. Hanbury Brown and Twiss interferometry with interacting photons. *Nature Photonics* **4**, 1–6 (2010).

[94] G. Baym. The Physics of Hanbury Brown-Twiss intensity interferometry: From stars to nuclear collisions. *Acta. Phys. Pol. B* **B29**, 1839–1884 (1998).

[95] M. Schellekens, R. Hopperler, A. Perrin, J. Viana Gomes, D. Boiron, A. Aspect, and W. CI. Hanbury Brown Twiss effect for ultracold quantum gases. *Science* **310**, 648–651 (2005).

[96] J. W. Pan, Z. B. Chen, C. Y. Lu, H. Weinfurter, and A. Zeilinger. Rev. Mod. Phys. 84, 777 (2012) - Multiphoton entanglement and interferometry. *Reviews of Modern Physics* **84**, 777 (2012).

[97] J. Leach, B. Jack, J. Romero, A. K. Jha, A. M. Yao, S. Franke-Arnold, D. G. Ireland, R. W. Boyd, S. M. Barnett, and M. J. Padgett. Quantum Correlations in Optical Angle-Orbital Angular Momentum Variables. *Science* **329**, 662–665 (2010).

[98] H. De Raedt, A. Lagendijk, and P. de Vries. Transverse Localization of Light. *Phys. Rev. Lett.* **62**, 68 (1989).

[99] J. Romero, J. Leach, B. Jack, M. R. Dennis, S. Franke-Arnold, S. M. Barnett, and M. J. Padgett. Entangled Optical Vortex Links. *Phys. Rev. Lett.* **106**, 100407 (2011).

[100] J. Xiong, D.-Z. Cao, F. Huang, H.-G. Li, X.-J. Sun, and K. Wang. Experimental Observation of Classical Subwavelength Interference with a Pseudothermal Light Source. *Phys. Rev. Lett.* **94**, 173601 (2005).

[101] A. Gatti, E. Brambilla, M. Bache, and L. Lugiato. Ghost Imaging with Thermal Light: Comparing Entanglement and ClassicalCorrelation. *Phys. Rev. Lett.* **93**, 093602 (2004).

[102] A. Nevet, A. Hayat, P. Ginzburg, and M. Orenstein. Indistinguishable Photon Pairs from Independent True Chaotic Sources. *Phys. Rev. Lett.* **107**, 253601 (2011).

[103] S.-H. Zhang, L. Gao, J. Xiong, L.-J. Feng, D.-Z. Cao, and K. Wang. Spatial Interference: From Coherent to Incoherent. *Phys. Rev. Lett.* **102**, 073904 (2009).

[104] B. Redding, M. A. Choma, and H. Cao. Speckle-free laser imaging using random laser illumination. *Nature Photonics* **6**, 355–359 (2012).

[105] M. V. Berry. Disruption of wavefronts: statistics of dislocations in incoherent Gaussian random waves. *J. Phys. A: Math. Gen.* **11**, 27–37 (1978).

[106] M. R. Dennis, K. O'Holleran, and M. J. Padgett. *Chapter 5 Singular Optics: Optical Vortices and Polarization Singularities*, vol. 53. Elsevier B.V. (2009).

[107] A. M. Yao and M. J. Padgett. Optics InfoBase: Advances in Optics and Photonics - Orbital angular momentum: origins, behavior and applications. *Adv. Opt. Photon.* **3**, 161 (2011).

[108] F. Tamburini, B. Thidé, G. Molina-Terriza, and G. Anzolin. Twisting of light around rotating black holes . *Nature Physics* **7**, 196 (2011).

[109] G. Foo, D. M. Palacios, and G. A. Swartzlander, Jr. Optical vortex coronagraph. *Opt. Lett.* **30**, 3308–3310 (2005).

[110] C. M. Harding, R. A. Johnston, and R. G. Lane. Fast simulation of a kolmogorov phase screen. *Appl. Opt.* **38**, 2161 (1999).

[111] M. Mirhosseini, O. S. Magaña-Loaiza, C. Chen, B. Rodenburg, M. Malik, and R. W. Boyd. Rapid Generation of Light Beams Carrying Orbital Angular Momentum. *Opt. Express* **21**, 30204 (2013).

[112] F. T. Arecchi. Measurement of the statistical distribution of Gaussian and laser sources. *Phys. Rev. Lett.* **15**, 912 (1965).

[113] A. Glindemann, R. G. Lane, and J. C. Dainty. Simulation of Time-evolving Speckle Patterns Using Kolmogorov Statistics. *Journal of Modern Optics* **40**, 2381–2388 (1993).

[114] R. Hanbury Brown and R. Q. Twiss. Interferometry of the intensity fluctuations in light. II. An experimental test of the theory for partially coherent light. *Proc. R. Soc. A* **243**, 291–319 (1958).

[115] B. Jack, J. Leach, J. Romero, S. Franke-Arnold, R.-M. M, and P. M. J. Holographic Ghost Imaging and the Violation of a Bell Inequality. *Phys. Rev. Lett.* **103**, 083602 (2009).

[116] L. Chen, J. Lei, and J. Romero. Quantum digital spiral imaging. *Light Sci. Appl.* **3**, 153 (2014).

[117] C. Paterson. Atmospheric Turbulence and Orbital Angular Momentum of Single Photons for Optical Communication. *Phys. Rev. Lett.* **94**, 153901 (2005).

[118] G. Gbur and T. D. Visser. Coherence vortices in partially coherent beams. *Optics Communications* **222**, 117 (2003).

[119] A. Kumar, J. Banerji, and R. P. Singh. Hanbury Brown-Twiss-type experiments and observation of modulated intensity correlation on scattering from rotating ground glass. *Phys. Rev. A* **86**, 013825 (2012).

[120] M. R. Dennis, R. P. King, B. Jack, K. O'Holleran, and M. J. Padgett. Isolated optical vortex knots. *Nature Physics* **6**, 118–121 (2010).

[121] D. Hetharia, M. P. van Exter, and W. Löffler. Spatial Coherence and the orbital angular momentum of light in Astronomy. *Phys. Rev. A* **90** (2014).

[122] M. Born and E. Wolf. Principles of Optics. *Cambridge Univ. Press, Cambrisge* 986 (1999).

[123] P. B. Dixon, G. A. Howland, K. Chan, and C. O'Sullivan-Hale. Quantum ghost imaging through turbulence. *Phys. Rev. A* **83**, 051803 (2011).

[124] W.-K. Yu, X.-F. Liu, X.-R. Yao, C. Wang, S.-Q. Gao, G.-J. Zhai, Q. Zhao, and M.-L. Ge. Single photon counting imaging system via compressive sensing. *arXiv* **physics.optics** (2012).

[125] G. A. Howland, P. B. Dixon, and J. C. Howell. Photon-counting compressive sensing laser radar for 3D imaging. *Appl. Opt.* **50**, 5917–5920 (2011).

[126] T. Pittman, Y. Shih, D. Strekalov, and A. Sergienko. Optical imaging by means of two-photon quantum entanglement. *Phys. Rev. A* **52**, R3429–R3432 (1995).

[127] P. Clemente, V. Durán, V. Torres-Company, E. Tajahuerce, and J. Lancis. Optical encryption based on computational ghost imaging. *Opt. Lett.* **35**, 2391 (2010).

[128] S. Karmakar and Y. Shih. Two-color ghost imaging with enhanced angular resolving power. *Phys. Rev. A* **81**, 033845 (2010).

[129] M. Malik, H. Shin, M. O'Sullivan, P. Zerom, and R. W. Boyd. Quantum Ghost Image Identification with Correlated Photon Pairs. *Phys. Rev. Lett.* **104**, 163602 (2010).

[130] W. Gong, C. Zhao, J. Jiao, E. Li, M. Chen, H. Wang, W. Xu, and S. Han. Three-dimensional ghost imaging ladar. *arXiv* **quant-ph** (2013).

[131] J. L. O'Brien, A. Furusawa, and J. Vučković. Photonic quantum technologies. *Nature Photonics* **3**, 687–695 (2009).

[132] C. E. Shannon. Communication in the Presence of Noise. *Proc. IRE* **37**, 10–21 (1949).

[133] R. Bennink, S. Bentley, and R. Boyd. "Two-Photon" Coincidence Imaging with a Classical Source. *Phys. Rev. Lett.* **89**, 113601 (2002).

[134] M. Malik, H. Shin, and R. W. Boyd. Optics InfoBase - Quantum Ghost Image Tracking. *Laser Science* (2011).

[135] C. Monken, P. Ribeiro, and S. Pádua. Transfer of angular spectrum and image formation in spontaneous parametric down-conversion. *Phys. Rev. A* **57**, 3123–3126 (1998).

[136] R. F. Marcia and J. M. Nichols. SPIE | Optical Engineering | Compressed sensing for practical optical imaging systems: a tutorial. *... Engineering* (2011).

[137] S. Nakadate, T. Yatagai, and H. Saito. Optics InfoBase: Applied Optics - Electronic speckle pattern interferometry using digital image processing techniques. *Appl. Opt.* (1980).

[138] Y. H. Kim, R. Yu, S. P. Kulik, Y. Shih, and M. O. Scully. Delayed "Choice" Quantum Eraser. *Phys. Rev. Lett.* **84**, 0031–9007 (1999).

[139] H. F. Schouten, N. Kuzmin, G. Dubois, T. D. Visser, G. Gbur, P. F. A. Alkemade, H. Blok, G. W. t. Hooft, D. Lenstra, and E. R. Eliel. Plasmon-Assisted Two-Slit Transmission: Young's Experiment Revisited. *Phys. Rev. Lett.* **94**, 053901 (2005).

[140] R. Menzel, D. Puhlmann, A. Heuer, and W. P. Schleich. Wave-particle dualism and complementarity unraveled by a different mode. *PNAS* **109**, 9314–9319 (2012).

[141] E. Bolduc, J. Leach, F. M. Miatto, G. Leuchs, and R. W. Boyd. A "fair sampling" perspective on an apparent violation of duality. *PNAS* **111**, 12337 (2014).

[142] R. D. Sorkin. Quantum Mechanics as Quantum Measure Theory. *Mod. Phys. Lett. A* **09**, 3119–3127. doi:10.1142/S021773239400294X (1994).

[143] U. Sinha, C. Couteau, T. Jennewein, R. Laflamme, and G. Weihs. Ruling Out Multi-Order Interference in Quantum Mechanics. *Science* **329**, 418–421 (2010).

[144] H. De Raedt and K. Hess. Analysis of multipath interference in three-slit experiments. *Phys. Rev. A* **85**, 012101 (2012).

[145] R. Sawant, J. Samuel, A. Sinha, S. Sinha, and U. Sinha. Nonclassical Paths in Quantum Interference Experiments. *Phys. Rev. Lett.* **113**, 120406 (2014).

[146] A. Sinha, A. H Vijay, and U. Sinha. On the superposition principle in interference experiments. *Scientific Reports* **5**, 10304 (2015).

[147] J. W. Goodman. *Introduction to Fourier Optics*. McGraw-Hill, New York (1968).

[148] R. P. Feynman and A. R. Hibbs. *Quantum Mechanics and Path Integrals*. McGraw-Hill, New York, 3rd ed. ed. (1965).

[149] M. W. Kowarz. Homogeneous and evanescent contributions in scalar near-field diffraction. *Appl. Opt.* **34**, 3055. doi:10.1364/AO.34.003055 (1995).

[150] H. Raether. *Surface Plasmons on Smooth and Rough Surfaces and on Gratings*. Springer, Berlin (1988).

[151] W. L. Barnes, A. Dereux, and T. W. Ebbesen. Surface plasmon subwavelength optics. *Nature* **424**, 824 (2003).

[152] G. Gay, O. Alloschery, B. Viaris de Lesegno, C. O'Dwyer, J. Weiner, and H. J. Lezec. The optical response of nanostructured surfaces and the composite diffracted evanescent wave model. *Nat. Phys.* **2**, 262–267. doi:10.1038/nphys264 (2006).

[153] H. F. Schouten, N. Kuzmin, G. Dubois, T. D. Visser, G. Gbur, P. F. A. Alkemade, H. Blok, G. W. t. Hooft, D. Lenstra, and E. R. Eliel. Plasmon-Assisted Two-Slit Transmission: Young's Experiment Revisited. *Phys. Rev. Lett.* **94**, 053901. doi:10.1103/PhysRevLett.94.053901 (2005).

[154] E. D. Palik. *Handbook of Optical Constants of Solids.* Academic Press, New York (1985).

[155] P. Johnson and R. Christy. Optical constants of the noble metals. *Phys. Rev. B* **6**, 4370–4379 (1972).

Appendix

Appendix A

Amplification of Rotations Using Weak Values

The main purpose of this document is to provide more detailed information about the design of our experimental setup and recast its functionality in terms of the "weak measurement" formalism. In addition, we describe the scheme employed to measure the OAM spectrum of a beam of light.

Sagnac interferometer

We use a Sagnac interferometer composed of a polarized beam splitter (PBS), a Dove prism (DP) and a series of rotatable plates. In this first section, we will describe the role of the DP and how we use the rotatable plates to introduce geometric phases.

As mentioned in the article, a spatial mode $|f(\phi)\rangle$ is diagonally polarized and injected into the input port of the interferometer, and the polarization information is

described by the state $|\Psi_{pr}\rangle$. Therefore we can describe the initial state as $|f(\phi)\rangle\,|\Psi_{pr}\rangle$. The beam is split into two polarization components that circulate in opposite directions within the interferometer. The role of the DP is to rotate the beam. When the DP is rotated by an angle of $\Delta\phi/4$ about its optical axis, the transmitted beam suffers a rotation of $\pm\Delta\phi/2$, where the sign is determined by the propagation direction of the beam. In our experiment, the DP couples the polarization degree of freedom (DoF) to the spatial DoF of the beam. The action of the DP inside the polarized Sagnac interferometer is described as follows:

$$\begin{aligned} |\Psi_{pr}\rangle\,|f(\phi)\rangle \xrightarrow[Prism]{Dove} \quad & \tfrac{1}{\sqrt{2}}(\mathbf{R}(-\phi/2)\,|f(\phi)\rangle\,|H\rangle + \mathbf{R}(\phi/2)\,|f(\phi)\rangle\,|V\rangle) \\ & = \tfrac{1}{\sqrt{2}}\,|f(\phi-\Delta\phi/2)\rangle\,|H\rangle + |f(\phi+\Delta\phi/2)\rangle\,|V\rangle), \end{aligned} \tag{A.1}$$

where the operator $\mathbf{R}(\phi/2)$ is given by $e^{i\hat{\ell}\Delta\phi/2}$. $\hat{\ell}$ is the generator of rotations and is proportional to the operator representing angular momentum along the optical axis.

The role of the wave plates is to induce a geometric phase, which we will describe using the Jones matrix formalism. Here the polarization states are defined as:

$$|H\rangle = \begin{bmatrix} 1 \\ 0 \end{bmatrix} \text{ and } |V\rangle = \begin{bmatrix} 0 \\ 1 \end{bmatrix}. \tag{A.2}$$

The action of the quarter-wave plate **QWP** and half-wave plate **HWP** are described by the following matrices,

$$\mathbf{QWP} = \begin{bmatrix} e^{i\phi_{x1}}\cos^2(\theta_Q) + e^{i\phi_{y1}}\sin^2(\theta_Q) & (e^{i\phi_{x1}} - e^{i\phi_{y1}})\cos(\theta_Q)\sin(\theta_Q) \\ (e^{i\phi_{x1}} - e^{i\phi_{y1}})\cos(\theta_Q)\sin(\theta_Q) & e^{i\phi_{x1}}\sin^2(\theta_Q) + e^{i\phi_{y1}}\cos^2(\theta_Q) \end{bmatrix}, \tag{A.3}$$

and

$$\mathbf{HWP} = \begin{bmatrix} \cos(2\theta_H) & \sin(2\theta_H) \\ \sin(2\theta_H) & -\cos(2\theta_H) \end{bmatrix}. \tag{A.4}$$

θ_Q represents the orientation of the fast axis of the QWP, with respect to the x-axis, and θ_H represents the orientation of the HWP. The value $\phi_y - \phi_x$ determines the induced retardation phase between the two components of the electric field. For a QWP this number is equal to $\pi/2$.

The configuration used to induce the geometric phase consists of a HWP sandwiched between two QWPs. The angle θ_Q was set to $\pi/4$ whereas the angle of the HWP, θ_H, was set to $\theta_H/4$. Thus the Eqs. (A.3)–(A.4) become

$$\mathbf{QWP}_{\pm} = \begin{bmatrix} \frac{1}{2} + \frac{i}{2} & \pm(\frac{1}{2} - \frac{i}{2}) \\ \pm(\frac{1}{2} - \frac{i}{2}) & \frac{1}{2} + \frac{i}{2} \end{bmatrix}, \tag{A.5}$$

and

$$\mathbf{HWP}_{\pm} = \begin{bmatrix} \cos(\theta_H/2) & \pm\sin(\theta_H/2) \\ \pm\sin(\theta_H/2) & -\cos(\theta_H/2) \end{bmatrix}. \tag{A.6}$$

Different orientation angles have to be considered for each of the counter-propagating beams. Here we use positive and negative values for the horizontally and negative

polarized beams respectively. The transformation suffered by each beam is thus given by

$$\begin{aligned} |H^g\rangle &= \mathbf{QWP}_+ \cdot \mathbf{HWP}_+ \cdot \mathbf{QWP}_+ |H\rangle \\ &= e^{-i(\theta_H/2-\pi/2)} |H\rangle , \end{aligned} \tag{A.7}$$

and

$$\begin{aligned} |V^g\rangle &= \mathbf{QWP}_- \cdot \mathbf{HWP}_- \cdot \mathbf{QWP}_- |V\rangle \\ &= e^{i(\theta_H/2-\pi/2)} |V\rangle . \end{aligned} \tag{A.8}$$

As can be seen, the net effect is the acquisition of a phase given by $\pm(\theta_H/2 - \pi/2)$, which is the geometric phase.

The action of sagnac interferometer in terms of the weak measurement formalism

In this section we describe our weak measurement protocol. The action of the interferometer is described by the following interaction Hamiltonian:

$$\hat{H}_T = \hat{H}_g + \hat{H}_{SO}. \tag{A.9}$$

The Hamiltonian $\hat{H}_g$ describes the role of the three wave plates. It is given by $\delta\hat{\sigma}$. The spin-orbit interaction caused by the DP is described by $\hat{H}_{SO}$, which is given by a Hamiltonian of the form $\mu\hat{\sigma}\hat{\ell}$, where $\hat{\sigma}$ is the Pauli operator defined as $|H\rangle\langle H| - |V\rangle\langle V|$, $(\theta_H/2 - \pi/2) = \delta\Delta t$ and $\Delta\phi/2 = \mu\Delta t$. Given this, the evolution of the initial state $|\Psi_i\rangle = |\Psi_{pr}\rangle|f(\phi)\rangle$ to a final state $|\Psi_f\rangle$ is given as

$$\begin{aligned} |\Psi_f\rangle &= e^{-i\hat{H}_T\Delta t}|\Psi_{pr}\rangle|f(\phi)\rangle \\ &= e^{-i\hat{H}_g\Delta t}\Bigg[\frac{1}{\sqrt{2}}(|H\rangle + |V\rangle)|f(\phi)\rangle \\ &\quad - i\frac{\Delta\phi}{2\sqrt{2}}(|H\rangle\langle H| - |V\rangle\langle V|)(|H\rangle + |V\rangle)\hat{\ell}|f(\phi)\rangle + \dots\Bigg], \end{aligned} \tag{A.10}$$

This expression can be rewritten as

$$\begin{aligned} &|\Psi_f\rangle = \\ &\quad \tfrac{e^{-i\hat{H}_g\Delta t}}{\sqrt{2}}\left[|H\rangle(1 - i\tfrac{\Delta\phi}{2}\hat{\ell} + ...)|f(\phi)\rangle + |V\rangle(1 + i\tfrac{\Delta\phi}{2}\hat{\ell} + ...)|f(\phi)\rangle\right]. \end{aligned} \tag{A.11}$$

The expression in parenthesis is a translation operator in the azimuthal degree of freedom which leads to the state

$$|\Psi_f\rangle = \frac{e^{-i\hat{H}_g\Delta t}}{\sqrt{2}}[|H\rangle|f(\phi - \Delta\phi/2)\rangle + |V\rangle|f(\phi + \Delta\phi/2)\rangle]. \tag{A.12}$$

The action of $\hat{H}_g$ leads to the state

$$\begin{aligned} |\Psi_f\rangle = \frac{1}{\sqrt{2}}[&e^{-i(\theta_H/2-\pi/2)}\,|H\rangle\,|f(\phi-\Delta\phi/2)\rangle \\ &+ e^{i(\theta_H/2-\pi/2)}\,|V\rangle\,|f(\phi+\Delta\phi/2)\rangle]. \end{aligned} \tag{A.13}$$

The state above describes our experiment just before post-selection by the polarizer is performed. $\left|\Psi_f\right\rangle$ is the state of the photons emerging from the output port of the polarized beam splitter. The post-selection process is described by the projection operator $|\Phi_{ps}\rangle\langle\Phi_{ps}|$ which gives the post-selected state

$$\begin{aligned} |\Psi_p\rangle &= |\Phi_{ps}\rangle\langle\Phi_{ps}|\,|\Psi_f\rangle \\ &= [\langle\Phi_{ps}|\,e^{-i\hat{H}_g\Delta t}\,|\Psi_{pr}\rangle\,|f(\phi)\rangle \\ &\quad - i\frac{\Delta\phi}{2}\,\langle\Phi_{ps}|\,e^{-i\hat{H}_g\Delta t}\hat{\sigma}\,|\Psi_{pr}\rangle\,\hat{\ell}\,|f(\phi)\rangle + ...]\,|\Phi_{ps}\rangle\,. \end{aligned} \tag{A.14}$$

This expression can be approximated to the first order and then normalized:

$$|\Psi_p\rangle \approx \left(|f(\phi)\rangle - i\frac{\Delta\phi}{2}\frac{\langle\Phi_{ps}|\,e^{-i\hat{H}_g\Delta t}\hat{\sigma}\,|\Psi_{pr}\rangle}{\langle\Phi_{ps}|\,e^{-i\hat{H}_g\Delta t}\,|\Psi_{pr}\rangle}\hat{\ell}\,|f(\phi)\rangle\right)|\Phi_{ps}\rangle \tag{A.15}$$

Since $\hat{\sigma}$ commutes with $e^{-i\hat{H}_g\Delta t}$

$$|\Psi_p\rangle = \left(|f(\phi)\rangle - i\frac{\Delta\phi}{2}\frac{\langle\Phi_{ps}|\,\hat{\sigma}\,|\Psi_{fpr}\rangle}{\langle\Phi_{ps}|\Psi_{fpr}\rangle}\hat{\ell}\,|f(\phi)\rangle\right)|\Phi_{ps}\rangle\,, \tag{A.16}$$

where $\left|\Psi_{fpr}\right\rangle \equiv e^{-i\hat{H}_g \Delta t} \left|\Psi_{pr}\right\rangle$. Defining the weak value of $\hat{\sigma}$ as

$$\sigma_w \equiv \frac{\left\langle \Phi_{ps}\right| \hat{\sigma} \left|\Psi_{fpr}\right\rangle}{\left\langle \Phi_{ps}|\Psi_{fpr}\right\rangle}, \tag{A.17}$$

then the total effect of the post-selection can be written as

$$\left|\Psi_p\right\rangle = \left|f(\phi - \sigma_w \Delta\phi/2)\right\rangle \left|\Phi_{ps}\right\rangle . \tag{A.18}$$

The weak value of the polarization operator can be determined by using the following form for the states:

$$\begin{aligned} \left|\Psi_{fpr}\right\rangle &= \frac{1}{\sqrt{2}} \left(e^{-i(\theta_H/2 - \pi/2)} \left|H\right\rangle + e^{i(\theta_H/2 - \pi/2)} \left|V\right\rangle\right) \\ \left|\Phi_{ps}\right\rangle &= \sin\left(\gamma/2 - \pi/4\right) \left|H\right\rangle + \cos\left(\gamma/2 - \pi/4\right) \left|V\right\rangle . \end{aligned} \tag{A.19}$$

It is worth noting that $\left|\Phi_{ps}\right\rangle$ is almost orthogonal with respect to $\left|\Psi_{pr}\right\rangle$. Using the above states the weak value becomes

$$\sigma_w = \frac{\tan\left(\gamma/2 - \pi/4\right) e^{-i(\theta_H - \pi)} - 1}{\tan\left(\gamma/2 - \pi/4\right) e^{-i(\theta_H - \pi)} + 1}. \tag{A.20}$$

For simplicity we can define the angle $\theta_H - \pi$ as θ. If we assume that $\gamma/2$ and θ are very small, corresponding to the weak measurement regime, then this expression

becomes

$$\begin{aligned}\sigma_w &= \frac{e^{-i\theta\frac{\tan(\gamma/2)-\tan(\pi/4)}{1+\tan(\gamma/2)\tan(\pi/4)}}-1}{e^{-i\theta\frac{\tan(\gamma/2)-\tan(\pi/4)}{1+\tan(\gamma/2)\tan(\pi/4)}}+1} \\ &\approx \frac{(1-i\theta)\frac{\gamma-2}{2+\gamma}-1}{(1-i\theta)\frac{\gamma-2}{2+\gamma}+1} \\ &= \frac{\gamma-2-i\theta\gamma+2i\theta-\gamma-2}{\gamma-2-\theta\gamma+2i\theta+\gamma+2} \\ &\approx \frac{-2}{\gamma+i\theta} = -2\frac{\gamma}{\gamma^2+\theta^2}+2\frac{i\theta}{\gamma^2+\theta^2}.\end{aligned} \tag{A.21}$$

Projective measurements

In this section we describe a simple form of measuring the OAM power spectrum of an ensemble of photons. The technique employed is known as projection measurements. Here a spatial mode (in our case an angular mode $f(\mathbf{r})$), which can be written in terms of the modal expansion $\sum_\ell a_\ell e^{i\ell\phi}$, is imaged onto a SLM that transforms the field in the first diffracted order to:

$$f(\mathbf{r})e^{-i\ell\phi}. \tag{A.22}$$

A Fourier transforming lens takes the field above to

$$f_\ell(\boldsymbol{\rho}) = F[f(\mathbf{r})e^{-i\ell\phi}], \tag{A.23}$$

which is spatially filtered using a SMF coupled to an avalanche photodiode (APD) which allows measurement at single photon levels. The coupling efficiency into the fiber, η_ℓ is given by

$$\eta_\ell \propto \left| \int f_\ell(\boldsymbol{\rho}) e^{-\frac{\rho^2}{2\eta^2}} \, \mathrm{d}^2\boldsymbol{\rho} \right|^2, \tag{A.24}$$

where η is the Gaussian width of the fiber mode. Assuming features of f_ℓ to be of size scale larger than η, this filtering function becomes

$$\eta_\ell \approx \left| \int f_\ell(0) e^{-\frac{\rho^2}{2\eta^2}} \, \mathrm{d}^2\boldsymbol{\rho} \right|^2 \propto |f_\ell(0)|^2 = \left| \sum_{\ell'} \int a_{\ell} e^{i(\ell'-\ell)\phi} \mathrm{d}^2\mathbf{r} \right|^2 = |a_\ell|^2 , \tag{A.25}$$

permitting us to obtain the OAM power spectrum component $|a_\ell|^2$. This process is repeated for the different modes contained in the spatial mode. The efficiency of this technique for different spatial modes, such as radial modes, has been studied in reference [88].

Appendix B

HBT Interferometry with Twisted Light

Source of Pseudothermal light.

Pseudothermal light was generated by means of phase screen holograms obeying Kolmogorov statistics. Kolmogorov's statistical theory is used to model chaotic turbulent fluids. We have generated Kolmogorov phase screens for varying levels of simulated randomness by using the approximate power spectral density of $\Phi(f) \approx 0.023 r_0^{-5/3} f^{-11/3}$. Fried's parameter r_0 is related to the average coherence length between two points in the beam. By adjusting Fried's parameter r_0, we can increase or decrease the size of and the distance between the phase cells and thus the amount of randomness in the phase screens. By adding normally distributed deviations to the power spectral density, we can then take the real part of the inverse Fourier transform in order to generate a single Kolmogorov phase screen.

A DMD can be used to manipulate both the phase and amplitude profile of a light beam. A translation in a binary diffraction grating will cause a phase shift to occur in the diffracted light, whereas varying the duty cycle of the periodic grating will change the efficiency, and thus the amplitude, of the diffracted beam. Both of these techniques can be done locally to spatially control the phase and amplitude of the beam. The generated Kolmogorov screens were then converted into binary diffraction gratings to be displayed on a DMD.

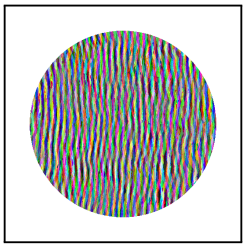

Figure B.1: Example of a frame sent to the DMD. It contains 24 binary holograms encoded in bit plane slices.

We used the Texas Instruments LightCrafter Evaluation Module (DLPC300) which drives a Texas Instruments DLP3000 DMD. The DMD contains an array of 608×684 micromirrors with a total diagonal length of 7.62 mm. The DMD was operated in a mode that allowed a binary pattern to be displayed at a rate of 1440 Hz. The DMD takes a 24-bit color 60 Hz signal over an HDMI connection. Because the image contains 24 bits, a single video frame can contain 24 binary images. In this mode, the DMD will cycle through the least significant bit to the most significant bit in the blue signal of a frame. Then, the DMD will display the bits in the red signal and, finally, the green signal. Kolmogorov screens (72,000) were encoded into three thousand 24-bit

frames for each value of Fried's parameter $r_0 = 70$ μm, 150 μm and 210 μm. Figure B.1 shows an example of one of the generated frames sent to the DMD. This frame contains 24 binary holograms encoded in the bit planes of the image to be displayed sequentially.

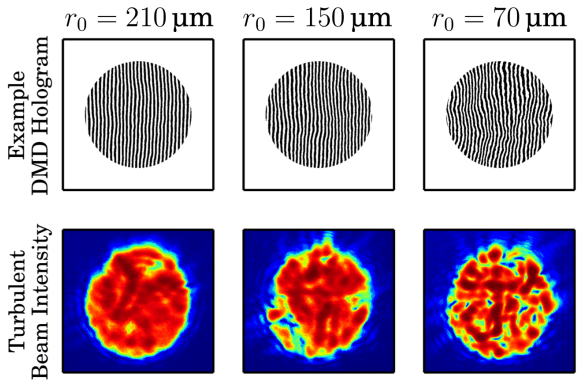

Figure B.2: Example DMD holograms and resulting beams measured before the image plane.

Figure B.2 shows examples of the intensity distribution for three random beams generated by this method. In addition, in each case, an example of one of the holograms used to produce the beam is shown. Note that the randomness within the beam increases as the value of r_0 decreases.

The HBT effect for symmetrically displaced modes (ℓ and $-\ell$).

Here, we derive the equations utilized in the manuscript. We start by describing HBT interference of pseudothermal light. We assume that the beam of light from our

laser is described by the electric field $\mathcal{E}(r)$, where r is the radial coordinate in the transverse plane. In addition, we assume that the initial electric field does not possess any azimuthal dependence. We encode a random Kolmogorov phase screen $\Phi(r, \phi)$ onto the beam. Later, the field illuminates two angular apertures centered on angles 0 and ϕ_0. Thus the field after the two slits is given by

$$\Psi(r, \phi) = \mathcal{E}(r)\Phi(r, \phi)[A(\phi) + A(\phi - \phi_0)].\cdot \tag{B.1}$$

As described earlier in the manuscript, we replace the widely used ground-glass plate with a series of phase screens that change rapidly in comparison to the accumulation time of the measurement, thus creating an ensemble of field realizations. The next step is to find the intensity of the field for a given OAM eigenstate. We can write the electric field after the two slits as a linear combination of radial-OAM modes. We designate a complete radial basis as $R_p(r)$, although we do not make use of any explicit form for this basis. We thereby express the field after the slits as

$$\Psi(r, \phi) = \sum_{\ell,p} a_{p\ell} R_p(r) \frac{e^{i\ell\phi}}{\sqrt{2\pi}}, \tag{B.2}$$

where the expansion coefficients $a_{p\ell}$ are given by

$$a_{p\ell} = \int r dr d\phi R_p^*(r) \frac{e^{-i\ell\phi}}{\sqrt{2\pi}} \Psi(r, \phi). \tag{B.3}$$

Thus, the measured intensity after projecting the beam onto OAM mode ℓ is given by

$$\begin{aligned} I_\ell &= \sum_p |a_{p\ell}|^2 = \sum_p \int r_1 dr_1 r_2 dr_2 d\phi_1 d\phi_2 \Psi^*(r_1,\phi_1) R_p(r_1) \frac{e^{i\ell\phi_1}}{\sqrt{2\pi}} \frac{e^{-i\ell\phi_2}}{\sqrt{2\pi}} R_p^*(r_2) \Psi(r_2,\phi_2) \\ &= \int r_1 dr_1 r_2 dr_2 d\phi_1 d\phi_2 \Psi^*(r_1,\phi_1)\Psi(r_2,\phi_2) \frac{e^{i\ell(\phi_1-\phi_2)}}{2\pi} \sum_p R_p(r_1) R_p^*(r_2) \\ &= \frac{1}{2\pi} \int r dr d\phi_1 d\phi_2 \Psi^*(r,\phi_1)\Psi(r,\phi_2) e^{i\ell(\phi_1-\phi_2)}, \end{aligned} \tag{B.4}$$

where the last form comes from using the relation $\sum_p R_p(r_1) R_p^*(r_2) = (1/r_1)\delta(r_1 - r_2)$, which is true for any complete normalized set of basis functions, where $\delta(r)$ is the usual Dirac delta function. Now we replace $\Psi(r,\phi)$ with the electric field after the two angular slits given by Eq.1. For simplicity, we first approximate $A(\phi)$ by $\delta(\phi)$ and $A(\phi - \phi_0)$ by $\delta(\phi - \phi_0)$. The quantity I_ℓ then becomes

$$I_\ell = \frac{1}{2\pi} \int r dr |\mathcal{E}(r)|^2 \left\{ 2 + e^{-i\ell\phi_0} \Phi^*(r,0)\Phi(r,\phi_0) + e^{i\ell\phi_0} \Phi^*(r,\phi_0)\Phi(r,0) \right\}. \tag{B.5}$$

We next take the ensemble average to obtain

$$\langle I_\ell \rangle = \frac{1}{2\pi} \int r dr |\mathcal{E}(r)|^2 \left\{ 2 + e^{-i\ell\phi_0} \langle \Phi^*(r,0)\Phi(r,\phi_0) \rangle + e^{i\ell\phi_0} \langle \Phi^*(r,\phi_0)\Phi(r,0) \rangle \right\}. \tag{B.6}$$

In reality, however, the finite size of the slits produces an envelope, caused by diffraction, that modulates the form of the interference pattern. If a slit with a width α is considered, the interference pattern can be easily calculated to be $\int_{-\pi}^{\pi} d\phi f(\phi) e^{-i\phi\ell}$,

where in our case $f(\phi)$ is equal to 1 in the range from $-\alpha/2$ to $\alpha/2$ and is equal to 0 otherwise. This integral produces a diffraction envelope given by $\frac{\alpha}{2\pi}\text{sinc}\left(\frac{\ell\alpha}{2}\right)$. The diffraction produced by the second slit can likewise be described as $\frac{\alpha}{2\pi}\text{sinc}\left(\frac{\ell\alpha}{2}\right)e^{-i\ell\phi_0}$. The intensity of the total diffraction is described as $\left(\frac{\alpha}{\pi}\right)^2\text{sinc}^2\left(\frac{\ell\alpha}{2}\right)(1+\cos(\ell\phi_0))$. Taking this result into account, we find that the first-order-interference diffraction pattern is given not by Eq. B.6. but rather by

$$\langle I_\ell\rangle = \frac{\alpha^2\text{sinc}^2(\ell\alpha/2)}{2\pi^2}\int rdr\mathcal{E}^2(r)\left\{2+e^{-i\ell\phi_0}\langle\Phi^*(r,0)\Phi(r,\phi_0)\rangle+e^{i\ell\phi_0}\langle\Phi^*(r,\phi_0)\Phi(r,0)\rangle\right\}. \tag{B.7}$$

We next develop appropriate approximations for the quantities defined above. A reasonable assumption is that the field fluctuations follow Gaussian statistics such that

$$\langle\Phi^*(r_1,0)\Phi(r_2,\phi_0)\rangle = \exp\left(-\frac{r_1^2+r_2^2-2r_1r_2\cos\phi_0}{r_0^2}\right). \tag{B.8}$$

By setting r_1 equal to r_2, we find that

$$\langle\Phi^*(r,0)\Phi(r,\phi_0)\rangle = \exp\left(-\frac{4r^2|\sin\frac{\phi_0}{2}|^2}{r_0^2}\right) = \exp(-\beta r^2). \tag{B.9}$$

The last form of this expression defines the quantity β. For a fully coherent beam, (that is, for $r_0 \gg r$, where r_0 is the Fried parameter introduced in Section 3) we see that to very high accuracy $\langle\Phi^*(r,0)\Phi(r,\phi_0)\rangle$ is equal to 1. As r_0 decreases the value

of the correlation function $\langle \Phi^*(r,0)\Phi(r,\phi_0)\rangle$ also decreases. Through use of Eq. B.8 expression (B.6) for the intensity can be expressed as

$$\begin{aligned}\langle I_\ell\rangle &= \mathcal{I}_0 + \mathcal{I}_\ell \\ \mathcal{I}_0 &= \frac{1}{\pi}\int r dr \mathcal{E}^2(r) \\ \mathcal{I}_\ell &= \frac{\cos(\ell\phi_0)}{\pi}\int r dr |\mathcal{E}(r)|^2 \exp(-\beta r^2).\end{aligned} \tag{B.10}$$

As r_0 decreases, β increases and most of the contribution to the integral in the last expression comes from $r \approx 0$, but since the integrand is zero at that point, the integral vanishes. In this limit, $\mathcal{I}_0$ makes the only contribution to $\langle I_\ell\rangle$ and the spectrum becomes flat, that is, $\langle I_\ell\rangle$ shows no dependence on the value of ℓ.

Next we derive an expression for the correlations between projections onto OAM values of ℓ and $-\ell$, that is,

$$\begin{aligned}I_\ell I_{-\ell} = &\frac{1}{4\pi^2}\int r_1 dr_1 |\mathcal{E}(r_1)|^2 \left\{2 + e^{-i\ell\phi_0}\Phi^*(r_1,0)\Phi(r_1,\phi_0) + e^{i\ell\phi_0}\Phi^*(r_1,\phi_0)\Phi(r_1,0)\right\} \\ &\times \int r_2 dr_2 |\mathcal{E}(r_2)|^2 \left\{2 + e^{i\ell\phi_0}\Phi^*(r_2,0)\Phi(r_2,\phi_0) + e^{-i\ell\phi_0}\Phi^*(r_2,\phi_0)\Phi(r_2,0)\right\} \\ \equiv &\mathcal{G}_0 + \mathcal{G}_\ell + \mathcal{G}_{2\ell},\end{aligned} \tag{B.11}$$

where the three contributions to $I_\ell I_{-\ell}$ are given by

$$\begin{aligned}\mathcal{G}_0 =&\frac{1}{\pi^2}\int r_1 dr_1 r_2 dr_2 |\mathcal{E}(r_1)|^2|\mathcal{E}(r_2)|^2 \\ &+\frac{1}{4\pi^2}\int r_1 dr_1 r_2 dr_2 |\mathcal{E}(r_1)|^2|\mathcal{E}(r_2)|^2\,\Phi^*(r_1,0)\Phi(r_1,\phi_0)\Phi^*(r_2,0)\Phi(r_2,\phi_0) \\ &+\frac{1}{4\pi^2}\int r_1 dr_1 r_2 dr_2 |\mathcal{E}(r_1)|^2|\mathcal{E}(r_2)|^2\,\Phi^*(r_1,\phi_0)\Phi(r_1,0)\Phi^*(r_2,\phi_0)\Phi(r_2,0)\end{aligned} \tag{B.12}$$

$$\begin{aligned}\mathcal{G}_\ell =&\frac{1}{2\pi^2}\int r_1 dr_1 r_2 dr_2 |\mathcal{E}(r_1)|^2|\mathcal{E}(r_2)|^2\, e^{-i\ell\phi_0}\,\{\Phi^*(r_1,0)\Phi(r_1,\phi_0) \\ &+\Phi^*(r_2,\phi_0)\Phi(r_2,0) + \text{c.c.},\ \text{and}\end{aligned} \tag{B.13}$$

$$\begin{aligned}\mathcal{G}_{2\ell} =&\frac{1}{4\pi^2}\int r_1 dr_1 r_2 dr_2 |\mathcal{E}(r_1)|^2|\mathcal{E}(r_2)|^2\, e^{-2i\ell\phi_0} \\ &\times\{\Phi^*(r_1,0)\Phi(r_1,\phi_0)\Phi^*(r_2,\phi_0)\Phi(r_2,0)\} + \text{c.c.}\end{aligned} \tag{B.14}$$

We next estimate the ensemble averages of these quantities. For a field with strong random fluctuations, the field correlation between two different angular positions is very small and thus the term $\mathcal{G}_\ell$ does not contribute significantly to $\langle I_\ell I_{-\ell}\rangle$. A similar situation occurs for the second and third contributions of $\mathcal{G}_0$; it is important to note that these terms contain the quantities $\langle\Phi^*(r_1,0)\Phi(r_1,\phi_0)\Phi^*(r_2,0)\Phi(r_2,\phi_0)\rangle$ and $\langle\Phi^*(r_1,\phi_0)\Phi(r_1,0)\Phi^*(r_2,\phi_0)\Phi(r_2,0)\rangle$, and these quantities vanish when $r_1 = r_2$. They vanish because they describe the average of the product of two chaotic and independent variables. Thus, the main contributions to the second-order interference

are the first term in Eq.12 (which does not vary with ϕ_0) and the contribution

$$\langle \mathcal{G}_{2\ell} \rangle = \frac{e^{-2i\ell\phi_0}}{4\pi^2} \int r_1 dr_1 r_2 dr_2 |\mathcal{E}(r_1)|^2 |\mathcal{E}(r_2)|^2 \langle \Phi^*(r_1, 0)\Phi(r_1, \phi_0)\Phi^*(r_2, \phi_0)\Phi(r_2, 0)\rangle + \text{c.c.}. \tag{B.15}$$

We would like to remark the fact that, contrary to the correlation functions given by $\langle \Phi^*(r_1, 0)\Phi(r_1, \phi_0)\Phi^*(r_2, 0)\Phi(r_2, \phi_0)\rangle$ and $\langle \Phi^*(r_1, \phi_0)\Phi(r_1, 0)\Phi^*(r_2, \phi_0)\Phi(r_2, 0)\rangle$, the correlation function $\langle \Phi^*(r_1, 0)\Phi(r_1, \phi_0)\Phi^*(r_2, \phi_0)\Phi(r_2, 0)\rangle$ is equal to unity for $r_1 = r_2$. We therefore obtain

$$\langle \mathcal{G}_{2l} \rangle = \frac{e^{-2i\ell\phi_0}}{4\pi^2} \int r_1^2 dr_1 |\mathcal{E}(r_1)|^4 + \text{c.c.} \tag{B.16}$$

We thus conclude that the quantity $\langle I_l I_{-l} \rangle$ is given by the sum of the contributions of Eq. B.16 and the first term in Eq. B.12 or

$$\langle I_l I_{-l} \rangle \approx \left(\frac{1}{\pi} \int r dr |\mathcal{E}(r)|^2 \right)^2 + \left(\frac{\cos 2l\phi_0}{2\pi^2} \int r^2 dr |\mathcal{E}(r)|^4 \right). \tag{B.17}$$

For the case of slits with finite size, this result must be modified for the same reasons given in the discussion following Eq. B.6. One thereby obtains

$$\langle I_l I_{-l} \rangle \approx \left(\frac{1}{\pi} \int r dr |\mathcal{E}(r)|^2 \right)^2 + \frac{\alpha^4 \text{sinc}^4\left(\frac{\ell\alpha}{2}\right)}{4\pi^4} \left(\frac{\cos 2l\phi_0}{2\pi^2} \int r^2 dr |\mathcal{E}(r)|^4 \right). \tag{B.18}$$

The HBT effect for arbitrary mode indices ℓ_1 and ℓ_2.

The intensity correlation between two arbitrary OAM modes $\langle I_{\ell_1} I_{\ell_2}\rangle$ produces a complicated second-order correlation function comprised of five terms. The contribution of each term is determined by the degree of fluctuations in the field. One is the constant term $\mathcal{G}_0$ given by $\frac{1}{\pi^2}\int r_1 dr_1 r_2 dr_2 \langle|\mathcal{E}(r_1)|^2|\mathcal{E}(r_2)|^2\rangle$. There are two terms whose contributions are equally important; one oscillates with a frequency $\ell_1\phi_0$ and the other with $\ell_2\phi_0$. The strength of these terms is determined by the quantity $\langle\Phi^*(r,0)\Phi(r,\phi_0)\rangle$, which is negligible for highly chaotic light ($r_0 \ll r$). The frequency of the fourth component is determined by the quantity $(\ell_1+\ell_2)\phi_0$, although its strength is dictated by the quantity $\langle\Phi^*(r,0)\Phi(r,\phi_0)\Phi^*(r,0)\Phi(r,\phi_0)\rangle$. For highly chaotic fields this is an extremely small contribution. The primary contribution to $\langle I_{\ell_1} I_{\ell_2}\rangle$ is therefore given by the term

$$\begin{aligned}\mathcal{G}_{\ell_1,\ell_2} =& \frac{\alpha^4 \mathrm{sinc}^4\left(\frac{[\ell_1-\ell_2]\alpha}{2}\right)}{4\pi^4}\int r_1 dr_1 r_2 dr_2 |\mathcal{E}(r_1)|^2|\mathcal{E}(r_2)|^2 \,(e^{-i(\ell_1-\ell_2)\phi_0} \\ &\times\langle\Phi^*(r_1,0)\Phi(r_1,\phi_0)\Phi^*(r_2,\phi_0)\Phi(r_2,0)\rangle + \text{c.c.})\end{aligned} \tag{B.19}$$

Note that this contribution describes an interference pattern that depends on the values of both ℓ_1 and ℓ_2.

Orbital angular momentum correlations and angular position correlations.

In this section we derive expressions for the correlations of pairs of OAM values and pairs of angular positions. The light that emerges from the DMD is given by $\mathcal{E}(r)\Phi(r,\phi)$. We make two copies of this field using a beam splitter and find the coincidences between projections onto two different modes of light. Let us first discuss the projection of one of the beams. The amplitude of the projection onto OAM mode ℓ is given by

$$a_\ell = \int r dr d\phi \mathcal{E}(r)\Phi(r,\phi)\frac{e^{-i\ell\phi}}{\sqrt{2\pi}}g(r), \tag{B.20}$$

where $g(r)$ is the radial profile of the single-mode collection fiber, which is a Gaussian function. The intensity $|a_\ell|^2$ is given by

$$I_\ell = \int r_1 dr_1 d\phi_1 \mathcal{E}(r_1)\Phi(r_1,\phi_1)\frac{e^{-i\ell\phi_1}}{\sqrt{2\pi}}g(r_1) \times \int r_2 dr_2 d\phi_2 \mathcal{E}^*(r_2)\Phi^*(r_2,\phi_2)\frac{e^{i\ell\phi_2}}{\sqrt{2\pi}}g(r_2). \tag{B.21}$$

Therefore the ensemble-averaged intensity after the projection is given by

$$\langle I_\ell\rangle = \int r_1 dr_1 r_2 dr_2 d\phi_1 d\phi_2 \mathcal{E}(r_1)g(r_1)\mathcal{E}^*(r_2)g(r_2)\frac{e^{-i\ell(\phi_1-\phi_2)}}{2\pi}\langle\Phi(r_1,\phi_1)\Phi^*(r_2,\phi_2)\rangle. \tag{B.22}$$

We are considering the case of highly fluctuating light; in this regime $\langle \Phi(r_1, \phi_1)\Phi^*(r_2, \phi_2)\rangle$ can be approximated by $(1/r_1)\delta(r_2 - r_1, \phi_2 - \phi_1)$, leading to the result

$$\langle I_\ell \rangle = \frac{1}{2\pi} \int r_1 dr_1 d\phi_1 |\mathcal{E}(r_1)|^2 \, g(r_1)^2. \tag{B.23}$$

Note that this quantity is independent of the value ℓ. Now let us consider the case of two coincident projections. The amplitude of coincident projections is given by

$$a_{\ell_1} a_{\ell_2} = \Pi_{i=1}^2 \left(\int r_i dr_i d\phi_i \mathcal{E}(r_i)\Phi(r_i, \phi_i) \frac{e^{-i\ell_i \phi_i}}{\sqrt{2\pi}} g(r_i) \right). \tag{B.24}$$

We measure the rate at which these coincidences occur, which is given by

$$\begin{aligned} I_{\ell_1} I_{\ell_2} = &\int r_1 dr_1 d\phi_1 \mathcal{E}(r_1)\Phi(r_1, \phi_1) \frac{e^{-i\ell_1 \phi_1}}{\sqrt{2\pi}} g(r_1) \times \int r_2 dr_2 d\phi_2 \mathcal{E}(r_2)\Phi(r_2, \phi_2) \frac{e^{-i\ell_2 \phi_2}}{\sqrt{2\pi}} g(r_2) \\ &\times \int r_3 dr_3 d\phi_3 \mathcal{E}^*(r_3)\Phi^*(r_3, \phi_3) \frac{e^{i\ell_1 \phi_3}}{\sqrt{2\pi}} g(r_3) \times \int r_4 dr_4 d\phi_4 \mathcal{E}^*(r_4)\Phi^*(r_4, \phi_4) \frac{e^{i\ell_2 \phi_4}}{\sqrt{2\pi}} g(r_4). \end{aligned} \tag{B.25}$$

After taking the statistical average, we obtain

$$\begin{aligned} \langle I_{\ell_1} I_{\ell_2} \rangle = &\int r_1 dr_1 d\phi_1 \mathcal{E}(r_1) \frac{e^{-i\ell_1 \phi_1}}{\sqrt{2\pi}} g(r_1) \times \int r_2 dr_2 d\phi_2 \mathcal{E}(r_2) \frac{e^{-i\ell_2 \phi_2}}{\sqrt{2\pi}} g(r_2) \\ &\times \int r_3 dr_3 d\phi_3 \mathcal{E}^*(r_3) \frac{e^{i\ell_1 \phi_3}}{\sqrt{2\pi}} g(r_3) \times \int r_4 dr_4 d\phi_4 \mathcal{E}^*(r_4) \frac{e^{i\ell_2 \phi_4}}{\sqrt{2\pi}} g(r_4) \\ &\times \langle \Phi(r_1, \phi_1)\Phi^*(r_3, \phi_3)\Phi(r_2, \phi_2)\Phi^*(r_4, \phi_4)\rangle. \end{aligned} \tag{B.26}$$

Following the same considerations and a similar procedure those used in obtaining Eq. B.11, we write the four-point coherence function as the sum of three contributions, each a product of two 2-point coherence functions. One of the contributions is always negligible for highly chaotic light. Another contribution leads to the simple product $\langle I_{\ell_1}\rangle\langle I_{\ell_2}\rangle$. This contribution is actually independent of the values ℓ_1 and ℓ_2 in the limit of highly chaotic light for the same reason stated above in connection with Eq. B.9. The last contribution is given by

$$\int r_1 dr_1 d\phi_1 \mathcal{E}(r_1)\frac{e^{-i\ell_1\phi_1}}{\sqrt{2\pi}}g(r_1) \times \int r_4 dr_4 d\phi_4 \mathcal{E}^*(r_4)\frac{e^{i\ell_2\phi_4}}{\sqrt{2\pi}}g(r_4) \times \langle\Phi(r_1,\phi_1)\Phi^*(r_4,\phi_4)\rangle$$
$$\times \int r_2 dr_2 d\phi_2 \mathcal{E}(r_2)\frac{e^{-i\ell_2\phi_2}}{\sqrt{2\pi}}g(r_2) \times \int r_3 dr_3 d\phi_3 \mathcal{E}^*(r_3)\frac{e^{i\ell_1\phi_3}}{\sqrt{2\pi}}g(r_3) \times \langle\Phi(r_2,\phi_2)\Phi^*(r_3,\phi_3)\rangle. \tag{B.27}$$

By invoking the same approximation used above to evaluate the coherence functions as delta functions, we simplify this expression to

$$\left|\int r dr d\phi |\mathcal{E}(r)|^2\, g(r)^2 \frac{e^{-i(\ell_1-\ell_2)\phi}}{2\pi}\right|^2. \tag{B.28}$$

Note that the integral over ϕ vanishes unless $\ell_1 = \ell_2$. Thus, we finally obtain

$$\langle I_{\ell_1,\ell_2}\rangle = \langle I_{\ell_1}\rangle\langle I_{\ell_2}\rangle(1+\delta_{\ell_1,\ell_2}), \tag{B.29}$$

which is the expression used in the body of this paper to explain our experimental results. Note that the correlations between two different values of OAM are half as large as those between the same value of OAM.

We can perform a similar calculation to find the correlations between two angular positions. For the case of a single beam (no beam splitter), the amplitude of the projection for a single value of ϕ is given by

$$a_\phi = \int r dr \mathcal{E}(r)\Phi(r,\phi)g(r). \tag{B.30}$$

It follows that the ensemble-averaged intensity at one of the detectors is given as follows

$$\begin{aligned}
\langle I_\phi \rangle &= \langle |a_\phi|^2 \rangle && \text{(B.31)}\\
&= \langle \int r_1 dr_1 \mathcal{E}(r_1)\Phi(r_{,1}\,\phi)g(r_1) \times \int r_2 dr_2 \mathcal{E}^*(r_2)\Phi^*(r_2,\phi)g(r_2)\rangle && \text{(B.32)}\\
&= \int r_1 dr_1 r_2 dr_2 \mathcal{E}(r_1)\mathcal{E}^*(r_2)g(r_1)g(r_2)\,\langle \Phi(r_{,1}\,\phi)\Phi(r_2,\phi)^*\rangle && \text{(B.33)}\\
&= \int r dr |\mathcal{E}(r)|^2\, g(r)^2. && \text{(B.34)}
\end{aligned}$$

The last form follows from the substitution $\langle \Phi(r_{,1}\,\phi)\Phi(r_2,\phi)^*\rangle = (1/r_1)\delta(r_1 - r_2)$. If we now add the beam splitter and find the probability for coincidence detection of

two beams, we obtain

$$\langle I_{\phi_1} I_{\phi_2} \rangle = \int r_1 dr_1 \mathcal{E}(r_1) g(r_1) \times \int r_2 dr_2 \mathcal{E}(r_2) g(r_2) \tag{B.35}$$

$$\times \int r_3 dr_3 \mathcal{E}^*(r_3) g(r_3) \times \int r_4 dr_4 \mathcal{E}^*(r_4) g(r_4) \tag{B.36}$$

$$\times \langle \Phi(r_1, \phi_1) \Phi^*(r_3, \phi_3) \Phi(r_2, \phi_2) \Phi^*(r_4, \phi_4) \rangle. \tag{B.37}$$

Similar to the OAM case, we find that this expression yields two contributions. One of these contributions is independent of the values ϕ_1 and ϕ_2 whereas the other contribution is large only if the two intensities are measured at $\phi_1 = \phi_2$. This result can be described by the relation

$$\langle I_{\phi_1} I_{\phi_2} \rangle = \langle I_{\phi_1} \rangle \langle I_{\phi_2} \rangle [1 + \delta(\phi_1 - \phi_2)]. \tag{B.38}$$

As expected, and similar to the case of correlating two OAMs, two non-overlapping angles share no correlation. However, in contrast to the OAM variable, the angular position variable is not discrete, and one is allowed to correlate two regions defined by two angular positions that are not orthogonal, and consequently there is a partial overlap between the two correlated regions. Thus the degree of second-order correlation can take any value between 1 and 2. Therefore an appropriate expression for this correlation function is given by

$$\langle I_{\phi_1} I_{\phi_2} \rangle = \langle I_{\phi_1} \rangle \langle I_{\phi_2} \rangle [1 + f(\phi_1 - \phi_2)], \tag{B.39}$$

where $f(\phi_1 - \phi_2)$ is defined as

$$f(\phi_1 - \phi_2) = \begin{cases} 0 & \text{for } |\phi_1 - \phi_2| > \alpha/2 \\ 1 - \frac{|\phi_1 - \phi_2|^2}{\alpha^2} & \text{for } |\phi_1 - \phi_2| \leq \alpha/2. \end{cases}$$

$f(\phi_1 - \phi_2)$ can be interpreted as the fractional angular overlaps of the two slits.

Appendix C

Measuring Looped Trajectories of Light

Experiment

We generate single photons by means of heralding a photon by a“partner” photon detection from a photon pair source. The photon pairs were created in a spontaneous parametric down conversion process using a 2mm-long type-I nonlinear crystal (periodically poled potassium titanyl phosphate (ppKTP)). We pump the crystal with a blue 405nm continuous-wave diode laser (∼200mW), thereby creating degenerate photon pairs at 810nm wavelength. Both photons are passed through a 3nm band-pass filter, coupled into a single-mode fiber and split by a 50/50-fiber beams splitter, which led to a coincidence count rate of approximately 40kHz. The heralding photon is detected with a single-photon avalanche photo diode. Its partner photon is delayed by a 22m long fiber, send through the setup and imaged by an ICCD. The ICCD is operated in the external triggering mode (7ns coincidence gate time), where the heralding

detection signal is used as an external trigger, to ensure that only these single photon events are registered. Note that due to the low coincidence count rate there is only one photon at a time in the experimental setup. For experiments using a weak laser instead of heralded single photons, the ICCD was operated in the continuous mode, where the intensifier is permanently switched on.

For the case in which we used single photons, the idler photons are detected by an APD that heralds the detection of signal photons with an ICCD. We used either y- or x-polarized light which is selected by means of a polarizer and half-wave plate. The beam is weakly focused onto the arrangement of slits that is mounted on a motorized three-axis translation stage that can be displaced in small increments of 60 nm. An infinity-corrected oil-immersion microscope objective (NA=1.4, magnification of 60×, working distance of 100 μm) was used to collect the light emerging from the slit patterns. The light collected by the objective was then magnified with a telescope and measured by an ICCD camera..

Data Analysis

The background subtracted interference patterns were used to determine the magnitudes of κ shown in Fig. 6.4. In Fig. 6.4a, we show the values of κ, obtained in the single photon regime, for different positions of the detector. The deviation from the theory and the magnitude of the error bars are larger at the edges of the κ profile

because the signal is low at the edges of the interference patters, which results in a noisier signal. On the other hand, the central maximum of the interference patterns permits a more reliable characterization of κ. The values of κ obtained for classical light as a function of the wavelength, shown in Fig. 6.4b and 6.4c, were calculated using central maximum of the interference patterns. For these cases, we used only the regions of central fringe having intensities within 70% of the peak value. The data was then used to obtain the mean value and standard deviations for κ.

Fabrication

The glass substrates are standard BK7 cover slips (SCHOTT multipurpose glass D 263® T eco Thin Glass) with a thickness of $\sim 170\mu$m, polished on both sides to optical quality. The substrate was ultrasonically cleaned for 2 hours in 2% Hellmanex III alkaline concentrate solution and subsequently rinsed and sonicated in MEK denatured Ethanol and then in demineralized water. The gold films were evaporated directly onto the clean glass substrates with no additional adhesive layer using a Plassys MEB 550S e-beam evaporation system. The growth of the film thickness was monitored in-situ during the evaporation by a water cooled quartz micro-balance. The slit patterns were structured by Ga ion beam milling using a Tescan Lyra 3 GMU SEM/FIB system with a canion FIB column from Orsay Physics. Each slit pattern consisted of 100μm long slits. While fabricating the different slit sets, proper focusing of the FIB was checked

by small test millings and if needed the FIB settings were readjusted accordingly to provide a consistent and reproducible slit quality.

Structure design

Full-wave electromagnetic simulations were conducted using a Maxwell's equation solver based on the finite difference time domain method (Lumerical FDTD). The dispersion of the materials composing the structure was taken into account by using their frequency-dependent permittivities. The permittivity of the gold film was obtained from Ref. [155], the permittivity of the glass substrate (BK7) was taken from the manufacturer's specifications, and the permittivity of the index matching fluid (Cargille oil Type B 16484) was obtained by extrapolation from the manufacturer's specification.

Model

As described in the main text, the path integral formulation of the wave equation propagation kernel is given by

$$K(\mathbf{r}_1, \mathbf{r}_2) = \int \mathcal{D}[x(\mathbf{s})] \exp\left(ik \int \mathrm{d}\mathbf{s}\right), \tag{C.1}$$

and can be perturbatively expanded as [145]

$$K = K_1 + K_2 + K_3 + \cdots , \tag{C.2}$$

where K_n represents the nth application of of the Fresnel-Huygens principle. For instance, considering the propagation through the slits from the source located at $\mathbf{r_s}$ to the detector at $\mathbf{r_d}$, the expression for K_2 would be given by

$$K_2(\mathbf{r_s}, \mathbf{r_d}) = \int_\Omega \mathrm{d}\mathbf{r_1} \int_\Omega \mathrm{d}\mathbf{r_2} K(\mathbf{r_s}, \mathbf{r_1}) K(\mathbf{r_1}, \mathbf{r_2}) K(\mathbf{r_2}, \mathbf{r_d}), \tag{C.3}$$

where integration is over the slit areas Ω. Furthermore, assuming that the slits are much smaller than the wavelength, we can rewrite this equation as a discrete sum over paths. In this case, the expression above becomes

$$K_2(\mathbf{r_s}, \mathbf{r_d}) \approx \sum_{j,k} K(\mathbf{r_s}, \mathbf{r_j}) K(\mathbf{r_j}, \mathbf{r_k}) K(\mathbf{r_k}, \mathbf{r_D}), \tag{C.4}$$

which represents propagation from the source $\mathbf{r_s}$, to slit j at $\mathbf{r_j}$, and then from slit j to k at $\mathbf{r_k}$, and then finally propagation to the detector at $\mathbf{r_d}$.

Each term in Eq. C.4 represents a simple propagation solution. Assuming that the slits are illuminated with a planewave normally incident onto the surface of the slits,

then the propagation from the source to the screen is

$$K(\mathbf{r_s}, \mathbf{r_A}) = K(\mathbf{r_s}, \mathbf{r_B}) = K(\mathbf{r_s}, \mathbf{r_C}) = \text{constant}, \tag{C.5}$$

and the three straight paths in the (paraxial) far field will be given by

$$\begin{aligned} K(\mathbf{r_B}, \mathbf{D}) &\propto \operatorname{sinc}\left(\frac{k_x w}{2\pi}\right) \\ K(\mathbf{r_A}, \mathbf{D}) &= K(\mathbf{r_B}, \mathbf{D}) e^{i\phi_f} \\ K(\mathbf{r_C}, \mathbf{D}) &= K(\mathbf{r_B}, \mathbf{D}) e^{-i\phi_f}, \end{aligned} \tag{C.6}$$

where θ is the far field angle in the (x, z) plane ($\theta = 0$ corresponding to propagation in the z direction), w is the slit size, p is the spacing between slits, $k_0 = 2\pi/\lambda$ is the free-space wavenumber, $k_x = k_0 \sin(\theta)$ is the transverse wavenumber, and $\phi_f = pk_x$ is the phase difference due to differences in the distance between each slit and the far field.

For the case at hand, the looped paths involve an enhancement of the near field by surface plasmon modes which we solve for via numerical simulations using the FDTD method. For the simple configuration of slits in a metal screen, it has been shown that this is well approximated by the simple input-output relations [153]

$$K(\mathbf{r_A}, \mathbf{r_B}) = K(\mathbf{r_B}, \mathbf{r_A}) = K(\mathbf{r_B}, \mathbf{r_C}) = K(\mathbf{r_C}, \mathbf{r_B}) = a e^{i\phi_{\mathrm{SP}}} \tag{C.7a}$$

$$K(\mathbf{r_A}, \mathbf{r_C}) = K(\mathbf{r_C}, \mathbf{r_A}) = b e^{i2\phi_{\mathrm{SP}}}, \tag{C.7b}$$

where a and b are the relevant field strengths quantifying the coupling of a free-space to surface plasmon back to free-space mode for neighboring slits and paths with an extra slit between, and $\phi_{\mathrm{SP}} = k_{\mathrm{SP}}p$ is the phase accumulated along the plasmon path between slits.

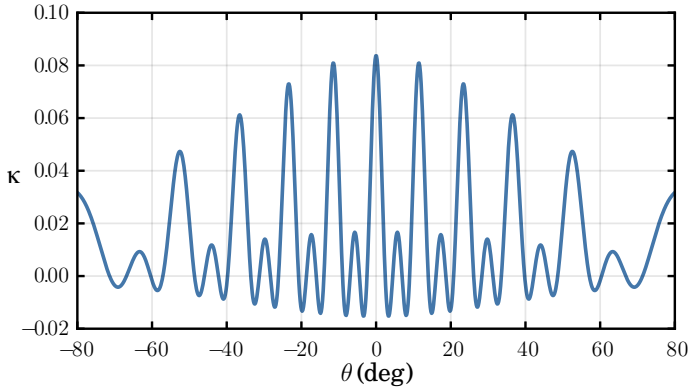

Figure C.1: Plot of the normalized Sorkin parameter, κ, assuming experimental parameters similar to those used in the main text.

A plot of the normalized Sorkin parameter, κ, is shown in Fig. C.1 assuming the parameters $p = 3.8$ µm, $w = 400$ nm, and $\lambda = 755$ nm, equivalent to the main paper. This plot was generated using the surface plasmon mode coupling parameters $a = 2b = 0.06$, and $k_{\mathrm{SP}} = 1.6k_0$. When this plot is compared with Fig. 6.4a and 6.4b, it can be seen that this simple model matches the observed features in both the experiment and full FDTD simulations of the experiment.

Signs of Looped Trajectories

Since the exotic looped trajectories of light are intimately related to the evanescent component of the fields, the conditions under which the probability of photons following looped trajectories is increased depends on the characteristics of the three slits and the physical processes that take place in their vicinity. The most suitable characteristics for the slits were found by investigating the regimes under which the looped trajectories show a significant role in the formation of interference fringes. We carried out this task by performing a series of FDTD simulations in which different slit sizes, slit separations, and metal thickness were studied.

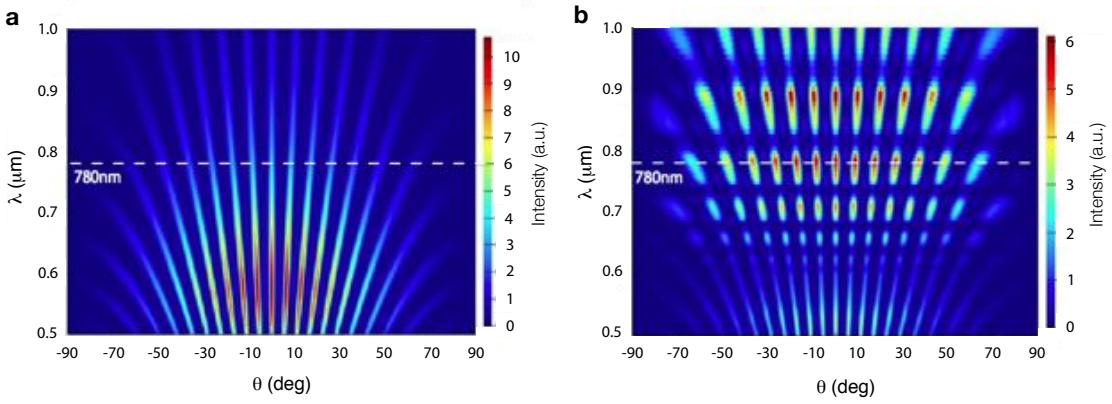

Figure C.2: The wavelength-dependent intensity distribution of the interference pattern for a three-slit experiment in the absence (a) and pretense (b) of looped trajectories. Looped trajectories are enhanced by using along the short direction of the slit.

In Fig. C.2 we show distinct interference structures that unveil the importance of looped trajectories in the formation of interference structures. We plot the intensity as a function of wavelength and detector angles, or positions in the far-field of the three slits. In our calculations, we consider that the slits have a width of $w = 150$ nm,

the separation between slits is $p = 3.6\mu$m, the hight of the slits is infinite, and the three-slit structure is illuminated by a planewave at normal incidence. We show two interference structures produced by the same three-slit structure but under different illumination conditions. When these slits are illuminated with light polarized along the long axis of the slits, surface plasmon modes are not excited in the structure and the interference pattern shown in Fig. C.2a is shown in the far field. This pattern is practically identical to that obtained by simply applying the Fourier transform of the three slits. However, this simple experiment shows a striking interference structure when the slits are illuminated with light polarized along the short axis of the slits. In this case, surface plasmon modes are efficiently excited, leading to an increased probability for looped paths, which in turn leads to the significantly different interference pattern shown in Fig. C.2b. In addition, from this pattern it is quite clear how interference effects among looped trajectories lead to a clear wavelength dependence of the experiment.

The remarkable difference between these two interference structures offered us a clear signature of the presence of looped trajectories. We used this knowledge to decide the characteristics of the slits and the conditions we used when we performed the experiment.